

A SEARCH FOR SUPERSYMMETRY IN EVENTS WITH A Z  
BOSON, JETS, AND MISSING TRANSVERSE ENERGY IN  $p - p$   
COLLISIONS WITH  $\sqrt{s}=13$  TEV WITH THE ATLAS DETECTOR

TOVA RAY HOLMES



Physics Department  
University of California, Berkeley

August 2016 – version 1.0

Tova Ray Holmes: *A Search for Supersymmetry in Events with a Z Boson, Jets, and Missing Transverse Energy in  $p - p$  Collisions with  $\sqrt{s}=13$  TeV with the ATLAS Detector*, © August 2016





## ABSTRACT

---



## PUBLICATIONS

---

Some ideas and figures have appeared previously in the following publications:

Put your publications from the thesis here. The packages `multibib` or `bibtopic` etc. can be used to handle multiple different bibliographies in your document.



## ACKNOWLEDGEMENTS

---

Put your acknowledgements here.



## CONTENTS

---

<b>I</b>	<b>INTRODUCTION</b>	<b>1</b>
1	INTRODUCTION	3
<b>II</b>	<b>THEORY AND MOTIVATION</b>	<b>5</b>
2	THEORY AND MOTIVATION	7
2.1	The Standard Model . . . . .	7
2.1.1	Matter . . . . .	8
2.1.2	Forces . . . . .	9
2.1.3	Phenomenology of Proton-Proton Collisions . . . . .	16
2.1.4	Problems in the Standard Model . . . . .	17
2.2	Supersymmetry . . . . .	18
2.2.1	Supersymmetry Phenomenology . . . . .	19
2.2.2	Solutions to Standard Model Problems . . . . .	19
2.2.3	Supersymmetry Signatures in $p - p$ Collisions . . . . .	19
2.3	Monte Carlo Generators . . . . .	19
<b>III</b>	<b>THE EXPERIMENT</b>	<b>21</b>
3	THE LARGE HADRON COLLIDER	23
3.1	The Injector Complex . . . . .	24
3.2	Operation of the Large Hadron Collider . . . . .	25
3.3	Luminosity . . . . .	27
3.4	Pile-up in $p - p$ Collisions . . . . .	28
4	THE ATLAS DETECTOR	31
4.1	Coordinate System Used in the ATLAS Detector . . . . .	31
4.2	The Inner Detector . . . . .	32
4.2.1	The Pixel Detector . . . . .	32
4.2.2	The Silicon Microstrip Tracker . . . . .	34
4.2.3	The Transition Radiation Tracker . . . . .	34
4.3	The Calorimeters . . . . .	35
4.4	The Muon Spectrometer . . . . .	36
4.5	The Magnet System . . . . .	38
4.6	The Trigger System and Data Acquisition . . . . .	41
5	OBJECT RECONSTRUCTION IN THE ATLAS DETECTOR	45
5.1	Electrons . . . . .	45
5.2	Photons . . . . .	45
5.3	Muons . . . . .	45
5.4	Jets . . . . .	45
5.5	Missing Transverse Energy . . . . .	45
5.6	Monte Carlo Simulation . . . . .	45
6	APPLICATION OF A NEURAL NETWORK TO PIXEL CLUSTERING	47
6.1	Clustering in the Pixel Detector . . . . .	47

6.1.1	Charge Interpolation Method . . . . .	48
6.1.2	Improving Measurement with Neural Networks	48
6.2	Impact of the Neural Network . . . . .	49
6.2.1	The Neural Network in 13 TeV Data . . . . .	50
<b>IV</b>	<b>SEARCHING FOR SUPERSYMMETRY</b>	<b>55</b>
7	<b>BACKGROUND PROCESSES</b>	<b>57</b>
7.1	Monte Carlo Samples . . . . .	59
8	<b>OBJECT IDENTIFICATION AND SELECTION</b>	<b>61</b>
8.1	Electrons . . . . .	61
8.2	Muons . . . . .	61
8.3	Jets . . . . .	61
8.4	Photons . . . . .	61
9	<b>EVENT SELECTION</b>	<b>63</b>
9.1	Signal Region . . . . .	63
9.2	Control and Validation Regions . . . . .	63
10	<b>BACKGROUND ESTIMATION</b>	<b>67</b>
10.1	Flavor Symmetric Processes . . . . .	67
10.1.1	Flavor Symmetry Method . . . . .	67
10.1.2	Sideband Fit Method . . . . .	69
10.2	$Z/\gamma^*$ + jets Background . . . . .	70
10.3	Fakes . . . . .	73
10.4	Diboson and Rare Top Processes . . . . .	76
11	<b>SYSTEMATIC UNCERTAINTIES</b>	<b>79</b>
11.1	Uncertainties on Data-Driven Backgrounds . . . . .	79
11.1.1	Uncertainties on the Flavor Symmetry Method .	79
11.1.2	Uncertainties on the $\gamma$ +jets Method . . . . .	84
11.1.3	Uncertainties on the Fakes Background . . . . .	84
11.2	Theoretical and Experimental Uncertainties . . . . .	84
11.3	Impact of Uncertainties on the Signal Region . . . . .	85
12	<b>RESULTS</b>	<b>89</b>
13	<b>INTERPRETATIONS</b>	<b>91</b>
<b>V</b>	<b>CONCLUSIONS</b>	<b>93</b>
14	<b>CONCLUSIONS</b>	<b>95</b>
15	<b>OUTLOOK</b>	<b>97</b>
	<b>BIBLIOGRAPHY</b>	<b>99</b>

## LIST OF FIGURES

---

Figure 1	The Standard Model of particle physics, containing all known bosons and fermions, with the addition of the hypothetical graviton. [38]	8
Figure 2	Gluon self coupling Feynman diagrams involving 3- and 4-gluon interactions. . . . .	12
Figure 3	Quark couplings to the different types of gauge bosons. The $q_{u,d}$ labels represent any up- or down-type quarks. . . . .	13
Figure 4	The running of the strong coupling constant, $\alpha_s$ . [50] . . . . .	14
Figure 5	Trilinear gauge couplings in the Standard Model (SM). . . . .	14
Figure 6	2008 MSTW Parton Distribution Functions (PDFs) for various particle types. [48] . . . . .	16
Figure 7	Galactic rotation curve showing that the discrepancy between the observed luminous matter and the total mass in the system can be described as a non-luminous halo of matter. [53]	17
Figure 8	SM particles and their superpartners, with mass very roughly indicated by size. [newscientist-pz]	19
Figure 9	The Large Hadron Collider (LHC) main collider ring and pre-accelerator Super Proton Synchrotron (SPS) overlaid on a map of Switzerland and France, with the four main LHC experiments identified. . . . .	23
Figure 10	The pre-accelerators of the LHC. . . . .	24
Figure 11	Bunch structure in the Proton Synchrotron (PS), SPS, and LHC. . . . .	25
Figure 12	Cross-section of a cryodipole magnet in the LHC.	26
Figure 13	Beam spot in the ATLAS detector for one run in 2015. Distributions show only the highest $p_T$ vertex per event. Left is the $x - y$ distribution of vertices, while the right plot shows the $x - z$ distribution. . . . .	26
Figure 14	Cross-sections for many SM processes at the Tevatron and LHC [1]. . . . .	27
Figure 15	Instantaneous luminosity of one fill of 7 TeV data in 2011. . . . .	28
Figure 16	ATLAS luminosity for Run 1 and Run 2, as of September 2016. . . . .	29

Figure 17	Average number of interactions per crossing shown for 2015 and 2016 separately, as well as the sum of the two years. . . . .	29
Figure 18	Diagram of the ATLAS detector, with subsystems and magnets identified. . . . .	31
Figure 19	Diagram of the ATLAS Inner Detector, containing the Pixel, SCT, and TRT subsystems. . . .	33
Figure 20	Diagram of one-quarter of the ATLAS Inner Detector in the $R - z$ plane, with lines drawn to indicate various $\eta$ locations. . . . .	34
Figure 21	The calorimeter system of the ATLAS detector.	
Figure 22	An $x$ - $y$ view of the Muon Spectrometer ( <b>MS</b> ). In it, the three barrel layers are visible, as well as the overlapping, differently sized chambers. The outer layer of the <b>MS</b> is about 20m in diameter. . . . .	35
Figure 23	An $r$ - $z$ view of the <b>MS</b> . The three layers of the barrel and endcap <b>MS</b> are visible, and all muons at $ \eta  < 2.7$ should traverse three detectors, assuming they propagate in an approximately straight line from the interaction point. . . .	37
Figure 24	The magnet system of the ATLAS detector. The inner cylinder shows the solenoid which gives a uniform magnetic field in the Inner Detector ( <b>ID</b> ). Outside of that are the barrel and endcap toroids, which provide a non-uniform magnetic field for the <b>MS</b> . . . . .	38
Figure 25	Plots of the magnetic field within the ATLAS detector. Top is the field (broken into its $R$ and $z$ components) as a function of $z$ for several different values of $R$ . Bottom is the field integral through the Monitored Drift Tubes ( <b>MDTs</b> ) as a function of $ \eta $ for two different $\phi$ values. . . .	39
Figure 26	Level One ( <b>L1</b> ) trigger rates for for a run in July 2016 as a function of luminosity block, an approximately 60-second long period of data-taking. The total rate is lower than the combined stack because of overlapping triggers. . . .	40
Figure 27	High Level Trigger ( <b>HLT</b> ) trigger rates for for a run in July 2016 as a function of luminosity block, an approximately 60-second long period of data-taking. The total rate is lower than the combined stack because of overlapping triggers. . . .	42
Figure 28	Trigger efficiencies as a function of $E_T$ for data and Monte Carlo simulation ( <b>MC</b> ). Efficiencies are given for offline selected loose electrons. . . .	43

Figure 29	A few possible types of clusters in the Pixel Detector. (a) shows a single particle passing through a layer of the detector, (b) shows two particles passing through the detector, creating a single merged cluster, and (b) shows a single particle emitting a $\delta$ -ray as it passes through the detector. . . . .	47
Figure 30	One example of a two-particle cluster and its truth information compared with the output of the Neural Networks (NNs). The boxes represent pixels, with a color scale indicating Time Over Threshold (ToT). At top, the $p(N = i)$ values give the output of the Number NN, the probabilities that the cluster contains 1, 2, and 3 particles. Given the highest probability is for $N = 2$ , the other NNs predict the position and errors of the two particles (in white). The black arrows and squares represent the truth information from the cluster, and the black dot and dotted line show the position measurement for the un-split cluster. . . . .	50
Figure 31	$x$ resolutions for clusters with 3 (top) and 4 (bottom) pixels in the $x$ direction in 7 TeV data for Connected Component Analysis (CCA) and NN clustering taken from MC. . . . .	51
Figure 32	Fraction of cluster classes as a function of the distance between tracks for IBL (top) and 2nd pixel layer (bottom). . . . .	52
Figure 33	Performance of the pixel neural network used to identify clusters created by multiple charged particles, as a function of constant coherent scaling of the charge in each pixel in the cluster. The top figure shows the rate at which the neural network wrongly identifies clusters with one generated particle as clusters with multiple particles. The bottom figure shows the rate at which the neural network correctly identifies clusters generated by multiple particles as such. . . . .	53
Figure 34	An example Feynman diagram of $t\bar{t}$ production and decay. . . . .	57
Figure 35	An example Feynman diagram of the production and decay of a WZ event. . . . .	58
Figure 36	An example Feynman diagram of the production and decay of a $Z/\gamma^* + \text{jets}$ event. . . . .	58

Figure 37	Schematic diagrams of the control, validation and signal regions for the on-shell Z (top) and edge (bottom) searches. For the on-shell Z search the various regions are shown in the $m_{\ell\ell} - E_T^{\text{miss}}$ plane, whereas in the case of the edge search the signal and validation regions are depicted in the $H_T - E_T^{\text{miss}}$ plane. . . . .	64
Figure 38	Comparison of data and MC in a selection like SRZ, without the $E_T^{\text{miss}}$ cut. . . . .	70
Figure 39	Sub-leading lepton $p_T$ for $ee$ (left) and $\mu\mu$ (right) events in the tight-tight region used to measure the real-lepton efficiency for 2016. . . . .	74
Figure 40	Sub-leading lepton $p_T$ for $\mu e$ (left) and $\mu\mu$ (right) events in the tight-tight region used to measure the fake-lepton efficiency for 2016. . . . .	75
Figure 41	Same sign validation regions in the $ee$ (top left), $\mu\mu$ (top right), $e\mu$ (bottom left) and $\mu e$ (bottom right) channels combining 2015+2016 data. Uncertainty bands include both statistical and systematic uncertainties. . . . .	75
Figure 42	Distribtuions in VR-WZ. On the top row, reconstructed transverse mass of the W (left) and mass of the Z (right). On the bottom row, $p_T$ of the W (left) and Z (right). . . . .	77
Figure 43	Distribtuions in VR-WZ. On the left, mass of the Z bosons in the event, and on the right, $p_T$ of the Z bosons. . . . .	77
Figure 44	MC closure plots of VRS (top) and SRZ (bottom). The number of events from MC (black points) is compared to the number of events predicted from the flavor symmetry method (yellow histogram). The comparison is performed before the expanded $m_{\ell\ell}$ window is used to predict the on-Z bin. . . . .	80
Figure 45	Measurements of $k$ , the ratio of electron to muon events, in bins of $p_T$ and $\eta$ . On the top is the measurements indexed by the leading lepton, while the measurements indexed by the sub-leading lepton are on the bottom. These efficiencies are for the 2016 dataset. . . . .	81
Figure 46	$\alpha$ , the trigger efficiency ratio, calculated as a function of $E_T^{\text{miss}}$ from three different sources: data, the usual skimmed $t\bar{t}$ MC, and an unskimmed $t\bar{t}$ MC. . . . .	82

- Figure 47 Plots of the fraction of on-Z events with a VR-FS-like selection as a function of  $H_T$ . The top figure shows 2015 data and MC while the bottom figure shows the same for 2016. . . . . 83

## LIST OF TABLES

---

Table 1	Simulated background event samples used in this analysis with the corresponding matrix element and parton shower generators, cross-section order in $\alpha_s$ used to normalise the event yield, underlying-event tune and PDF set. . . . .	<b>60</b>
Table 2	Summary of the electron selection criteria. The signal selection requirements are applied on top of the baseline selection. . . . .	<b>61</b>
Table 3	Summary of the muon selection criteria. The signal selection requirements are applied on top of the baseline selection. . . . .	<b>62</b>
Table 4	Overview of all signal, control and validation regions used in the on-shell Z search. More details are given in the text. The flavour combination of the dilepton pair is denoted as either “SF” for same-flavour or “DF” for different flavour. All regions require at least two leptons, unless otherwise indicated. In the case of CR $\gamma$ , VR-WZ, VR-ZZ, and VR-3L the number of leptons, rather than a specific flavour configuration, is indicated. The main requirements that distinguish the control and validation regions from the signal region are indicated in bold. Most of the kinematic quantities used to define these regions are discussed in the text. The quantity $m_T(\ell_3, E_T^{\text{miss}})$ indicates the transverse mass formed by the $E_T^{\text{miss}}$ and the lepton which is not assigned to either of the Z-decay leptons. . . . .	<b>63</b>
Table 5	List of the triggers considered for this analysis. The corresponding L1 items are included for reference. The last column notes if the trigger is available in data. . . . .	<b>65</b>
Table 6	Lepton trigger requirements used for the analysis in different regions of lepton- $p_T$ phase space.	<b>65</b>

Table 7	Yields in signal and validation regions for the flavor symmetric background. Errors include statistical uncertainty, uncertainty from MC closure, uncertainty from the $k$ and $\alpha$ factors, uncertainty due to deriving triggers efficiencies from a DAOD, and uncertainty on the MC shape used to correct for the $m_{\ell\ell}$ expansion. . . . .	69
Table 8	Background fit results from the sideband fit method. The $t\bar{t}$ MC's normalization is taken as a free parameter in the fit to data in CRT, then that normalization factor is applied in SRZ. The results are shown here both divided between the $ee$ and $\mu\mu$ channels and summed together. All other backgrounds are taken from MC in CRT, while in SRZ, the $Z/\gamma^*$ + jets contribution is taken from the $\gamma$ + jets method. The uncertainties quoted include both statistical and systematic components. . . . .	71
Table 9	Summary of the $t\bar{t}$ normalization factors calculated by the sideband fit to CRT and VRT for the 2015+2016 data. . . . .	72
Table 10	Comparison of Flavor Symmetric (FS) background predictions from the nominal method, the flavor symmetry method, and the cross-check, the sideband fit method. Uncertainties include statistical and systematic uncertainties in both cases.	72
Table 11	Control regions used to measure efficiencies of real and fake leptons. The flavour combination of the dilepton pair is denoted as either "SF" for same-flavour or "DF" for different flavour. The charge combination of the leading lepton pairs are given as "SS" for same-sign or "OS" for opposite-sign. . . . .	74
Table 12	Yields in validation regions. In VRS, data-driven background estimates are used for $Z/\gamma^*$ + jets, fakes, and FS processes. All other backgrounds are taken from MC, including all backgrounds in the multi-lepton Validation Region (VR)s. Uncertainties include statistical and systematic components. . . . .	76

Table 13	Uncertainties in the on-Z signal and validation regions. Nominal predictions are given with statistical uncertainty (including uncertainty from subtracted backgrounds), MC Closure uncertainty, uncertainty on the prediction from varying $k$ and $\alpha$ by their statistical uncertainties, comparing the efficiencies from AODs to that of DAODs, and on the $m_{\ell\ell}$ widening, which includes MC statistics and a data/MC comparison in a loosened region. . . . .	79
Table 14	Systematic uncertainties on the fake-lepton background for on-Z regions for 2015+2016 yields. The nominal yield includes statistical uncertainty from the baseline selection in a given region. The following rows indicate the results of varying the real and fake lepton efficiencies up and down by by their statistical uncertainty. Real cont. gives an uncertainty on the the contamination of real leptons in the fake lepton efficiency. $b$ -jet and no $b$ -jet indicate the impact of requiring or vetoing $b$ -tagged jets in the regions used to measure the fake efficiency. . . . .	84
Table 15	Fractional uncertainties of dibosons in signal and validation regions from Sherpa scale variations. . . . .	86
Table 16	Comparison of yields in on-Z and off-Z regions in Sherpa and Powheg diboson MC at $14.7 \text{ fb}^{-1}$ . . . . .	86
Table 17	Overview of the dominant sources of systematic uncertainty on the total background estimate in the signal regions. The values shown are relative to the total background estimate, shown in %. . . . .	87

## LISTINGS

---

## ACRONYMS

---

- IBL Insertable B-Layer  
MS Muon Spectrometer  
ID Inner Detector  
SCT Silicon Microstrip Tracker  
TRT Transition Radiation Tracker  
NN Neural Network  
CCA Connected Component Analysis  
ToT Time Over Threshold  
MDT Monitored Drift Tube  
CSC Cathode-Strip Chamber  
RPC Resistive Plate Chamber  
TGC Thin Gap Chamber  
L<sub>1</sub> Level One  
HLT High Level Trigger  
L<sub>1</sub>Calo L<sub>1</sub> Calorimeter Trigger  
L<sub>1</sub>Topo L<sub>1</sub> Topological Trigger  
CTP Central Trigger Processor  
TTC Trigger Timing and Control  
ROB Read Out Board  
RoI Region of Interest  
LHC Large Hadron Collider  
LEP Large Electron-Positron  
SPS Super Proton Synchrotron  
CMS Compact Muon Solenoid  
ALICE A Large Ion Collider Experiment  
LHCb Large Hadron Collider beauty

- RF Radiofrequency  
PSB Proton Synchrotron Booster  
PS Proton Synchrotron  
MC Monte Carlo simulation  
SM Standard Model  
BSM Beyond the Standard Model  
SUSY Supersymmetry  
QCD Quantum Chromodynamics  
PDF Parton Distribution Function  
DM Dark Matter  
NLO+NLL Next-to-Leading-Logarithmic Accuracy  
SUSY Supersymmetry  
AOD Analysis Object Data  
SR Signal Region  
VR Validation Region  
CR Control Region  
FS Flavor Symmetric



## Part I

### INTRODUCTION

The centerpiece of this thesis is a search for Supersymmetry, but it also includes all the scaffolding and background necessary to understand the search. An overview of the LHC and the ATLAS Detector are presented along with the theory that motivates the search.



## INTRODUCTION

---

The pages that follow detail the author’s work on the ATLAS experiment from 2011 through 2016, focusing on an analysis of  $13\text{TeV}$  proton-proton collisions at the [LHC](#) looking for Supersymmetry with the ATLAS Detector.

[CHAPTER 2](#) outlines the Standard Model of Particle Physics and the benefits of extending it to include Supersymmetry, then continues to describe the motivation behind searching for this particular model.

[CHAPTER 3](#) describes the [LHC](#) and its operation.

[CHAPTER 4](#) contains descriptions of the many pieces of the ATLAS detector, and how they serve to detect particles coming from [LHC](#) collisions.

[CHAPTER 5](#) presents a neural network designed to improve tracking in the ATLAS Pixel Detector, and describes the benefits of its implementation.



## Part II

### THEORY AND MOTIVATION

This section describes the theoretical foundation for the analysis presented in [Part iv](#). It includes an overview of the Standard Model, including its phenomenology in a  $p - p$  collider. The theory of Supersymmetry is explained, and the motivation for extending the Standard Model to include it is presented. In addition, this section includes an explanation of Monte Carlo generators and details about the specific form of Supersymmetry searched for in this analysis.



# 2

## THEORY AND MOTIVATION

---

The **SM** of particle physics represents all particles and interactions currently understood by the particle physics community. It is formulated using the principles of Quantum Field Theory, with the constraints of several symmetries and physical requirements to determine the rules for allowed interactions. [24] Developed in the 1960s and 70s, it has been immensely successful at predicting additional particles, and has held up to many high-precision tests. Despite this success, it has several shortcomings which point to its incompleteness. Though the **SM** is likely correct at the energies thus far probed, it may be missing key components that become more important at higher energies. Models supplementing the **SM** with additional particles and interactions are referred to as Beyond the Standard Model (**BSM**) theories.

One possible extension of the **SM** is Supersymmetry (**SUSY**), a theory which applies an additional symmetry between bosons and fermions to the **SM**, creating a spectrum of **SUSY** particles (sparticles) which interact with the particles of the **SM**. This theory motivates the search performed in [Part iv](#), and its theoretical appeals are discussed in this section, along with specific simplified models considered in the search.

### 2.1 THE STANDARD MODEL

The **SM** of particle physics describes the interactions of all of the particles currently known to exist, and consists of both matter particles and force carriers. This model has been unprecedentedly successful in predicting new particles and phenomena, including the prediction of the Higgs particle almost 50 years before its discovery in 2012, which completed the **SM**. This section describes the components of the **SM** and how they interact, focusing on the environment of the **LHC**.

The particles of the **SM** are divided into two categories: fermions and bosons. The fermions comprise all the matter described by the **SM**, and are spin- $\frac{1}{2}$  particles. The bosons, integer-spin particles, are the force carriers. They provide a mechanism to explain three of the four forces known to particle physics, with gravity still lacking a quantum formalization. The Higgs boson, the only spin-0 particle in the **SM**, provides a mechanism for giving mass to the other particles. The full **SM**, with the addition of the hypothetical graviton, is presented in [Figure 1](#).

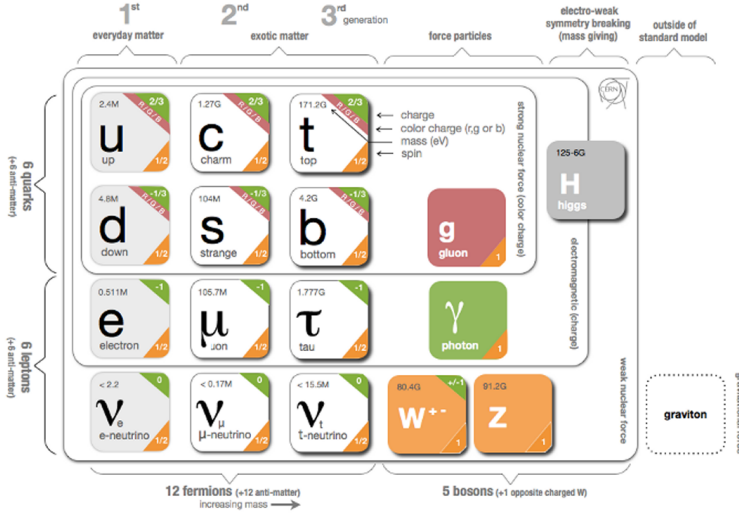


Figure 1: The Standard Model of particle physics, containing all known bosons and fermions, with the addition of the hypothetical graviton. [38]

### 2.1.1 Matter

The matter described by the SM is made up of fermions, spin- $\frac{1}{2}$  particles which can be broken into two groups, quarks and leptons. The leptons all interact weakly, while the quarks additionally interact strongly.

#### 2.1.1.1 Leptons

Leptons, as seen in the bottom left of Figure 1, come in three generations, each labeled by a flavor: electron, muon, and tau. In the case of the massive leptons, these flavors are mass eigenstates, and the generations are placed in an order based on increasing mass. Each massive lepton is negatively charged and has a positively charged anti-particle.

The three neutrinos come in the same flavors as the massive leptons, but these flavor eigenstates do not correspond exactly to mass eigenstates. As a consequence, neutrinos oscillate between flavors as they propagate through space. These oscillations are the only evidence of neutrino mass, which is bound from below by the mass splittings determined from the oscillation. Though it is still uncertain if the masses of the neutrinos follow the same hierarchy as the massive leptons, that expected ordering is slightly preferred over the inverted hierarchy. [41]

Unlike the massive leptons, the neutrinos are uncharged, and it is not yet known whether each neutrino has a separate anti-particle, or if it is its own antiparticle. Because they are uncharged, they can only interact weakly, making them extremely difficult to detect. In the AT-

LAS detector, neutrinos pass through all layers undetected, and their presence can only be inferred from the non-conservation of momentum that results in the observed particles. As a consequence of their ability to evade detection, neutrinos are the least understood particles of the SM.

The SM conserves lepton number,  $L$ , which is defined as the number of leptons minus the number of anti-leptons in a state. While this conservation is not theoretically required, its violation has not yet been observed. As a consequence of this conservation, the lightest massive lepton, the electron, is stable.

### 2.1.1.2 Quarks

Quarks, as seen in the top left of Figure 1, are also charged particles that interact weakly, but are differentiated from the leptons by their strong interactions. They are also organized in three generations ordered by mass, and come in pairs of “up-type” and “down-type” quarks, named after the lightest generation. Though the up quark is lighter than the down, that rule is reversed in the subsequent two generations. Up-type quarks are charged  $+\frac{2}{3}$ , while the down-type quarks are charged  $-\frac{1}{3}$ . Quarks are also charged under the strong interaction, whose three charges are often characterized by colors: red, green, and blue. Each quark has an anti-particle with the opposite charges.

These fractional charges and individual colors are never seen in nature because of the requirement (discussed further in Section 2.1.2.2) that stable particle states be color-neutral. To accomplish this, quarks can create two-particle bound states called *mesons* consisting of one quark and one anti-quark with the same color charge or three-particle bound states of quarks or anti-quarks with the three different color charges, which are called *baryons*. The lightest color neutral state containing only quarks, the proton ( $uud$ ), is stable. Extremely unstable bound states consisting of higher numbers of quarks can also exist, such as the pentaquark discovered in 2015 at the LHC. [52] Collectively, these multi-quark bound states are called *hadrons*.

Like leptons, the number of quarks in a state is conserved. However, because quarks cannot exist in an isolated state, that conservation described as a conservation of baryon number ( $B$ ) defined similarly to lepton number. Mesons, because they have one quark and one anti-quark, have  $B = 0$ .

### 2.1.2 Forces

The fermions in the previous section interact via the electromagnetic, weak, and strong forces. In a perturbative quantum field theory, interactions via these forces are represented by mediating bosons. These force carriers interact only with particles charged with their force’s

quantum numbers. The photon, for example, interacts only with electromagnetically charged particles. Gluons, mediators of the strong force, interact only with color charged particles, quarks and gluons. All fermions are weakly charged and interact with the weak force's mediators, the  $W$  and  $Z$  bosons.

The formulation for each of these forces is developed by requiring that the [SM](#) lagrangian be locally gauge invariant. [40] This can be accomplished by adding gauge fields to the lagrangian, whose behavior under gauge transformations cancels out the gauge dependence of the free lagrangian. However, adding a mass term for these fields reintroduces gauge dependence, so this mechanism only creates forces mediated by massless gauge bosons. The addition of the Higgs field provides mass terms the weak gauge bosons without interfering with the gauge invariance.

The total gauged symmetry group for the [SM](#) is  $SU_c(3) \times SU_L(2) \times U_Y(1)$ , with a total lagrangian which can be divided into several terms

$$\mathcal{L}_{SM} = \mathcal{L}_{strong} + \mathcal{L}_{electroweak} \quad (1)$$

each of which will be described in detail in their respective sections.

#### 2.1.2.1 The Electromagnetic Force

The simplest example of gauge invariance requirements generating a description of a force can be found in electromagnetism. It has one massless mediator, the photon, which interacts with all electromagnetically charged particles. What follows is a brief description of how enforcing this invariance generates a lagrangian of the same form as the classical electromagnetic lagrangian, which can be easily incorporated into the [SM](#).

The particles in [Section 2.1.1](#) are fermions, and so their free lagrangians are Dirac lagrangians and all follow the form

$$\mathcal{L} = i\bar{\psi}\gamma^\mu\partial_\mu\psi - m\bar{\psi}\psi. \quad (2)$$

Requiring that the free lagrangians for these particles be invariant under a  $U(1)$  local gauge transformation,  $e^{iq\lambda(x)}$ , can be accomplished by adding a term to the lagrangian which cancels the derivative term arising from  $\lambda$ 's dependence on  $x$ :

$$\mathcal{L} = i\bar{\psi}\gamma^\mu\partial_\mu\psi - m\bar{\psi}\psi - (q\bar{\psi}\gamma^\mu\psi)A_\mu \quad (3)$$

where  $A_\mu$  is a “gauge field” that transforms according to

$$A_\mu \rightarrow A_\mu + \partial_\mu\lambda. \quad (4)$$

This vector field must also come with a free term,

$$\mathcal{L} = -\frac{1}{16\pi} F^{\mu\nu} F_{\mu\nu} + \frac{1}{8\pi} m_A^2 A^\nu A_\nu. \quad (5)$$

The mass term for this field would not itself be invariant under the transformation, but the field can simply be made massless to avoid this problem. The final lagrangian, then, is

$$\mathcal{L} = i\bar{\psi}\gamma^\mu \partial_\mu \psi - m\bar{\psi}\psi - \frac{1}{16\pi} F^{\mu\nu} F_{\mu\nu} - (q\bar{\psi}\gamma^\mu \psi) A_\mu \quad (6)$$

which is precisely the original lagrangian with the addition of terms replicating the form of the Maxwell lagrangian. In a quantized interpretation, it describes a field that interacts with particles with non-zero electromagnetic charge  $q$  via interactions with a massless spin-1 boson, the photon.

For the purpose of succinct notation, this lagrangian is often rewritten in terms of the “covariant derivative”

$$\mathcal{D}_\mu = \partial_\mu + iq\lambda A_\mu \quad (7)$$

which immediately cancels the gauge dependent term created by the transformation. This mechanism is mathematically simple in the  $U(1)$  case, but can be replicated for more complicated gauge transformations with perturbative approximations.

### 2.1.2.2 The Strong Force

The strong force is generated by a similar process of requiring local gauge invariance, but in this case, for a  $SU(3)$  transformation. The interactions of the strong force are described by the theory of quantum chromodynamics, which is given by the lagrangian

$$\mathcal{L}_{strong} = -\frac{1}{4} G_{\mu\nu}^\alpha G^{\alpha\mu\nu} - \frac{1}{2} \bar{Q}_m \not{D} Q_m \quad (8)$$

where the  $\alpha$  index runs from 1 to 8 and represents the different generators of  $SU(3)$ , and  $m$  indexes the three quark generations.  $G_{\mu\nu}^\alpha$  is the field strength tensor and is defined as

$$G_{\mu\nu}^\alpha = \partial_\mu G_\nu^\alpha - \partial_\nu G_\mu^\alpha + g_3 f_{\beta\gamma}^\alpha G_\mu^\beta G_\nu^\gamma \quad (9)$$

where  $g_3$  is a function of the energy scale of the interaction  $\mu$ , and is related to the strong coupling constant by

$$\alpha_s(\mu) = g_s(\mu)^2 / 4\pi. \quad (10)$$

This first term of the lagrangian gives the gluon self-coupling interactions, with terms involving 2, 3, and 4 gluon field terms. The 2-field portion is simply the field strength tensor, but the other terms give couplings that can be described by the feynman diagrams in [Figure 2](#).

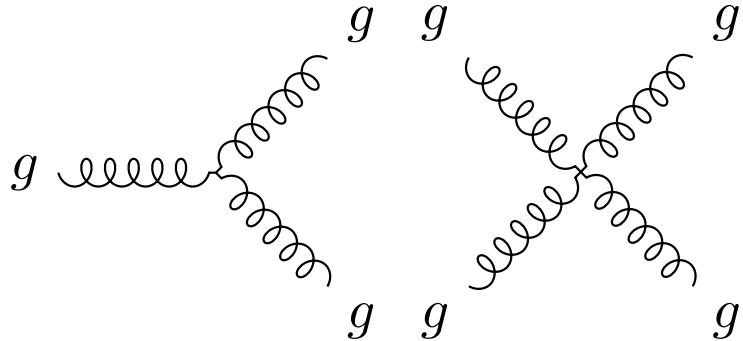


[Figure 2](#): Gluon self coupling Feynman diagrams involving 3- and 4-gluon interactions.

In the second term,  $\not{D}Q_m$  is the covariant derivative acting on the quark field. The quarks are in fact charged under all three forces, strong, electromagnetic, and weak, so the covariant derivative includes terms to make each of the force's lagrangians gauge invariant. Thus this term introduces quark-boson interactions of four types, seen in [Figure 3](#). The quarks' coupling to the gluon is the strongest, with the other couplings happening at lower rates. The couplings to the W and Z bosons will be described in [Section 2.1.2.3](#).

The canceling required to make the lagrangian gauge invariant is actually only satisfied to a first order expansion of the transformation, guaranteeing its validity only for infinitesimally small perturbations from the ground state. However, the strong coupling constant,  $\alpha$ , depends on the energy scale of the interaction, decreasing at higher energy scales and asymptotically increasing at low energies. [Figure 4](#) shows this effect translated to distance scales, demonstrating that QCD is weak and can be considered perturbatively at small distance scales, but at large distance scales this approximation breaks down, and the colorless hadrons introduce in [Section 2.1.1.2](#) must be used to describe interactions instead.

The boundary between these regimes is referred to as  $\Lambda_{QCD}$  and differentiates energies at which quarks can be considered free particles and the energies at which they must instead be described by their colorless bound states. The [LHC](#) is capable of producing individual quarks, but they instantaneously hadronize, producing showers of colored particles referred to as “jets”.

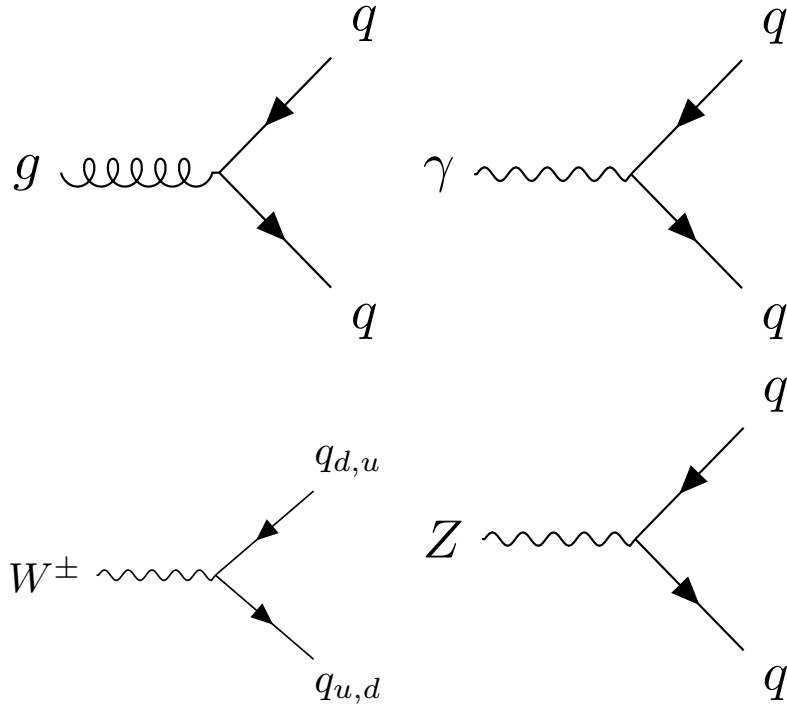


Figure 3: Quark couplings to the different types of gauge bosons. The  $q_{u,d}$  labels represent any up- or down-type quarks.

#### 2.1.2.3 The Weak Force

A similar process, using an  $SU(2)$  gauge transformation, can produce a lagrangian that would suffice to describe the  $W$  and  $Z$  bosons of the [SM](#), if only they were massless. However, they are not, so an alternate mechanism must be used to add masses to the lagrangian.

Before a mechanism for their masses was understood, and before they were discovered, the large mass of the  $W$  and  $Z$  bosons were proposed in order to unify the electromagnetic and weak forces into the electroweak force. The large masses were crucial to explain the discrepancy in the strength of the two forces.

This unified theory resulted in a triplet,  $W$ , with coupling  $g_W$ , and a singlet field  $B$ , with coupling  $g'/2$ . However, this electroweak symmetry is broken, and mixing between these states occurs. Rewritten in their mass basis, the more familiar electroweak force carriers are produced:  $W^\pm$ , two states with identical coupling resulting from the first two states of the  $W$  triplet, then  $Z^0$  and the photon field  $A$  resulting from the mixing of the last  $W$  state and  $B$ .

The electroweak lagrangian is much more complicated than the strong lagrangian, and can be divided into several terms:

$$\mathcal{L}_{\text{electroweak}} = \mathcal{L}_{\text{gauge}} + \mathcal{L}_{\text{fermions}} + \mathcal{L}_{\text{Higgs}} + \mathcal{L}_{\text{Yukawa}}. \quad (11)$$

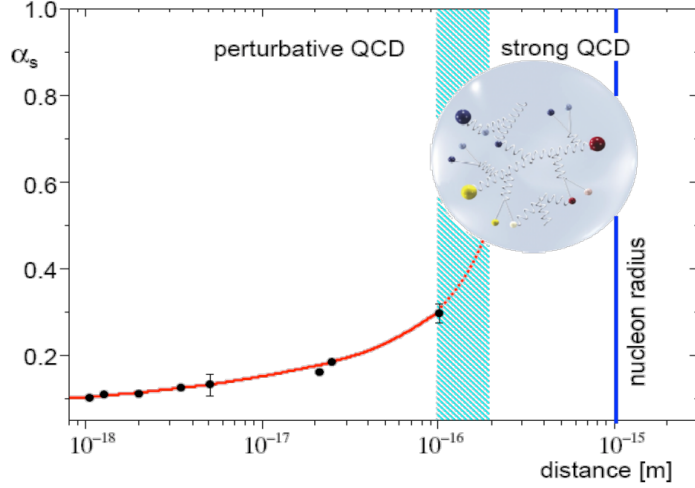


Figure 4: The running of the strong coupling constant,  $\alpha_s$ . [50]

The first term can be written as follows

$$\mathcal{L}_{gauge} = -\frac{1}{4}W^{a\mu\nu}W_{\mu\nu}^a - \frac{1}{4}B^{\mu\nu}B_{\mu\nu} \quad (12)$$

where the  $a$  indices are numbered 1 through 3 and indicate the generators of  $SU(2)$  and is written

$$W_{\mu\nu}^a = \partial_\mu W_\nu^a - \partial_\nu W_\mu^a + g_2 \epsilon_{abc} W_\mu^b W_\nu^c \quad (13)$$

The gauge portion of the lagrangian then generates interaction terms of between the three  $W$  fields, which when rewritten in terms of the mass-eigenstate basis, generates interactions like the ones in Figure 5.

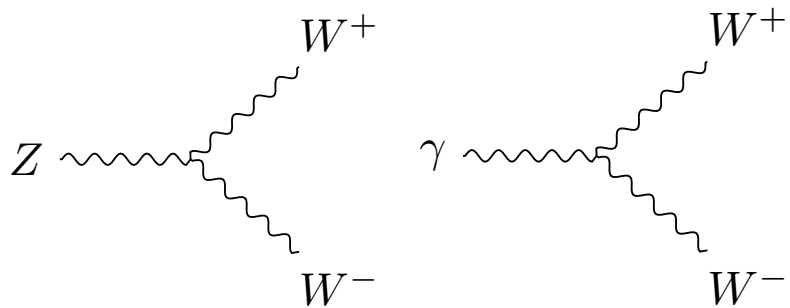


Figure 5: Trilinear gauge couplings in the SM.

The fermion portion of the lagrangian is written as

$$\begin{aligned}\mathcal{L}_{fermion} = & -\frac{1}{2}\bar{L}_m \not{D} L_m - \frac{1}{2}\bar{Q}_m \not{D} Q_m \\ & -\frac{1}{2}\bar{U}_m \not{D} U_m - \frac{1}{2}\bar{D}_m \not{D} D_m \\ & -\frac{1}{2}\bar{E}_m \not{D} E_m\end{aligned}\tag{14}$$

with the inclusion of the quark term already mentioned in [Section 2.1.2.2](#) for completeness. \*\*\*\* finish this with an explanation of handedness and and then draw feynman diagrams then move on to mass terms and into higgs mechanism. Figure out what to do with neutrino masses. Maybe make Higgs chapter a subsection called electroweak symmetry breaking.

#### 2.1.2.4 The Higgs Mechanism

The reason for this symmetry breaking has to do with the final piece of the [SM](#), the Higgs boson. The Higgs mechanism presents an alternate way to generate a mass term, through an unexpected route. It is a scalar field, with a lagrangian

$$\mathcal{L} = \frac{1}{2}(\partial_\mu \phi)^*(\partial^\mu \phi) + \frac{1}{2}\mu^2 \phi^* \phi - \frac{1}{4}\lambda^4 (\phi^* \phi)^2\tag{15}$$

where  $\phi$  is a complex scalar field,  $\phi = \phi_1 + i\phi_2$ . This looks very similar to the standard scalar field, but the signs on the mass and interaction terms are reversed, giving a result that looks like an imaginary mass. However, this lagrangian differs from all previously considered lagrangians in that its ground state does not occur at  $\phi = 0$ . Because this is a perturbative theory, its validity only holds when expanded around the ground states, which must satisfy

$$\phi_1^2 + \phi_2^2 = -\frac{\mu}{\lambda}\tag{16}$$

Rewriting the original lagrangian in terms of fields centered around ground states chosen to satisfy that condition results in a reasonable mass term. However, in an effect called “spontaneous symmetry breaking”, the original  $SO(2)$  rotational symmetry of the lagrangian is lost, resulting only in a  $U(1)$  rotational symmetry; the lagrangian is invariant under a phase transformation.

As in [Section 2.1.2.1](#), it is possible to make the lagrangian invariant under a local  $U(1)$  transformation,  $\phi \rightarrow e^{i\theta(x)\phi}$  by adding a massless gauge field  $A^\mu$  and using the covariant derivative. Due to the many cross terms from the non-zero ground state, terms for the mass of one of the bosons as well as the gauge field appear, leaving only one

massless boson. The massless boson, it turns out, can be completely removed from the theory via local  $U(1)$  transformations, ultimately producing a theory with one massive scalar (the Higgs) and a massive gauge field.

### 2.1.3 Phenomenology of Proton-Proton Collisions

As discussed in [Chapter 3](#), the [LHC](#) collides bunches of high-energy protons, and the interactions of these protons' constituent quarks produce the wide array of particles seen in the ATLAS detector. The [LHC](#) typically cites its energy in terms of  $\sqrt{S}$ , the center of mass energy of protons in the two colliding beams. However, because the proton is not fundamental, this energy is divided among many particles that make up the proton.

To first order, a proton consists of three quarks: two up quarks and one down quark. However, a real quantum mechanical system is much more chaotic, with other quarks popping into and out of existence and gluons flying between them. These additional quarks are called "sea" quarks. The particles inside the proton can have a wide range of energies depending on the internal dynamics at the moment of the collision. These cannot be predicted exactly, but probabilistic models called [PDFs](#) describe the likelihood of any given configuration. These models are determined using data from hard scattering experiments and give probabilistic estimates for how often a given type of particle appears with a fraction  $x$  of the total proton energy, as seen in [Figure 6](#).

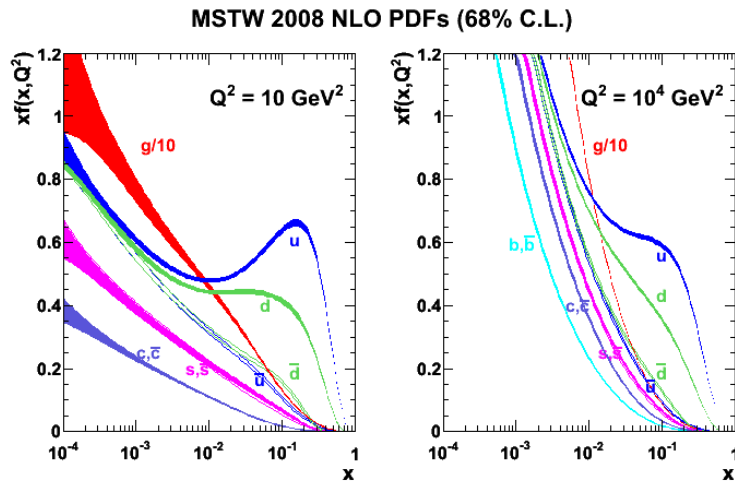
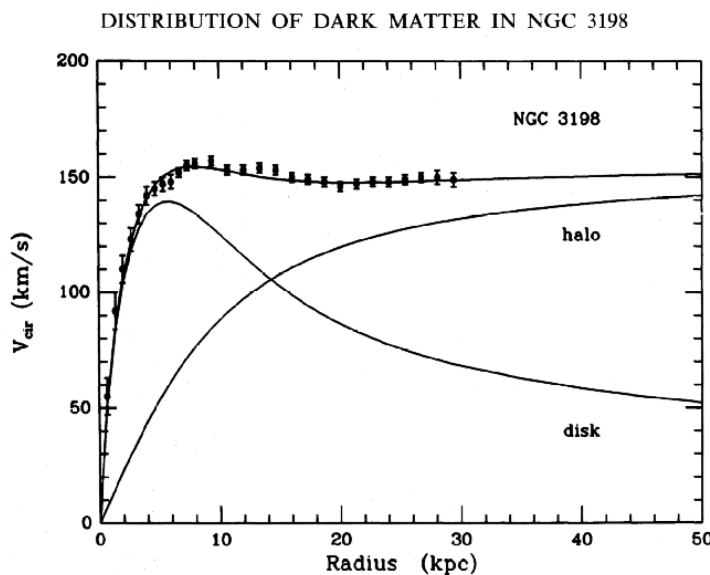


Figure 6: 2008 MSTW [PDFs](#) for various particle types. [48]

### 2.1.4 Problems in the Standard Model

Thought the [SM](#) is a self-consistent theory that describes to great accuracy all of the particles and forces it includes, it does have certain shortcomings. The most glaring is the omission of gravity. Though the force is well understood at large scales via the theory of General Relativity, no satisfying quantum description of gravity has been accepted, much less proven. The Planck scale, the energy scale at which gravitational interactions become large enough that no sound theory can ignore gravity, is at about  $10^{28}$  eV, 16 orders of magnitude above the electroweak scale.

Another clear omission of the [SM](#) is Dark Matter ([DM](#)). This matter was first identified in 1933 through the observation of galactic rotation curves. [51] The speed of rotation indicated both that there was more mass in the system than could be accounted for by observations made directly of the galaxy, and that this additional matter was distributed in a halo, not a disk like the typical luminous matter. This effect can be seen in [Figure 7](#). Since then, the gravitational impact of [DM](#) has been observed in colliding clusters and many more rotational curves, but it has never been directly detected or seen at a particle accelerator. As a consequence, very few details are known about the nature of the particles that make up this matter, only that it does not interact strongly or electromagnetically and its density throughout the universe.



[Figure 7](#): Galactic rotation curve showing that the discrepancy between the observed luminous matter and the total mass in the system can be described as a non-luminous halo of matter. [53]

Beyond the omissions of the [SM](#), there are several aesthetic problems - things that could have no solution, but seem to suggest that

the current [SM](#) are missing some pieces that could unify it and provide more order. The first is the sheer number of parameters in the [SM](#). There are 26 independent parameters determining the mass of the particles and all the couplings between them. Besides the rough grouping of fermions into generations, there seems to be no order to masses of particles, and no way to predict the masses or couplings. Each, it seems, is independently provided by nature.

In the past, large numbers of seemingly unrelated parameters has indicated that a theory has a more fundamental form at shorter distance scales. The large number of elements, it turned out, could be explained by different groupings of three particles, the proton, neutron and electron. Later, the menagerie of hadrons became so large that a similar reimagining of what was fundamental took place, and the theory of quarks gave an order to the many mesons and baryons. This pattern leaves physicists suspicious of any theory with too many particles and free parameters, suggesting that perhaps, at a higher energy, there is a simpler model that can unify many of the seemingly disparate elements of the [SM](#).

However, some of these seemingly independent parameters have suspicious symmetry. The Higgs mass, for example, has been measured to be 125 GeV. This mass is the sum of the bare mass, the one that appears in the lagrangian, and quantum corrections from interactions with other particles, which are proportional to the square of the particles' mass. Since new physics must exist at the Planck scale to account for gravity, these corrections could be up to 35 orders of magnitude larger than the Higgs mass. The bare mass could theoretically cancel out this massive correction, these parameters should be independent, and the odds that they would be precisely the same to 35 places are very, very small. This exact canceling is often called "fine-tuning", an undesirable trait in a theory which suggests that some more fundamental symmetry has been missed. The word "naturalness" is used to describe the extent to which a theory is free of fine-tuning.

## 2.2 SUPERSYMMETRY

[SUSY](#) was proposed and developed in the 1970s to give solutions to many of these [SM](#) shortcomings. The theory works by extending the [SM](#) to include a symmetry between fermions and bosons. This requires the existence of many new particles - a bosonic "sfermion" for each fermion of the [SM](#) and a fermionic "gaugino" for each of the gauge bosons. These superpartners of [SM](#) particles should have identical quantum numbers to the original particle, except for their spin. [Figure 8](#) shows the [SM](#) particles and their superpartners.

Of course, if there were a "selectron", for example, with identical mass to the electron, it would have been detected long ago. In fact,

such a particle would fundamentally change atomic structure, with the bosonic selectrons capable of piling into the ground state of an atom, and removing all the interesting valence-shell interactions of electrons that determine molecular structure. Thus, if SUSY does exist, the symmetry must be broken, with much higher masses for the superpartners than the original SM particles.

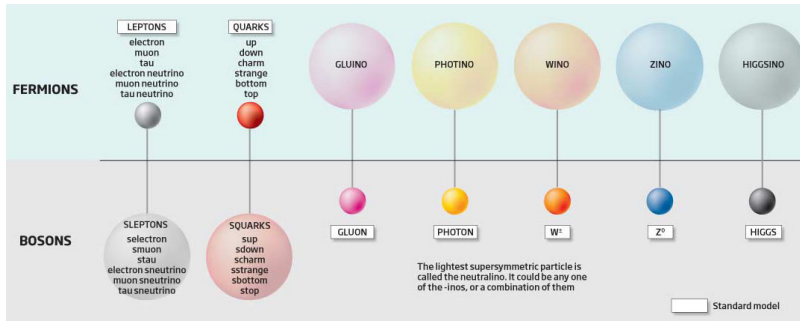


Figure 8: SM particles and their superpartners, with mass very roughly indicated by size. [newscientist-pz]

### 2.2.1 Supersymmetry Phenomenology

[49]

### 2.2.2 Solutions to Standard Model Problems

Many believe that a complete SM would include a unification of the three forces, as electromagnetism and the weak force have already been unified. This requires that at some higher energy, the coupling constants of all three forces merge.

### 2.2.3 Supersymmetry Signatures in $p - p$ Collisions

#### 2.2.3.1 Simplified Models Used in This Analysis

## 2.3 MONTE CARLO GENERATORS



## Part III

### THE EXPERIMENT

This section describes the [LHC](#) and the ATLAS detector, which collectively provide the physical environment and the data collection for the analysis discussed in [Part iv](#).



# 3

## THE LARGE HADRON COLLIDER

The LHC is unique in the world, producing proton-proton collisions at energies an order of magnitude higher than any accelerator before [37]. It provides unique environments at its collision points where massive, unstable particles can exist for an instant, then decay to the ordinary material of the universe. It is the goal of the ATLAS experiment to identify these short-lived particles, but LHC's work of producing them is equally complex.

The LHC sits in a 26.7 km circular tunnel that straddles the French-Swiss border outside of Geneva, originally built in 1989 for the Large Electron-Positron (LEP) collider [46]. In the LHC, two beams of protons are accelerated to 6.5 TeV, then focused and collided at four points around the ring, which can be seen in Figure 9. These points are each encased by particle detectors, which can examine the outputs of the collisions, and have different strengths and goals. The two multipurpose detectors are ATLAS and Compact Muon Solenoid (CMS), which have very complex detectors aimed and measuring as many SM particles as possible and discovering new processes [3, 33]. Large Hadron Collider beauty (LHCb) examines processes related to the  $b$  quark [34]. Meanwhile, A Large Ion Collider Experiment (ALICE) focuses on special runs of the LHC which collide lead ions instead of protons, and seeks to understand the high energy densities resulting from the collisions of such massive, complex particles [32].

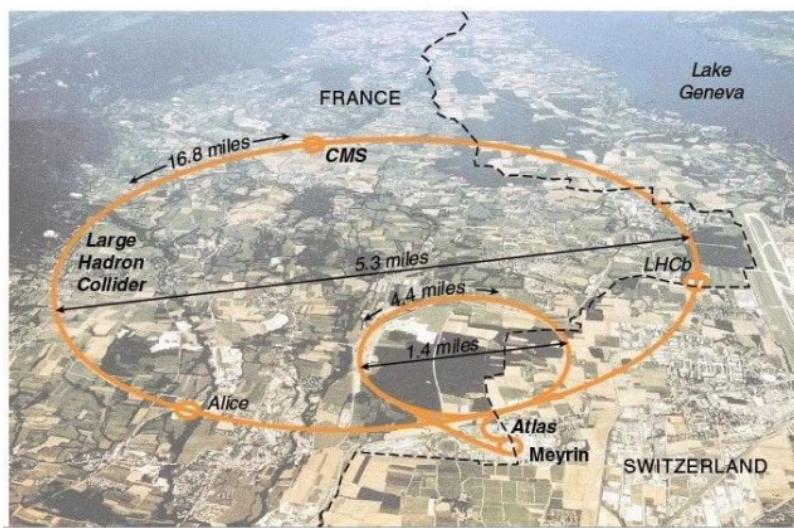


Figure 9: The LHC main collider ring and pre-accelerator SPS overlaid on a map of Switzerland and France, with the four main LHC experiments identified.

### 3.1 THE INJECTOR COMPLEX

The goal of the LHC is to provide high luminosity proton-proton collisions at 13 TeV. To achieve this, it must be capable of rapidly accelerating large numbers of protons and holding them at a constant energy, and organizing them into bunches which can be focused and collided at precise points and times. To do this, a complex system of pre-accelerators are required, as well as a precisely engineered system of magnets withing the LHC. The full system of pre-accelerators is shown in Figure 10.

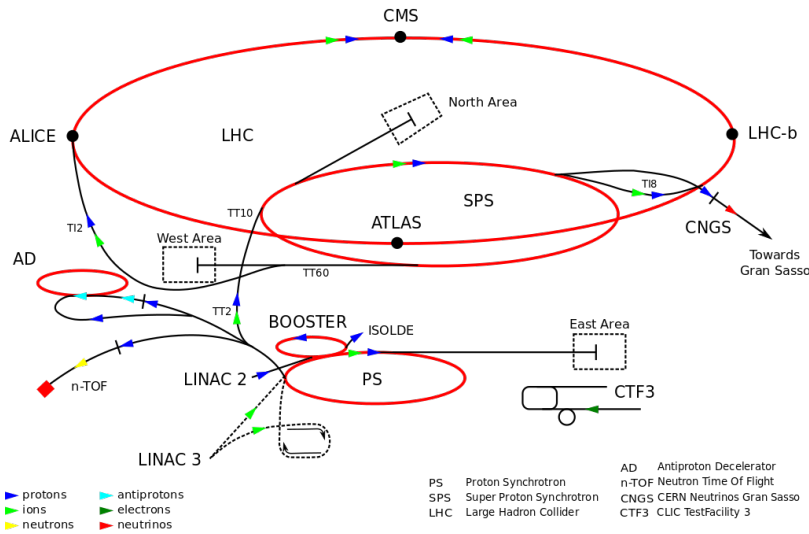


Figure 10: The pre-accelerators of the LHC.

The chain begins with when hydrogen gas is stripped of its electrons and injected in short pulses into Linac2, a linear accelerator which uses Radiofrequency (RF) cavities, which use alternating positive and negative electric fields to simultaneously push and pull particles forward through the accelerator. This RF behavoir keeps the bunches of protons resulting from the original pulses separated, beginning the formation of the bunch structure used for collisions. Quadropole magnets along the accelerator keep the beam focused. By the end of the accelerator, protons have reached 50 MeV.

The proton beam is then injected into the Proton Synchrotron Booster (PSB), the first circular accelerator in the pre-accelerator chain. It increases its magnetic field as the protons increase in speed, ultimately accelerating them to 1.4 GeV.

At this point the proton moves on to the PS, a 600 m long circular accelerator that consists of 277 electromagnets that accelerate the protons up to 25 GeV, and 100 additional dipole magnets to bend the beam.

The last accelerator before injection into the LHC is the SPS, a 7 km long ring which is responsible for the discover of the  $W$  and  $Z$  bosons.

The [SPS](#) accelerates particles up to 450 GeV before they are launched into the [LHC](#).

Proton bunches are structured for ease of acceleration, with distinct features resulting from each of the pre-accelerators. The [PS](#) produces 72 bunches separated by 25 ns, which are injected into the [SPS](#), as seen in [Figure 11](#). However, as the magnetic field directing these protons out of the [PS](#) loop is turned on, there must be a gap in the bunch structure. Without this gap, called the injection kicker rise time, the changing magnetic field would direct particles out of the accelerator and produce high amounts of unsafe radiation around the [PS](#). A similar gap in bunch structure is required for the injection from the [SPS](#) to the [LHC](#). The injection process is repeated until the [LHC](#) is completely filled with around 2000 bunches, which takes about three minutes.

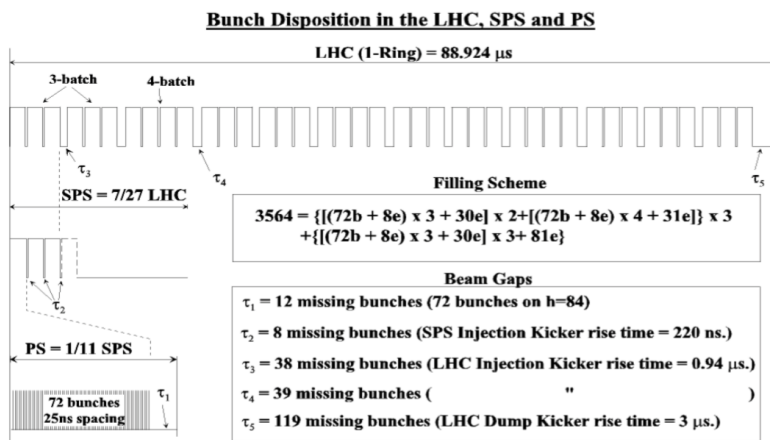


Figure 11: Bunch structure in the [PS](#), [SPS](#), and [LHC](#).

### 3.2 OPERATION OF THE LARGE HADRON COLLIDER

The [LHC](#) consists of eight straight sections each connected by an arc. In each straight section, [RF](#) cavities accelerate protons, ultimately bringing them up to 6.5 GeV. Between these straight sections, 8.4 T dipole magnets bend the beams to maintain the approximately circular path. However, because the [LHC](#) is a proton-proton collider as opposed to a proton-antiproton collider, the two counter-rotating beams must be housed in separate rings and accelerated separately. To achieve this, twin-bore superconducting magnets, one example of which can be seen in [Figure 12](#), surrounds the two rings and accelerates them both. Quadropole magnets are used at the four collision points to focus the beams, which cross at an interaction point at the center of a detector. In total there are 1232 main dipole magnets over 5000 additional magnets, which are all superconducting and kept below their critical temperatures by liquid helium cooling.

### LHC DIPOLE : STANDARD CROSS-SECTION

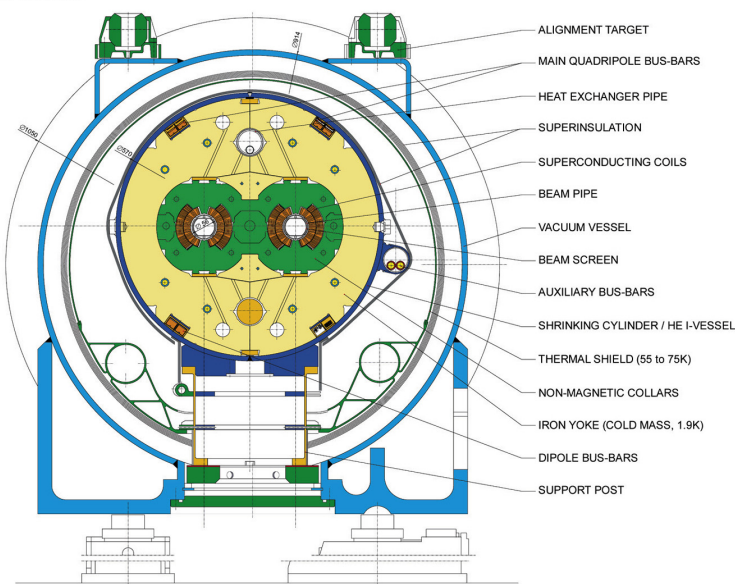


Figure 12: Cross-section of a cryodipole magnet in the LHC.

When first injected into the LHC, the protons must be accelerated over many turns through the machine, with the magnetic field from the dipoles increasing with each pass to apply more force with which to bend the beam. Once the protons have reached a maximum energy, a process called “squeezing” occurs, in which the total transverse area of the beam is reduced and bunches are elongated slightly. The shape produced by this process determines the “beam spot” for the ATLAS detector, the measurement of the area in which collisions occur within the detector. As shown in Figure 13, the collisions all occur very close together in the  $x - y$  plane, but have a long spread in the  $z$  direction.

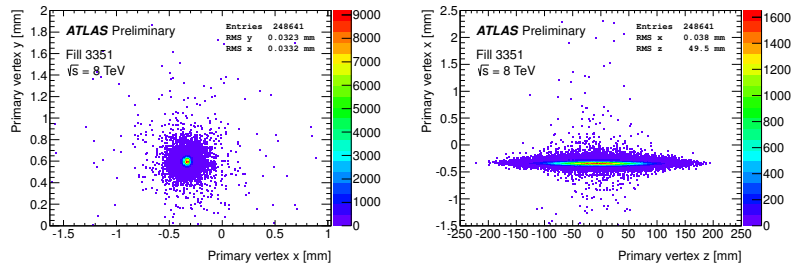


Figure 13: Beam spot in the ATLAS detector for one run in 2015. Distributions show only the highest  $p_T$  vertex per event. Left is the  $x - y$  distribution of vertices, while the right plot shows the  $x - z$  distribution.

Once the beams are at a stable energy and have been squeezed, the LHC indicates that it is physics-ready to the experiments around the ring, and, after some additional checks by each experiment, data-

taking can begin. As collisions occur, the beam is depleted, and when it is sufficiently depleted to require a new fill, or if any instability occurs, the beam is dumped into a cavern full of steel and concrete, which can absorb the energy.

### 3.3 LUMINOSITY

The goal of the collisions provided by the [LHC](#) is to produce [SM](#) and [BSM](#) particles, which can be observed by the detectors. How frequently a given process could occur was a crucial consideration in its design. The number of events of a given type is given by

$$N_{event} = \mathcal{L}\sigma_{event} \quad (17)$$

where  $\mathcal{L}$  is the luminosity delivered by the [LHC](#) and  $\sigma_{event}$  is the cross-section of the process in question. These cross-sections vary over many orders of magnitudes for different processes, as shown in [Figure 14](#), a plot of many different [SM](#) cross-sections. As a consequence, a very large amount of luminosity is required to produce the more rare events, and to have enough statistical power to differentiate them from other much more common events.

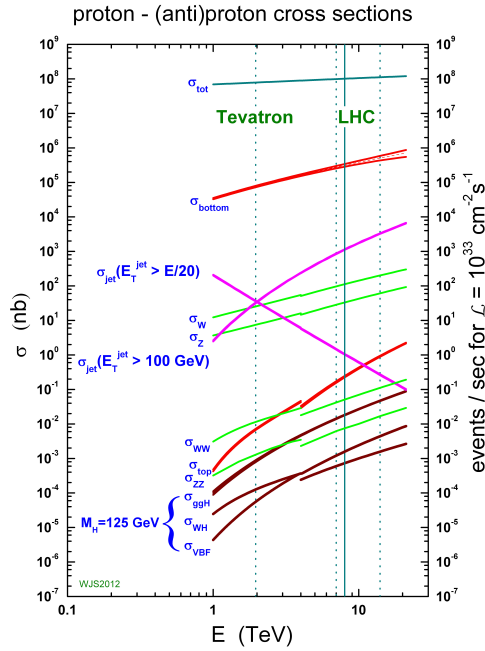


Figure 14: Cross-sections for many [SM](#) processes at the Tevatron and [LHC](#) [1].

The instantaneous luminosity at the [LHC](#) is given by

$$\mathcal{L} = \frac{N_b^2 n_b f_{rev} \gamma_r}{4\pi\epsilon_n \beta_*} F \quad (18)$$

where  $N_b$  is the number of protons per bunch ( $\sim 10^{11}$ ),  $n_b$  is the number of bunches in each beam ( $\sim 10^3$ ),  $f_{rev}$  is the number of times per second that the beam travels around the ring,  $\gamma_r$  is the relativistic gamma factor,  $\epsilon_n$  is the normalized transverse beam emittance, and  $\beta^*$  is the  $\beta$ -function at the collision point, which describes the transverse displacement of particles in the beam.  $F$  gives the reduction factor due to the geometry of the beam crossings, and is given by

$$F = \left(1 + \left(\frac{\theta_c \sigma_z}{2\sigma^*}\right)^2\right)^{-1/2} \quad (19)$$

where  $\theta_c$  is the crossing angle of the beams,  $\sigma_z$  is the RMS of the bunch length in the  $z$  direction, and  $\sigma^*$  is the same in the transverse direction.

As the proton beams circulate and collide,  $N_b$  decreases, producing a falling instantaneous luminosity, as seen in Run 1 example in [Figure 15](#). In Run 2, peak instantaneous luminosity was brought up to  $10^{34} \text{ cm}^{-2}\text{s}^{-1}$ . This high instantaneous luminosity and consistent running resulted in much faster data collection than in Run 1, as seen in [Figure 16](#).

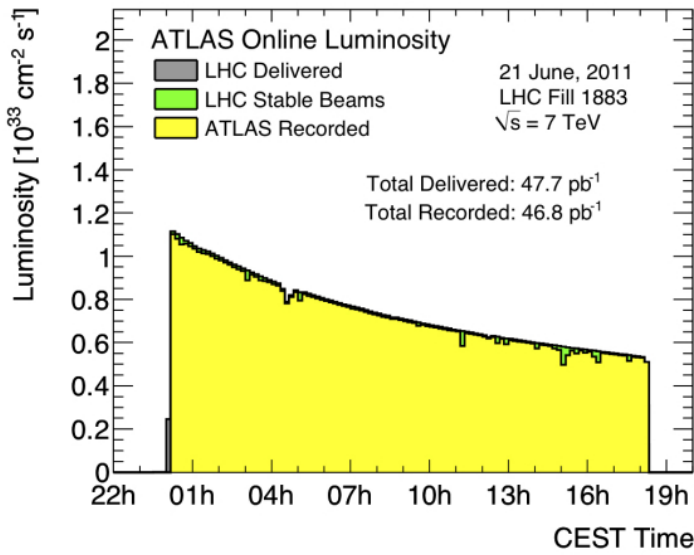


Figure 15: Instantaneous luminosity of one fill of 7 TeV data in 2011.

### 3.4 PILE-UP IN $p - p$ COLLISIONS

One consequence of the high instantaneous luminosity is “pile-up”, or multiple simultaneously interactions. Because each bunch has on order 100 billion protons, it is very likely that multiple protons will collide in the same bunch crossing. In fact, the average number of simultaneous interactions in 13 TeV data, shown in [Figure 17](#), is about twenty.

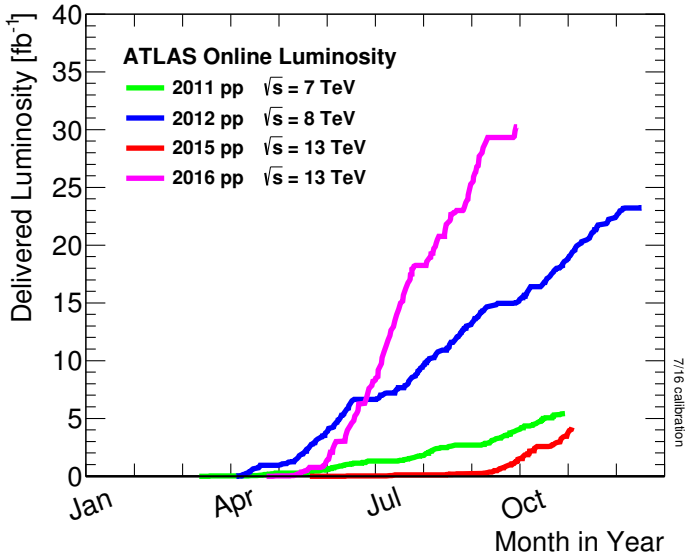


Figure 16: ATLAS luminosity for Run 1 and Run 2, as of September 2016.

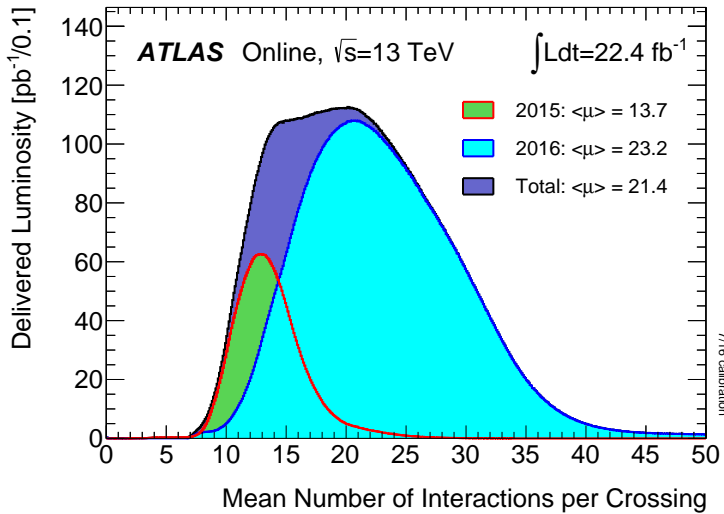


Figure 17: Average number of interactions per crossing shown for 2015 and 2016 separately, as well as the sum of the two years.

Pile-up can be a difficult challenge for the ATLAS collaboration because it typically results in additional jets in an event, and can increase SM backgrounds for analyses seeking to identify events with jets. It can also add to the overall hadronic energy of an event, and that energy can be mis-assigned to other objects. Fortunately, it is typically possible to resolve the different vertices that each proton-proton collision makes, and so pile-up jets can be identified and rejected.



# 4

## THE ATLAS DETECTOR

The ATLAS detector circumscribes the LHC’s beam pipe, enclosing the collision point with a series of particle detecting layers, aimed at making as many measurements of the particles leaving the collision point as possible. Its goal is to get a precise measurement of all the stable or semi-stable particles flying from proton-proton collisions at its center, allowing analyzers to fully reconstruct the kinematics of the underlying processes.

The ATLAS detector is the largest detector of its kind, measuring 44 m in length and 25 m in height, as seen in Figure 18. The size is mainly determined by the constraints of the MS, discussed in Section 4.4, which is the largest and outermost subsystem. The MS is submerged in a spatially varying magnetic field provided by three toroidal magnets, while the ID (Section 4.2) is encased by a superconducting solenoid, which provides a uniform 2 T field throughout its volume [3].

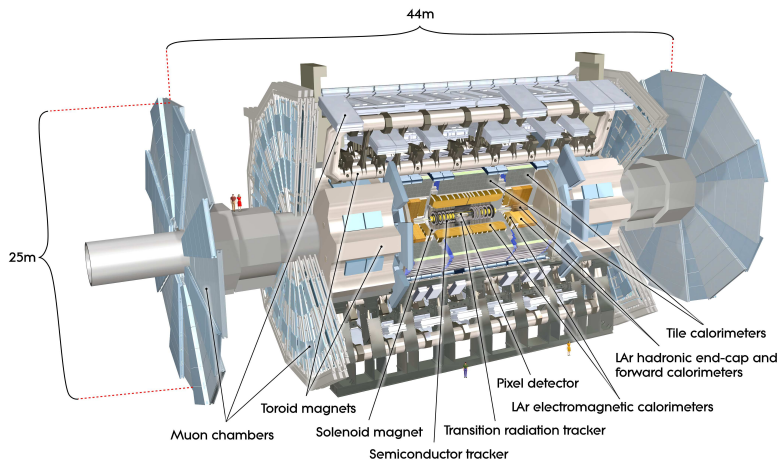


Figure 18: Diagram of the ATLAS detector, with subsystems and magnets identified.

### 4.1 COORDINATE SYSTEM USED IN THE ATLAS DETECTOR

The ATLAS detector is centered around the  $p - p$  collision point, and is built radially out from the beam pipe, maintaining as much rotational symmetry around the beam pipe as possible. It is also symmetric in the forward-backward directions. A coordinate system using the collision point as the origin is used, with the beam line defining

the  $z$ -axis. The positive  $x$  direction is defined as pointing to the center of the [LHC](#) ring, while the positive  $y$  direction points upwards. For ease of reference, the side of the detector in the positive- $z$  direction is referred to as the A side, and the other side is referred to as the C side.

Because of the cylindrical design of the detector, angular coordinates are often used. The azimuthal angle  $\phi$  defines the angle around the beam pipe and the polar angle  $\theta$  defines the angle from the beam axis ( $z$ ). However, a transformation of the polar angle called pseudo-rapidity ( $\eta$ ) is used more often, and is defined as

$$\eta = -\ln[\tan \frac{\theta}{2}]. \quad (20)$$

Building on this variable definition, distance between objects is typically defined as

$$\Delta R = \sqrt{\Delta\eta^2 + \Delta\phi^2}. \quad (21)$$

Often variables are defined purely in the transverse plane, which is indicated by a subscripted  $T$ , as in  $p_T$ , which gives an object's transverse momentum.

## 4.2 THE INNER DETECTOR

The Inner Detector ([ID](#)) is responsible for the production of tracks, predictions of the paths charged particles take as they travel through the detector. Collisions in the detector can produce about 1000 particles, so identifying and differentiating all the tracks resulting from a collision is both a hardware and a computational challenge.

The [ID](#) consists of three separate subdetectors, each of which has multiple layers capable of producing an electrical signal, called a “hit”, when a charged particle travels through its active material. ATLAS tracking software considers all these hits and forms tracks, with the goal of minimizing fake tracks due to random noise and maximizing the efficiency of identifying a real particle. Some details of this process is discussed in [Chapter 6](#). The full [ID](#) can be seen in [Figure 19](#), while a schematic in [Figure 20](#) shows more detail on the placement of each layer.

### 4.2.1 *The Pixel Detector*

The Pixel detector lies closest to the beam pipe of the [LHC](#), and has four layers comprising 92 million pixels. There are three standard layers, referred to as Layers 0-2 (L<sub>0</sub>, L<sub>1</sub>, L<sub>2</sub>), and an additional layer added for the 2015 data-taking, called the Insertable B-Layer ([IBL](#)).

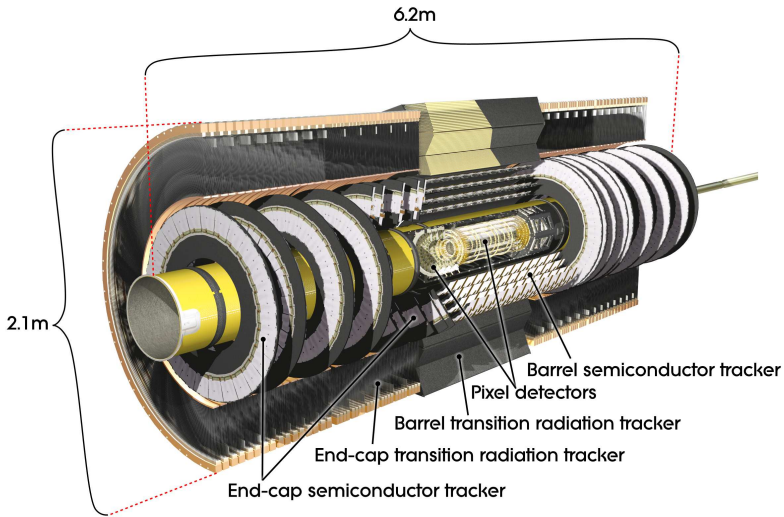


Figure 19: Diagram of the ATLAS Inner Detector, containing the Pixel, SCT, and TRT subsystems.

#### 4.2.1.1 *The Original Pixel Detector*

The Pixel Detector consists of high-precision silicon chip pixel sensors, with 1744 modules in total. Each module is identical, containing 47232 pixels, which are typically each  $50 \times 400 \mu\text{m}^2$ .

As shown in Figure 20, the central  $\eta$  region (barrel) is covered by three concentric cylindrical layers of sensors, while the higher  $\eta$  region (endcap) is covered by a series of three disks positioned in the  $x - y$  plane. Together, they give complete coverage out to  $|\eta| = 2.5$ , and a particle coming from the collision point will typically produce hits in three layers.

A pixel module consists of a sensor with mounted read-out electronics. The sensors are n-type silicon wafers with a voltage applied, and a passing charged particle produces thousands of electron-hole pairs inside the material, which drift in the electron field towards the mounted read-out system. A hit occurs when the resulting current becomes large enough to pass a threshold meant to suppress noise. A larger total charge deposit will result in the signal remaining over the threshold for a longer period of time. The initial timing of the hit, and the **ToT** are both recorded. This measurement is spatially accurate in the barrel (endcap) to  $10 \mu\text{m}$  in the  $R - \phi$  direction and  $115 \mu\text{m}$  in the  $z (R)$  direction.

#### 4.2.1.2 *Addition of the IBL*

In 2014, the **IBL** was added to the Pixel Detector. This layer sits on top of the beam pipe, inside barrel Lo, providing a measurement of particles only about 3 cm away from the interaction point. Its addition provides greater precision for all track measurements, but it's especially useful for the detection of  $B$  mesons, whose non-trivial

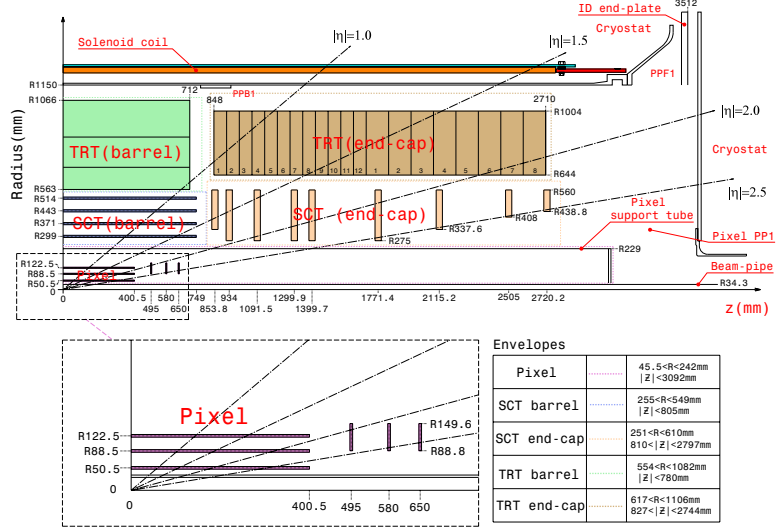


Figure 20: Diagram of one-quarter of the ATLAS Inner Detector in the  $R - z$  plane, with lines drawn to indicate various  $\eta$  locations.

lifetimes create secondary vertices in ATLAS events. The location of the **IBL** gives a measurement closer to these secondary vertices, and its increased pixel density increases the probability that these vertices can be resolved.

#### 4.2.2 The Silicon Microstrip Tracker

The Silicon Microstrip Tracker (**SCT**) employs a similar technology to the Pixel Detector, with 15912 sensors and 6.3 million readout channels. Its difference from the Pixel Detector is in the readout, which is performed by a series of 12 cm long strips with a width of 80  $\mu\text{m}$ . These layers are paired, placed on top of one another at a small (40 mrad) angle to allow for position determination in both directions, giving 4 spatial measurements for each particle passing through the **SCT**. In the barrel, these strips run parallel to the beam pipe, while in the endcap, they are arranged radially. These strips have a resolution in the barrel (endcap) of 17  $\mu\text{m}$  in the  $R - \phi$  direction and 580  $\mu\text{m}$  in the  $z$  ( $R$ ) direction.

#### 4.2.3 The Transition Radiation Tracker

The Transition Radiation Tracker (**TRT**) uses 4mm diameter gas-filled tubes, each with a high voltage wire suspended along the center of the tube. The tubes run the length of the barrel, with a separate wire in the positive and negative  $z$  direction. In the endcap, the tubes are arranged radially. In total, there are about 351,000 readout channels in the **TRT**. This detector makes measurements only in the  $R - \phi$  direction, where the resolution of each measurement is 130  $\mu\text{m}$ , and

coverage extends to  $|\eta| = 2.0$ . Each particle typically creates about 36 hits as it passes through the [TRT](#).

Particles passing through the gas mixture of the [TRT](#) ionize the gas, producing electrons which drift towards the wire due to a potential difference applied between it and the straw. The [TRT](#) also responds to low-energy transition radiation photons, which produce a much larger signal than charged particles passing through the detector. Because of this strong difference in signals, hits from the [TRT](#) are used to help differentiate between electrons and photons in the detector.

#### 4.3 THE CALORIMETERS

Unlike the tracking detectors, which aim to take measurements of a particle with minimal alterations of its trajectory, the calorimeters measure the energy of objects by stopping them entirely. The calorimeters, which can be seen in [Figure 21](#), provide coverage out to  $|\eta| < 4.9$ . High granularity electromagnetic measurements are made within  $|\eta| < 2.5$  to complement the [ID](#)'s tracking capability. In this range, high  $p_T$  electrons and photons have nearly straight tracks, making momentum measurement through track curvature difficult, leaving the calorimeter as the primary energy measurement. The hadronic calorimeters, as well as the higher  $|\eta|$  electromagnetic calorimeters, have a coarser granularity.

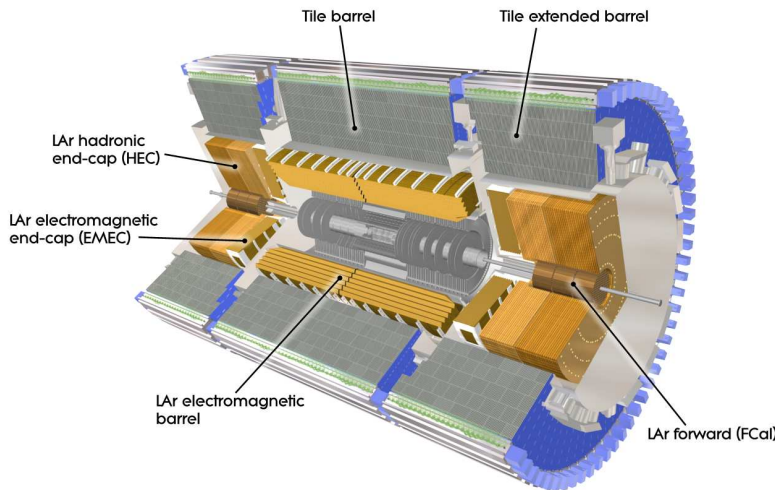


[Figure 21](#): The calorimeter system of the ATLAS detector.

Another task of the calorimeter system is to limit punch-through to the [MS](#), described in [Section 4.4](#). All other particles must be fully stopped by the calorimeters to allow for clean signals from muons, and to measure the total energy of the particle. This requirement sets a minimum number of interaction lengths for each of the calorimeters.

**THE LAR ELECTROMAGNETIC CALORIMETER** uses liquid argon as its active detector medium alternating with layers of lead acting as the absorber. The layers are shaped like accordions, which allows for complete coverage with multiple layers of active material, three in central  $\eta$  ( $0 < |\eta| < 2.5$ ) and two at higher  $\eta$  ( $2.5 < |\eta| < 3.2$ ). At  $|\eta| < 1.8$ , an instrumented liquid argon presampler provides a measurement of energy lost prior to reaching the calorimeters. The total energy resolution for this detector is about 10%.

**THE TILE CALORIMETER** is a hadronic calorimeter which surrounds the LAr Calorimeter. It uses layers of steel as its absorber with scintillating tiles as the active material between them, which are read out by photomultiplier tubes. The Tile Calorimeter covers  $|\eta| < 1.7$  with a typical energy resolution of about 50%.

**THE LAR HADRONIC ENDCAP CALORIMETER** covers the hadronic calorimetry for higher  $\eta$ . It uses liquid argon active material and copper plate absorbers, resulting in an energy resolution of approximately 50%. This calorimeter covers  $1.5 < |\eta| < 3.2$ , overlapping with the hadronic calorimeters in either direction of its  $\eta$  range.

**THE FCAL** or forward calorimeter provides electromagnetic and hadronic coverage at very high  $\eta$  ( $3.1 < |\eta| < 4.9$ ). This calorimeter also uses liquid argon as its active material, and uses copper-tungsten as the absorber. Its energy resolution is about 100%.

#### 4.4 THE MUON SPECTROMETER

The Muon Spectrometer ([MS](#)) measures charged particles that penetrate the calorimeter system. Because the calorimeters are designed to completely absorb electrons, photons, and hadrons, the [MS](#) mainly detects muons, which pass through the calorimeter with very little loss of energy. The goal of the [MS](#) is to give a high-precision measurement of these muons, and also to be able to quickly identify events with muons for the sake of triggering, discussed in [Section 4.6](#). The layout of the [MS](#) can be seen in Figures [22](#) and [23](#). Muons can be measured for all  $|\eta| < 2.7$ , and they can be triggered on for  $|\eta| < 2.4$ . The entire system is about 24 m tall and 40 m long.

To achieve these goals, the [MS](#) has several subsystems. The system responsible for precision measurement is called the [MDTs](#). This sub-detector consists of chambers of three to eight layers of tubes, with three layers of chambers covering both the barrel and end-cap regions. In the barrel, these chambers are arranged in layers concentric cylinders with small overlaps between adjacent chambers. The chambers are oriented such that the drift tubes are parallel to the beam line. In

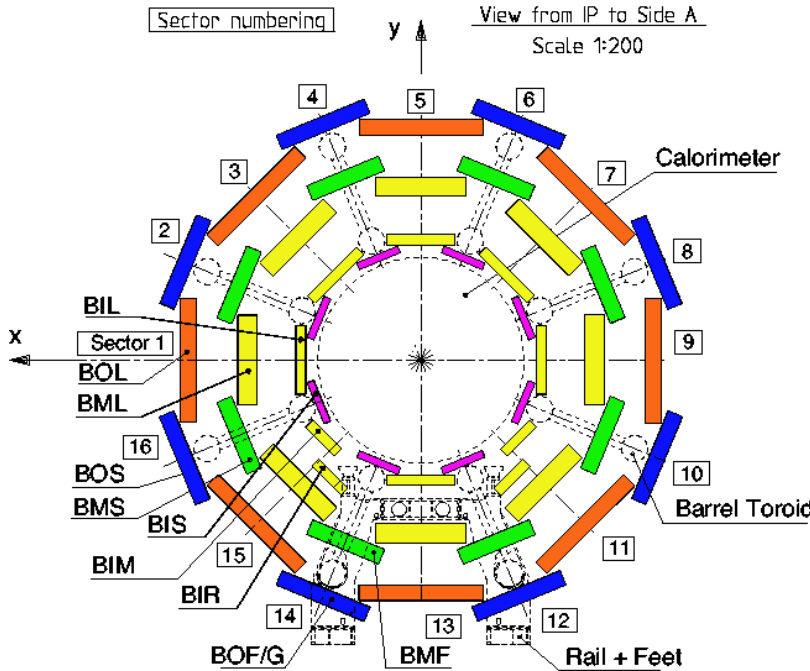


Figure 22: An  $x$ - $y$  view of the MS. In it, the three barrel layers are visible, as well as the overlapping, differently sized chambers. The outer layer of the MS is about 20m in diameter.

the endcap, the chambers form disks with drift tubes approximately aligned in the  $R$  direction.

The tubes each contain an Ar/CO<sub>2</sub> gas mixture and a single high voltage wire which runs at its center along its length. Charged particles excite the gas as they pass through it, producing electrons which drift towards the high voltage wire. The resulting electric signal is read out, and the magnitude and timing of the signals are both used to differentiate particle traces from noise.

Though very effective at giving a precise measurement, the MDTs have two shortcomings. The first is that the measurement is only precise in the direction perpendicular to the tubes; in the direction parallel to them, the resolution is not much better than the length of the drift tube, which are typically several meters long. The resolution in the perpendicular direction is about 35  $\mu\text{m}$  with the combined measurement of all the tubes in a chamber. The second major shortcoming is that the MDTs are slow, with a maximum drift time of about 700 ns.

The slow drift time means that muons from sequential collisions can appear in the same event, and that the signals from the MDTs are received too late to be used for triggering. To solve the former problem, another detector called the Cathode-Strip Chambers (CSCs) is used in high-rate regions of the MS. This detector consists of multi-wire proportional chambers which have cathode strips on either side of the anode in orthogonal directions, providing a 40  $\mu\text{m}$  resolution in one direction and 5mm resolution in the other. Their drift times

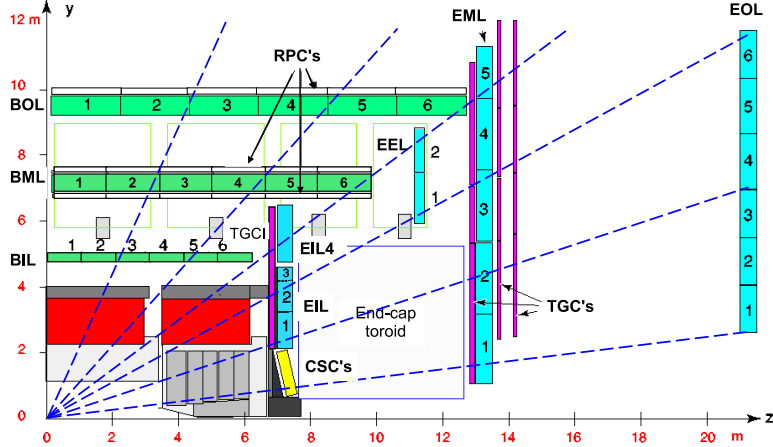


Figure 23: An  $r$ - $z$  view of the [MS](#). The three layers of the barrel and endcap [MS](#) are visible, and all muons at  $|\eta|<2.7$  should traverse three detectors, assuming they propagate in an approximately straight line from the interaction point.

are also much shorter than those of the [MDTs](#), at about 40 ns. They are placed in the forward region of the detector ( $2<|\eta|<2.7$ ) where the incident particle rates are highest.

To achieve responses fast enough to be used for triggering, Resistive Plate Chambers ([RPCs](#)) and Thin Gap Chambers ([TGCs](#)) are used. These chambers both take less than 25 ns to produce a signal. The [RPCs](#) are used in the barrel and are made up of two high-resistance plastic plates with a gas mixture under an electric field between them. Passing particles ionize this gas, and the resulting signal is read out via metallic strips mounted to the plastic plates. The [TGCs](#) used in the endcap are a form of multi-wire proportional chambers, like the [CSCs](#). Unlike the [CSCs](#), the cathode is placed extremely close to the wires, speeding up its operation.

The massive [MS](#) is subject to deformations due to gravity and the magnetic field. To achieve a high precision alignment, these deformations are constantly monitored in each [MDT](#) chamber with a set of four optical alignment rays, which give alignment information at the precision of  $<30\ \mu\text{m}$ . In addition, a sag-adjustment system can use this information to re-align any wires that droop under gravity's pull. Lastly, the [MS](#) can be aligned using the tracks made from hits it measures, discussed more in [Section 5.3](#).

#### 4.5 THE MAGNET SYSTEM

The ATLAS magnet system consists of four superconducting magnets: an inner solenoid, a barrel toroid, and two endcap toroids. Collec-

tively, they are 22m in diameter and 26m long, and their basic layout can be seen in Figure 24.

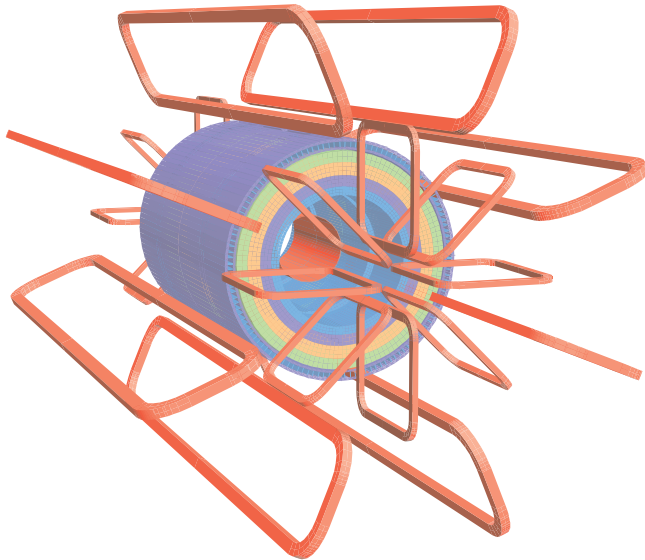


Figure 24: The magnet system of the ATLAS detector. The inner cylinder shows the solenoid which gives a uniform magnetic field in the **ID**. Outside of that are the barrel and endcap toroids, which provide a non-uniform magnetic field for the **MS**.

The solenoid is inside the calorimeter volume and provides a uniform 2T magnetic field for particles traveling through the **ID**. This axial field causes the trajectories of charged particles to bend in the  $x - y$  plane, and measurements of the curvature of these trajectories give the most accurate  $p_T$  measurement for many particles according to the equation

$$p_T = qB\rho \quad (22)$$

where  $q$  is the charge of the particle,  $B$  is the magnetic field in the  $z$  direction, and  $\rho$  is the radius of curvature.

Because the solenoid is placed between the tracking system and the calorimeter, it is important that it interfere minimally with particles in order to allow the calorimeter to measure their full energies. The solenoid is placed inside the same vacuum chamber as the LAr calorimeter and is made of Al-stabilized NbTi superconductor with aluminum casing, giving it a total thickness of about 0.66 radiation lengths.

The barrel toroid is outside the calorimeters and provides the magnetic field for the barrel **MS**, which varies from 0.2–2.5T. The endcap toroids have a magnetic field range of 0.2–3.5T. All three toroid magnets are made with Al-stabilized Nb/Ti/Cu superconducting coils supported by Al-alloy struts.

The magnets are cooled with liquid helium, and take up to a month to be brought down to operating temperatures. All magnets have cold masses surrounding them to absorb heat in the event of a quench.

The  $B$ -field resulting from this magnet system can be seen in Figure 25. The plot on top demonstrates the relatively constant field rate within the barrel which drops steeply at  $|z|=2$ . The bottom plot shows the field integral in the MDTs as a function of  $|\eta|$ , demonstrating the good coverage out to  $|\eta|<2.6$  excluding a transition region between the barrel and endcap, where the field can drop to around half its usual value.

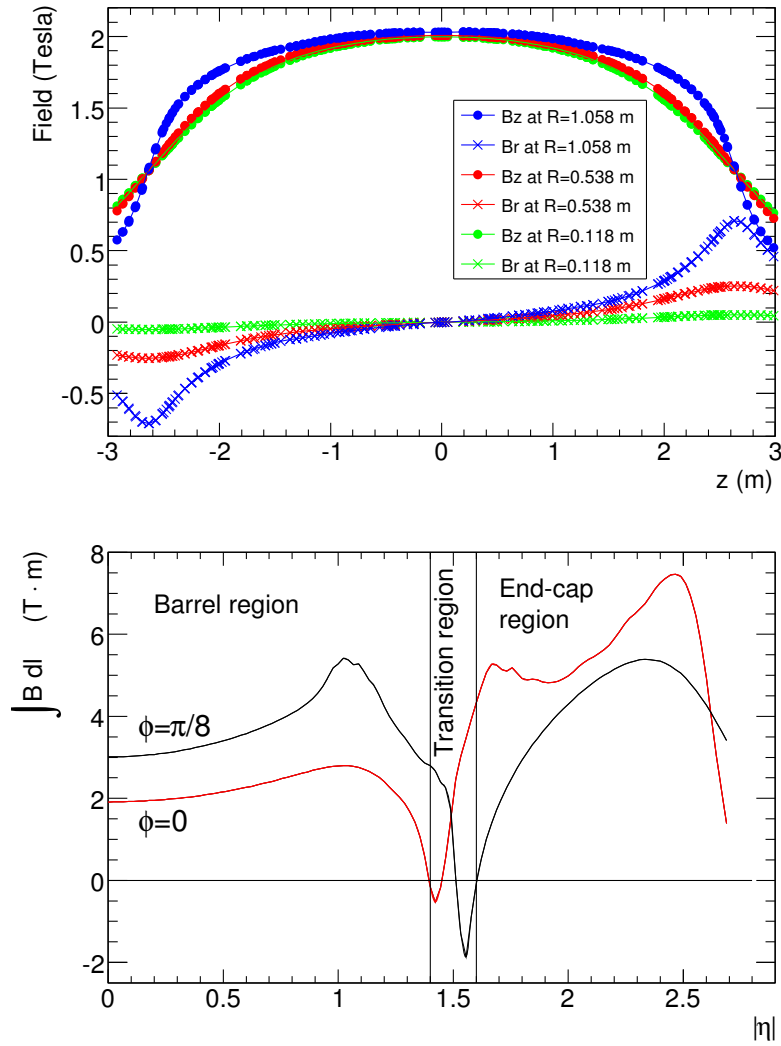


Figure 25: Plots of the magnetic field within the ATLAS detector. Top is the field (broken into its  $R$  and  $z$  components) as a function of  $z$  for several different values of  $R$ . Bottom is the field integral through the MDTs as a function of  $|\eta|$  for two different  $\phi$  values.

## 4.6 THE TRIGGER SYSTEM AND DATA ACQUISITION

The LHC provides proton bunch crossings every 25 ns, and each of these events contains about one MB of data, corresponding to 40 TB/s, a completely unmanageable amount of data. In addition to this concern, many of ATLAS’s subdetectors like the pixel detector and MDTs take much longer than 25 ns to read out, making keeping up with the bunch crossing rate impossible. To reduce the total data read out and allow for selective reading out of the slower detectors, a triggering system is used.

The trigger system uses fast detectors to get a coarse picture of an event’s topology, which is then compared to a trigger menu, which lists the types of events that are interesting enough to keep. Overall, the trigger system reduces the 40 million collisions a second to about 1000 to be fully read out from the ATLAS detector.

This filtering of events is done in two steps: the L<sub>1</sub> trigger is implemented in hardware and reduces the initial 40MHz to 100kHz, while the HLT is implemented in software, further reducing the rate to 1kHz [14]. The L<sub>1</sub> trigger uses coarse granularity information from the fast read-out subdetectors: the calorimeters, the RPCs and TGCs.

The coarse grained calorimeter information used for the L<sub>1</sub> trigger decision is referred to as L<sub>1</sub> Calorimeter Trigger (L<sub>1</sub>Calo) and uses information from all calorimeter systems. L<sub>1</sub>Calo is responsible for all triggers excluding muons, meaning it must be capable of identifying a large number of different objects and event topologies, including high- $p_T$  objects,  $E_T^{\text{miss}}$ , and large amounts of hadronic energy. The trigger can also identify isolated objects, objects with very few calorimeter deposits from other objects near them.

Events types that occur very frequently, such that it would require too much of the total trigger bandwidth to record all events passing a given threshold, are prescaled. Events passing these triggers are only recorded a fraction of the time, and these prescaling rates are used to adjust the final data to account for the limited rate. For example, the lowest unprescaled single electron trigger in 2016 data-taking required an electron with 60 GeV $p_T$ . A trigger requiring electrons with only 10 GeV $p_T$  also exists, but is prescaled by approximately a factor of ten.

An example of the L<sub>1</sub> trigger rates for different types of events can be seen in Figure 26 for one run in July 2016. The common features to all rates are due to LHC luminosity changes, deadtimes due to detector inefficiency, and adjustment of prescales to optimize trigger bandwidth.

For muon triggers, the trigger algorithm looks for patterns of hits from the RPC and TGC that are consistent with high- $p_T$  muons with origins at the interaction point.

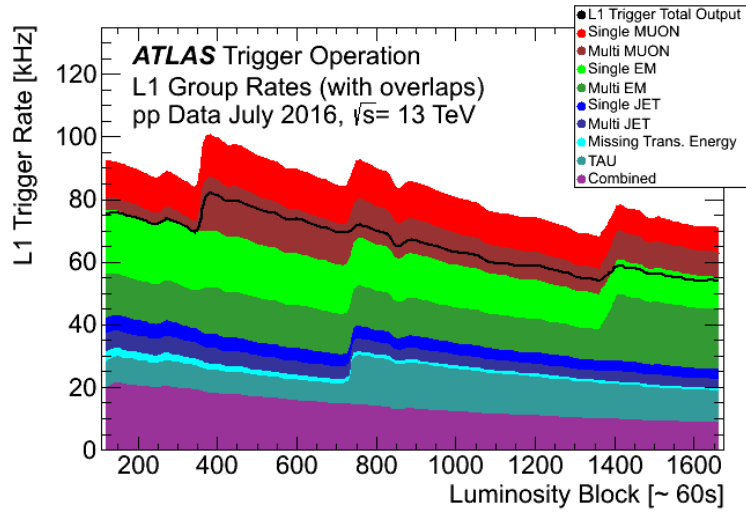


Figure 26:  $L_1$  trigger rates for a run in July 2016 as a function of luminosity block, an approximately 60-second long period of data-taking. The total rate is lower than the combined stack because of overlapping triggers.

All of this information is analyzed by the Central Trigger Processor (**CTP**), which uses a trigger menu identifying all types of events to be kept to return a trigger decision. The event must be processed in about  $2.5\mu\text{s}$  so that the remaining event information not yet read out is still available on the subdetectors when the trigger decision is made. This decision is passed to the Trigger Timing and Control (**TTC**), which communicates with all subdetectors. Upon receiving a  $L_1$  trigger, the subdetectors read out all the information they've stored about the event and place it on their Read Out Boards (**ROBs**).

The **HLT** takes the data from particular Region of Interests (**RoIs**), areas containing interesting objects that caused the  $L_1$  trigger, and analyzes this much more complete picture of the region to decide whether or not the event is still interesting enough to keep. This process has its own trigger menu with dedicated  $L_1$  seeds for each item. **HLT** triggers typically have slightly higher thresholds than their corresponding  $L_1$  triggers to ensure that events that would pass the **HLT** requirements are very likely to have passed the  $L_1$  requirements. Figure 27 shows the **HLT** rates for the same run in July. In addition to the event types seen in Figure 26, the **HLT** can also identify events with  $b$ -jets, differentiate between electrons and photons, and identify events interesting for B-physics.

Events passing the **HLT** trigger are written to disk to be analyzed. An example of the total trigger efficiency for single electron triggers is shown in Figure 28. Trigger efficiencies can be taken directly from **MC**, and are measured in data via a method called tag-and-probe, the main principles of which are discussed in Section 10.3.

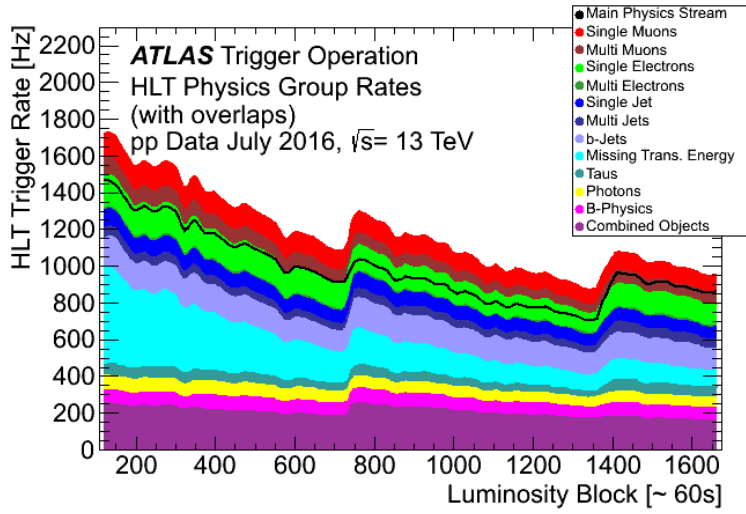


Figure 27: HLT trigger rates for a run in July 2016 as a function of luminosity block, an approximately 60-second long period of data-taking. The total rate is lower than the combined stack because of overlapping triggers.

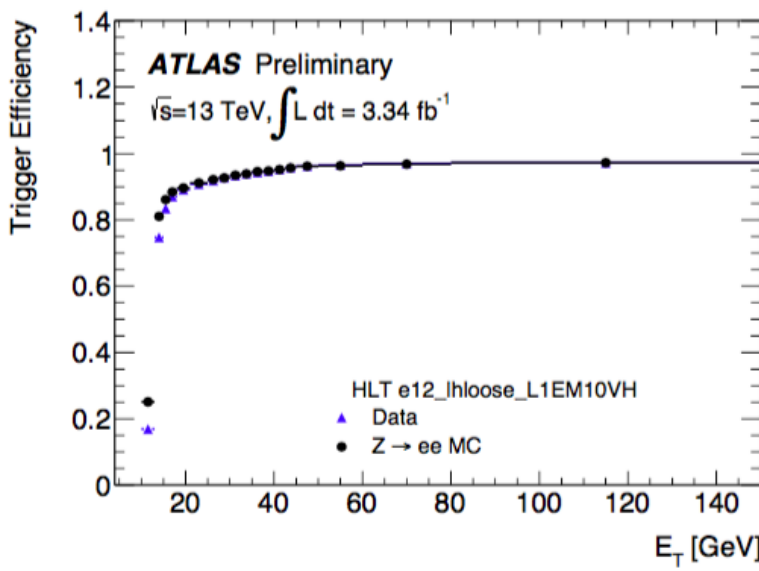


Figure 28: Trigger efficiencies as a function of  $E_T$  for data and MC. Efficiencies are given for offline selected loose electrons.



# 5

## OBJECT RECONSTRUCTION IN THE ATLAS DETECTOR

---

5.1 ELECTRONS

5.2 PHOTONS

5.3 MUONS

5.4 JETS

5.5 MISSING TRANSVERSE ENERGY

Another common usage is  $E_T^{miss}$ , which gives the negative vectorial sum of the energy in an event.

5.6 MONTE CARLO SIMULATION



## APPLICATION OF A NEURAL NETWORK TO PIXEL CLUSTERING

### 6.1 CLUSTERING IN THE PIXEL DETECTOR

Creating tracks from individual hits in the Inner Detector is one of most computationally challenging parts of the reconstruction of ATLAS events. Each event typically contains thousands of hits in the pixel detector alone, which must be combined into one coherent picture of which particles traversed the detector, and how they moved and lost energy as they traveled. A typical particle deposits charge in several pixels per layer, forming a series of clusters which can be connected together to form a track. This track can in turn be used to measure the charge, momentum, and trajectory of the particle.

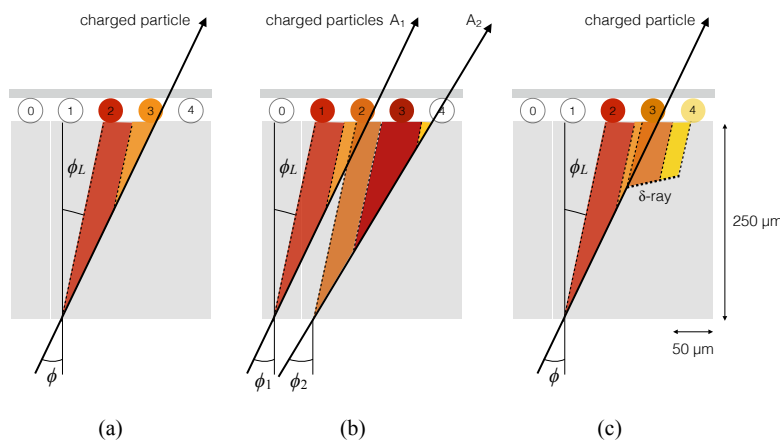


Figure 29: A few possible types of clusters in the Pixel Detector. (a) shows a single particle passing through a layer of the detector, (b) shows two particles passing through the detector, creating a single merged cluster, and (c) shows a single particle emitting a  $\delta$ -ray as it passes through the detector.

The process of going from clusters to track is relatively simple in an isolated environment in which one particle travels cleanly through all the layers, but can be complicated by multiple close-by tracks and by a single particle's emission of low energy particles, called  $\delta$ -rays. In these cases, it can be hard to tell how many particles were involved in creating a cluster, and where exactly each of those particles passed through the layer. A few examples of particle interactions with the pixel sensor can be seen in Figure 29 . The process of determining which pixels with charge deposits belong to a single particle is called

clustering, and it has recently been updated from a charge interpolation method to a method using a [NN](#).

### 6.1.1 Charge Interpolation Method

A typical cluster contains a few pixel hits spanning in the  $x$  and  $y$  directions, each with its own measurement of charge deposition, or [ToT](#). The extent of the cluster is defined by grouping together any pixels with a shared edge or corner. In the charge interpolation method, also called the [CCA](#) clustering algorithm, these individual hits are combined to make one estimation of the position a single particle which passed through them, using the following equation:

$$x_{cluster} = x_{center} + \Delta_x(\phi, N_{row}) \cdot \left[ \Omega_x - \frac{1}{2} \right] \quad (23)$$

$$x_{cluster} = x_{center} + \Delta_x(\phi, N_{row}) \cdot \left[ \Omega_x - \frac{1}{2} \right] \quad (24)$$

where  $\Omega_{x(y)}$  is defined by

$$\Omega_{x(y)} = \frac{q_{last\ row(col)}}{q_{first\ row(col)} + q_{last\ row(col)}} \quad (25)$$

and  $q$  represents the [ToT](#) of a given pixel, and  $\Delta_{x(y)}$  is a function derived from either data or [MC](#) and produces an output related to the projected length of the particles track on the pixel sensor and is measured as a function of  $\phi$ , the incident angle of a particle on the sensor, and  $N_{row(col)}$ , the number of pixels in the  $x$  and  $y$  direction.

In a simple case, such as (a) of [Figure 29](#), this method works quite effectively. However, in cases like (b), it has no ability distinguish two-particle from one-particle clusters, and can only assign a cluster center between the two particles' locations, despite that intermediate pixel having the lowest [ToT](#). Furthermore, because this method can't differentiate two-particle clusters, the tracking software can't use that information to preferentially allow multiple tracks to be fit to the cluster. In cases like (c), the  $\delta$ -ray will bias the measurement of the particle's position in whichever direction it is emitted.

### 6.1.2 Improving Measurement with Neural Networks

To address these problems, a series of [NNs](#) were created [7]. The first estimates the number of particles in a given cluster, the second predicts their positions within the cluster, and the third assesses the uncertainty of the position measurement. They are referred to, respectively, as the "Number", "Position", and "Error" [NNs](#).

These [NNs](#) are all trained with:

- a  $7 \times 7$  grid of cluster **ToT** information<sup>1</sup>
- a 7-element vector containing the  $y$ -size of the pixels in the grid<sup>2</sup>
- the layer of the pixel detector that the cluster was observed in
- a variable indicating whether the cluster is located in the barrel or endcap
- $\theta$  and  $\phi$  variables projecting the incident angles of the particle on the sensor, assuming it comes from the nominal interaction point
- the pixel module's  $\eta$  index, a label assigned to each module that is roughly proportional to its  $\eta$  position

After the Number **NN** predicts a number of particles associated with the cluster, required to be between 1 and 3, the same inputs are fed to one of three Position **NNs** based on the determined number of particles, which then outputs the  $x$  and  $y$  positions of each of the particles. Then, the same inputs combined with the output of the Position **NN** are fed into one of three Error **NNs** (also distinguished by number of particles), which outputs an uncertainty for each of the position predictions made. An example of the output of this process can be seen in [Figure 30](#), where the improved position resolution from the ability to identify a multi-particle cluster is evident.

The particle location predictions from the **NNs** are then handed to the tracking software, which now can use these multiple particle position predictions as independent hits to be fit. As a result, tracks in dense environments have fewer clusters shared between multiple tracks, and their trajectories are known to a greater degree of precision.

## 6.2 IMPACT OF THE NEURAL NETWORK

The **NN** was first applied to 7 TeV data, where it improved position resolution for particles in small and large clusters. [Figure 31](#) shows the improvement from the addition of the **NN** in  $x$  resolution in different cluster sizes. The improvement from **CCA** clustering is particularly evident in the 4-pixel case, where the double peaked structure of the interpolation method has been completely removed with the **NN**.

---

<sup>1</sup> Clusters spanning more than seven pixels in either direction are split into multiple clusters.

<sup>2</sup> The pixel detector contains some long pixels at the edges of modules, and this is intended to help the **NN** identify these cases.

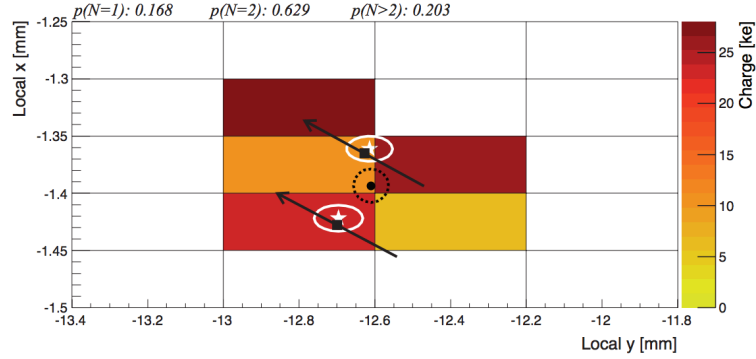


Figure 30: One example of a two-particle cluster and its truth information compared with the output of the NNs. The boxes represent pixels, with a color scale indicating ToT. At top, the  $p(N = i)$  values give the output of the Number NN, the probabilities that the cluster contains 1, 2, and 3 particles. Given the highest probability is for  $N = 2$ , the other NNs predict the position and errors of the two particles (in white). The black arrows and squares represent the truth information from the cluster, and the black dot and dotted line show the position measurement for the un-split cluster.

### 6.2.1 The Neural Network in 13 TeV Data

In Run 2, the tracking algorithm is first run on the CCA clusters, where it constructs loose tracks that allow shared clusters, clusters to which multiple tracks are fit [10]. The NN is then used to identify which clusters are likely to have had multiple particles pass through them, and to identify the positions of those particles. In the case that the cluster is determined to have resulted only from one particle, tracks that share that cluster are penalized by decreasing its “track score”, a measure of the quality of the track.

With this configuration, studies were done to determine how accurately MC could model the NN’s response to data. Figure 32 shows a comparison of how often the NN identifies different types of clusters in data and MC. Very good agreement was seen between the two samples.

With this confirmation that studies performed in MC would be good indicators for performance on data, the robustness of the NN was investigated with 13 TeVMC [11]. The goal of these studies was to determine which variables the NN’s predictions were most sensitive to, and whether it was likely that these variables could be mismodeled enough to produce unexpected results in data. One example of a sensitive variable is the overall charge scale, which is tested by scaling the ToT of all pixels in a cluster up and down. The impact of its scaling can be seen in Figure 33. In this case, the likelihood to misidentify multi-particle clusters and single particle clusters depended significantly on this scaling. Overall, it was found that variations on the

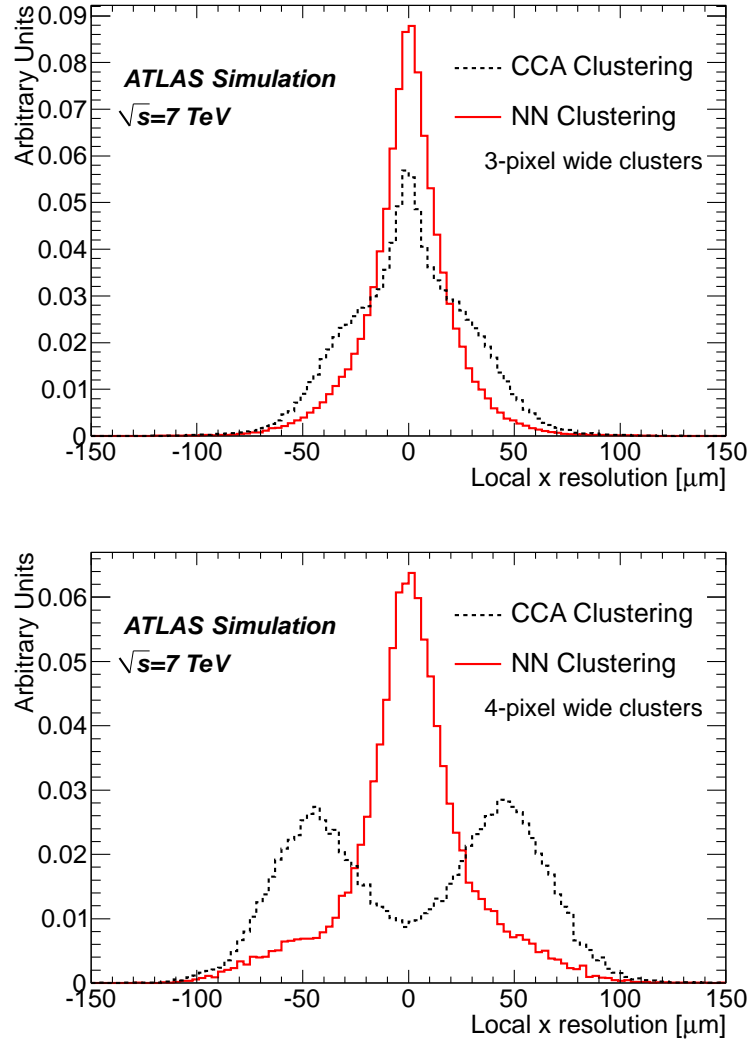


Figure 31:  $x$  resolutions for clusters with 3 (top) and 4 (bottom) pixels in the  $x$  direction in 7 TeV data for CCA and NN clustering taken from MC.

cluster charge produced a significant impact on predictions, while all other variations, such as incidence angle variation and spatial smearing of charge, had a minimal effect.

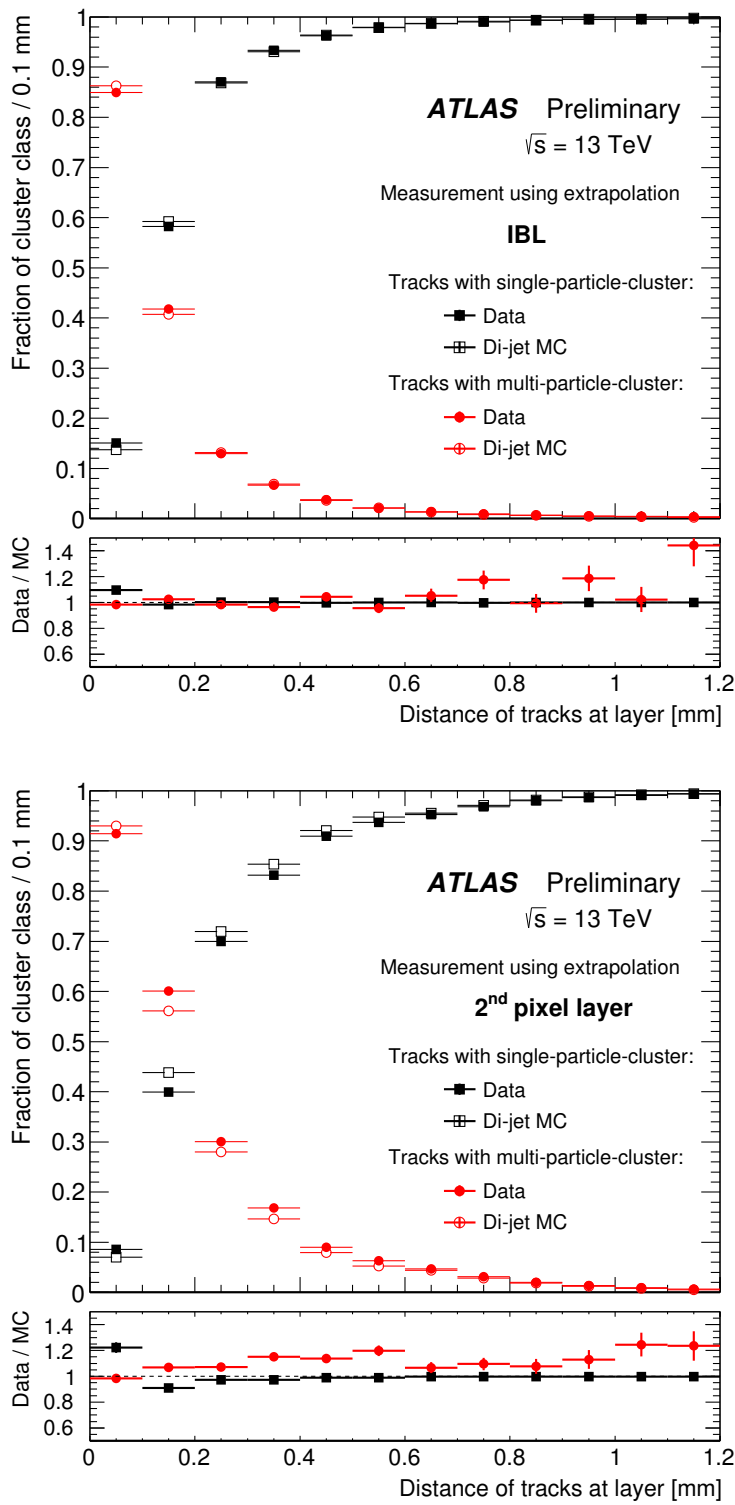


Figure 32: Fraction of cluster classes as a function of the distance between tracks for IBL (top) and 2nd pixel layer (bottom).

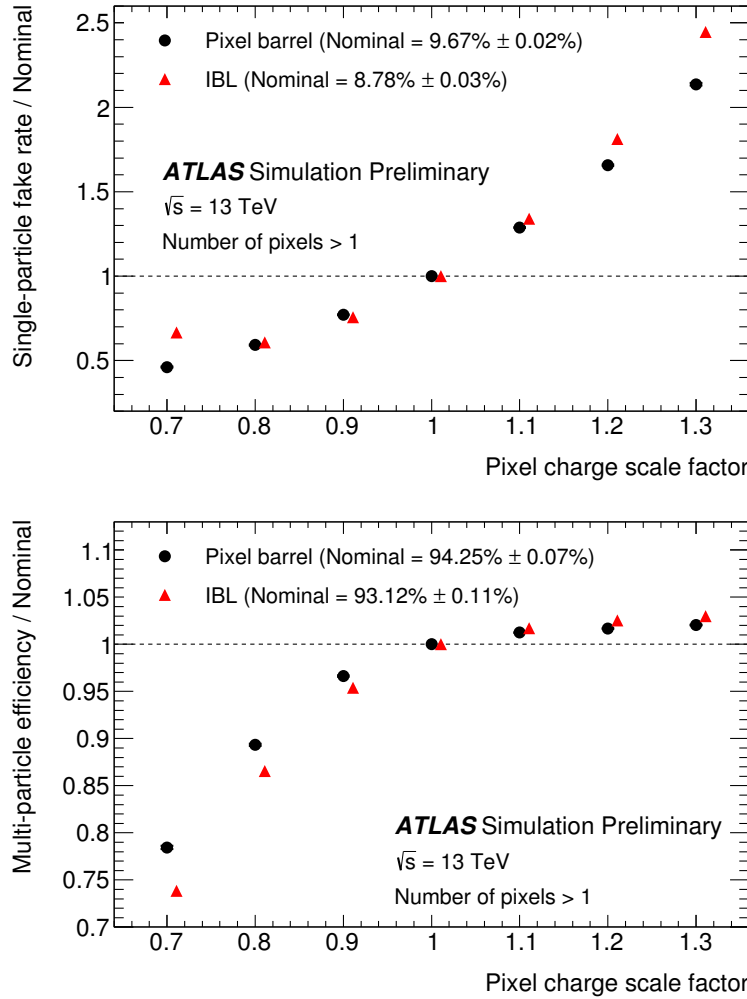


Figure 33: Performance of the pixel neural network used to identify clusters created by multiple charged particles, as a function of constant coherent scaling of the charge in each pixel in the cluster. The top figure shows the rate at which the neural network wrongly identifies clusters with one generated particle as clusters with multiple particles. The bottom figure shows the rate at which the neural network correctly identifies clusters generated by multiple particles as such.



## Part IV

### SEARCHING FOR SUPERSYMMETRY

This section describes an analysis of the ATLAS data carried out by the author and her analysis team. The analysis was performed on events from  $p - p$  collisions provided by the LHC at  $\sqrt{s}=13$  TeV. It searches for events like those described in [Section 2.2.3.1](#), which contain a Z boson decaying to leptons, jets, and missing transverse energy. The selection of a signal region in which to search for these events, background estimates, systematic uncertainty estimates, results, and interpretations are all discussed.



## BACKGROUND PROCESSES

This analysis is fundamentally a search for Supersymmetry ([SUSY](#)) in events with two leptons whose invariant mass is consistent with a Z boson. Additional event selections are made to reduce Standard Model ([SM](#)) processes relative to potential [SUSY](#) processes, defined by simplified models discussed in [Section 2.2.3.1](#). [SUSY](#) events typically have large amounts of  $E_T^{\text{miss}}$ ,  $H_T$  (the scalar sum of the  $p_T$  of objects in the event), and many jets. All of these features can help isolate these events from backgrounds. To understand what cuts would optimize the sensitivity of the search, it is essential to first understand what these [SM](#) backgrounds are.

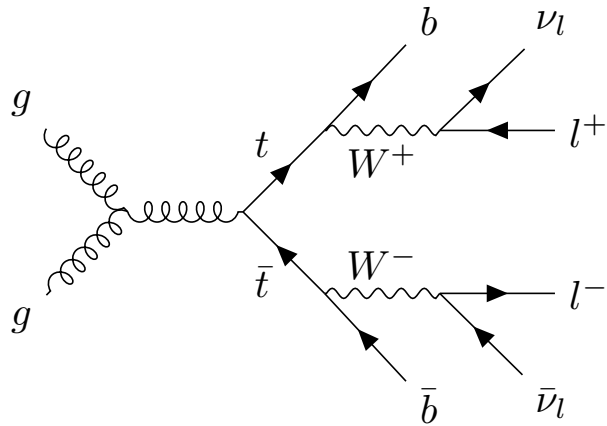


Figure 34: An example Feynman diagram of  $t\bar{t}$  production and decay.

**TOP-ANTITOP ( $t\bar{t}$ )** production is the largest background for this search. [Figure 34](#) shows an example of this process, which results in many jets, leptons, and neutrinos, which are seen in the detector as  $E_T^{\text{miss}}$ . Thus,  $t\bar{t}$  events naturally have high  $E_T^{\text{miss}}$  and  $H_T$ , jets, and leptons from two different W boson decays, which may coincidentally form an invariant mass consistent with a Z boson. These events are very difficult to separate from potential signals, though keeping the mass window small and increasing  $E_T^{\text{miss}}$  and  $H_T$  above the typical values for  $t\bar{t}$  events helps reduce this background.

**DIBOSON ( $VV$ )** production is the next leading background. These events can contain real Z bosons and will peak on-Z like a signal. In addition, in events like [Figure 35](#), an additional W boson can decay to another lepton and a neutrino, providing  $E_T^{\text{miss}}$ . The pictured process can occur with associated jets, but at reduced rates, so adding a jet

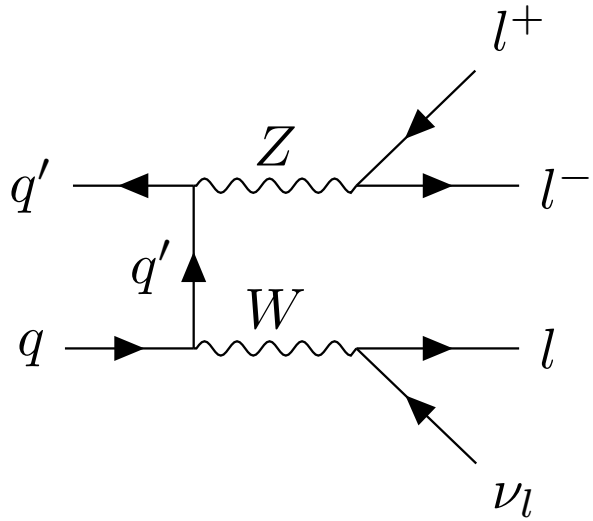


Figure 35: An example Feynman diagram of the production and decay of a WZ event.

requirement to the signal region helps reduce these events. If the  $W$  boson in this diagram instead decayed to two jets, there would be no true  $E_T^{\text{miss}}$  from a neutrino, so a  $E_T^{\text{miss}}$  cut in conjunction with a jet cut is very effective in reducing the total diboson background. A veto on a third lepton could also be used to reduce this background, but, depending on the signal model considered, this veto can also decrease signal acceptance, so it is not used in this analysis.

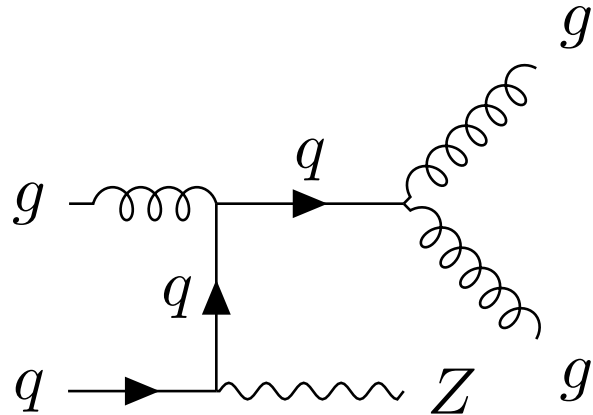


Figure 36: An example Feynman diagram of the production and decay of a  $Z/\gamma^*$  + jets event.

$Z/\gamma^*$  + JETS processes are very common but, as shown in Figure 36, don't produce any true  $E_T^{\text{miss}}$  or a very large number of jets. A high  $H_T$  cut helps reduce this background, but this process often occurs with associated jets, producing many events with large amounts

of hadronic activity.  $E_T^{\text{miss}}$  is the most powerful variable to reduce this background, because though events with mismeasured jets or leptons can fake  $E_T^{\text{miss}}$ , but these mismeasurements drastic enough to produce hundreds of GeV of  $E_T^{\text{miss}}$  are rare.

Other processes can contribute to the Standard Model background at lower rates. Processes similar to  $Z/\gamma^* + \text{jets}$  but with a W boson instead of a Z have real  $E_T^{\text{miss}}$  from leptonic W decays, but only one lepton. However, a fake or non-prompt lepton can cause these events to look very similar to simulated signals. Additionally, there are rare processes such as  $t\bar{t}$  production in association with bosons that will also be difficult to separate from signal processes.

### 7.1 MONTE CARLO SAMPLES

To precisely compare simulated signal to backgrounds, MC samples are generated for each of these processes. Table 1 details the method used to produce each sample. With these and the simulated background, optimizations on a signal region can be made to maximize potential for discovery or exclusion of simplified Supersymmetric models. These comparisons and the signal region definition can be found in Section 9.1.

Physics process	Generator	Parton Shower	Cross section	Tune	PDF set
$t\bar{t} + W$ and $t\bar{t} + Z$ [16, 39]	MG5_AMC@NLO MG5_AMC@NLO	Pythia 8.186 Pythia 8.186	NLO [28, 47] LO [20]	A14 A14	NNPDF23LO NNPDF23LO
$t\bar{t}$ + WW [16]	Powheg Box v2 r3926	Pythia 6.428	NNLO+NNLL [35, 36]	PERUGIA2012 PERUGIA2012	NILOCT10 NILOCT10
$t\bar{t}$ [49]	Powheg Box v2 r2856	Pythia 6.428	Approx. NNLO [42]	PERUGIA2012	NILOCT10
Single-top ( $Wt$ ) [49]	SHERPA 2.1.1	SHERPA 2.1.1	NNLO [27, 29]	SHERPA default	NILOCT10
WW, WZ and ZZ [48]	SHERPA 2.1.1	SHERPA 2.1.1	NNLO [30, 31]	SHERPA default	NILOCT10
$Z/\gamma^*$ ( $\rightarrow \ell\ell$ ) + jets [47]	SHERPA 2.1.1	SHERPA 2.1.1	NNLO [30, 31]	SHERPA default	NILOCT10

Table 1: Simulated background event samples used in this analysis with the corresponding matrix element and parton shower generators, cross-section order in  $\alpha_s$  used to normalise the event yield, underlying-event tune and PDF set.

# 8

## OBJECT IDENTIFICATION AND SELECTION

---

### 8.1 ELECTRONS

Cut	Value/description
Baseline Electron	
Acceptance	$p_T > 10 \text{ GeV},  \eta^{\text{clust}}  < 2.47$
Quality	LHLoose
Signal Electron	
Acceptance	$p_T > 25 \text{ GeV},  \eta^{\text{clust}}  < 2.47$
Quality	LHMedium
Isolation	GradientLoose
Impact parameter	$ z_0 \sin \theta  < 0.5 \text{ mm}$ $ d_0 / \sigma_{d_0}  < 5$

Table 2: Summary of the electron selection criteria. The signal selection requirements are applied on top of the baseline selection.

### 8.2 MUONS

### 8.3 JETS

### 8.4 PHOTONS

Cut	Value/description
Baseline Muon	
Acceptance	$p_T > 10 \text{ GeV},  \eta  < 2.5$
Quality	Medium
Signal Muon	
Acceptance	$p_T > 25 \text{ GeV},  \eta  < 2.5$
Quality	Medium
Isolation	GradientLoose
Impact parameter	$ z_0 \sin \theta  < 0.5 \text{ mm}$ $ d_0 / \sigma_{d_0}  < 3$
isBadMuon	MCP isBadMuon Flag

Table 3: Summary of the muon selection criteria. The signal selection requirements are applied on top of the baseline selection.

## EVENT SELECTION

---

Table 4: Overview of all signal, control and validation regions used in the on-shell Z search. More details are given in the text. The flavour combination of the dilepton pair is denoted as either “SF” for same-flavour or “DF” for different flavour. All regions require at least two leptons, unless otherwise indicated. In the case of CR $\gamma$ , VR-WZ, VR-ZZ, and VR-3L the number of leptons, rather than a specific flavour configuration, is indicated. The main requirements that distinguish the control and validation regions from the signal region are indicated in bold. Most of the kinematic quantities used to define these regions are discussed in the text. The quantity  $m_T(\ell_3, E_T^{\text{miss}})$  indicates the transverse mass formed by the  $E_T^{\text{miss}}$  and the lepton which is not assigned to either of the Z-decay leptons.

On-shell Z regions	$E_T^{\text{miss}}$ [GeV]	$H_T^{\text{incl}}$ [GeV]	$n_{\text{jets}}$	$m_{\ell\ell}$ [GeV]	SF/DF	$\Delta\phi(\text{jet}_{12}, p_T^{\text{miss}})$	$m_T(\ell_3, E_T^{\text{miss}})$ [GeV]	$n_{\text{b-jets}}$
Signal region								
SRZ	> 225	> 600	$\geq 2$	$81 < m_{\ell\ell} < 101$	SF	> 0.4	—	—
Control regions								
CRZ	< <b>60</b>	> 600	$\geq 2$	$81 < m_{\ell\ell} < 101$	SF	> 0.4	—	—
CR-FS	> 225	> 600	$\geq 2$	<b>61</b> < $m_{\ell\ell}$ < <b>121</b>	DF	> 0.4	—	—
CRT	> 225	> 600	$\geq 2$	$> 40$ , $m_{\ell\ell} \notin [81, 101]$	SF	> 0.4	—	—
CR $\gamma$	—	> 600	$\geq 2$	—	$0\ell, 1\gamma$	—	—	—
Validation regions								
VRZ	< <b>225</b>	> 600	$\geq 2$	$81 < m_{\ell\ell} < 101$	SF	> 0.4	—	—
VRT	<b>100–200</b>	> 600	$\geq 2$	$> 40$ , $m_{\ell\ell} \notin [81, 101]$	SF	> 0.4	—	—
VRS	<b>100–200</b>	> 600	$\geq 2$	$81 < m_{\ell\ell} < 101$	SF	> 0.4	—	—
VR-FS	<b>100–200</b>	> 600	$\geq 2$	<b>61</b> < $m_{\ell\ell}$ < <b>121</b>	DF	> 0.4	—	—
VR-WZ	<b>100–200</b>	—	—	—	$3\ell$	—	< 100	0
VR-ZZ	< 100	—	—	—	$4\ell$	—	—	0
VR-3L	<b>60–100</b>	> <b>200</b>	$\geq 2$	$81 < m_{\ell\ell} < 101$	$3\ell$	> 0.4	—	—

### 9.1 SIGNAL REGION

### 9.2 CONTROL AND VALIDATION REGIONS

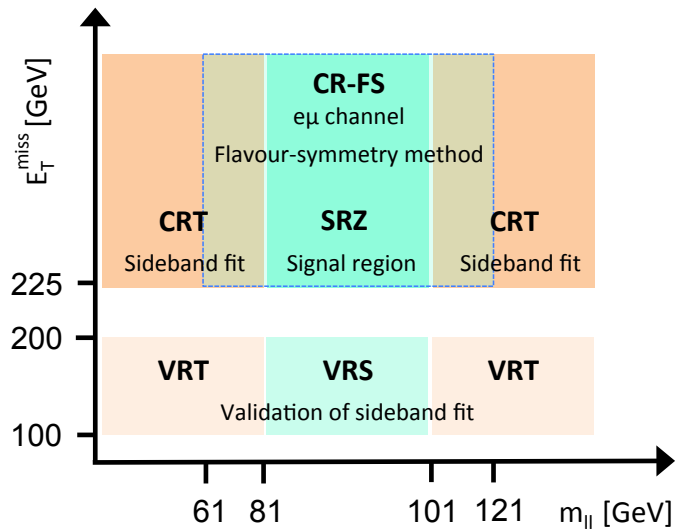


Figure 37: Schematic diagrams of the control, validation and signal regions for the on-shell  $Z$  (top) and edge (bottom) searches. For the on-shell  $Z$  search the various regions are shown in the  $m_{\ell\ell} - E_T^{\text{miss}}$  plane, whereas in the case of the edge search the signal and validation regions are depicted in the  $H_T - E_T^{\text{miss}}$  plane.

Trigger	L1	Notes
<b>Single electron triggers</b>		
HLT_e60_lhmedium	L1_EM22VHI	2015 and 2016
HLT_e60_lhmedium_nod0	L1_EM22VHI	2016 Only
HLT_e26_lhtight_nod0_ivarloose	L1_EM22VHI	Isolated; for evaluation in 2016
<b>Di-electron triggers</b>		
HLT_2e12_lhloose	L1_2EM13VH	2015 Only
HLT_2e17_lhvloose_nod0	L1_EM15VH	2016 Only
<b>Single muon triggers</b>		
HLT_mu50	L1_MU20	2015 and 2016
<b>Di-muon triggers</b>		
HLT_mu18_mu8noL1	L1_MU15	2015 Only
HLT_2mu14_nomucomb	L1_MU10	2016 Only
<b>Electron-muon triggers</b>		
HLT_e17_lhloose_mu14	L1_EM15VH_MU10	2015 Only
HLT_e7_lhmedium_mu24	L1_MU20	2015 Only
HLT_e17_lhloose_nod0_mu14	L1_MU10_EM15VH	2016 Only
HLT_e7_lhmedium_nod0_mu24	L1_MU20	2016 Only

Table 5: List of the triggers considered for this analysis. The corresponding L1 items are included for reference. The last column notes if the trigger is available in data.

Lepton $p_T$	Trigger in 2015	Trigger in 2016
<b>Di-electron channel</b>		
$p_T(e_1) > 65 \text{ GeV}$	HLT_e60_lhmedium	HLT_e60_lhmedium_nod0
$p_T(e_1) \leq 65 \text{ GeV}$	HLT_2e17_lhloose	HLT_2e17_lhvloose_nod0
<b>Di-muon channel</b>		
$p_T(\mu_1) > 52.5 \text{ GeV}$	HLT_mu50	HLT_mu50
$p_T(\mu_1) \leq 52.5 \text{ GeV}$	HLT_mu24_mu8noL1	HLT_2mu14_nomucomb
<b>Electron-muon channel</b>		
$p_T(e) > 65 \text{ GeV}$	HLT_e60_lhmedium	HLT_e60_lhmedium_nod0
$p_T(e) \leq 65 \text{ GeV} \text{ and } p_T(\mu) > 52.5 \text{ GeV}$	HLT_mu50	HLT_mu50
$p_T(e) \leq 65 \text{ GeV} \text{ and } p_T(\mu) \leq 52.5 \text{ GeV} \text{ and } p_T(e) < p_T(\mu)$	HLT_e7_lhmedium_mu24	HLT_e7_lhmedium_nod0_mu24
$p_T(e) \leq 65 \text{ GeV} \text{ and } p_T(\mu) \leq 52.5 \text{ GeV} \text{ and } p_T(\mu) < p_T(e)$	HLT_e17_lhloose_mu14	HLT_e17_lhloose_nod0_mu14

Table 6: Lepton trigger requirements used for the analysis in different regions of lepton- $p_T$  phase space.



## BACKGROUND ESTIMATION

---

This analysis requires two leptons that reconstruct to a  $Z$  mass, jets,  $E_T^{\text{miss}}$ , and  $H_T$ . Any standard model processes that produce this signature will appear as a background to the search. The most important task of the analysis is to identify and estimate these backgrounds, so that any excess of events appearing on top of the standard model background can be identified. The main backgrounds for this analysis are described in [Chapter 7](#). The largest background is from flavor symmetric processes, with smaller contributions coming from diboson processes,  $Z/\gamma^* + \text{jets}$ , rare top processes, and fake and non-prompt leptons.

### 10.1 FLAVOR SYMMETRIC PROCESSES

[FS](#) backgrounds include any processes that produce pairs of leptons with uncorrelated flavor in the final state. In this analysis, the largest contribution comes from  $t\bar{t}$ , with additional events from processes like  $WW$  and  $Z \rightarrow \tau\tau$ . In these processes, each lepton comes from a different decay. Unlike a  $Z \rightarrow \ll$  decay then, these leptons' flavors are completely independent.

#### 10.1.1 Flavor Symmetry Method

As a consequence of the independence of the lepton flavors, any [FS](#) process should produce  $ee$ ,  $\mu\mu$ , and  $e\mu$  events in a 1:1:2 ratio. This ratio is taken advantage of by the flavor symmetry method by measuring  $e\mu$  events in data and using them to predict the contribution of these processes in the  $ee$  and  $\mu\mu$  channels. [13]

To estimate the number of events in SRZ, a control region called CR-FS is used. Both regions are defined in [Table 4](#). CR-FS is very similar to SRZ with two changes: it requires different-flavor leptons instead of the same-flavor leptons required by SRZ, and the  $m_{\ell\ell}$  range it covers has been expanded by a factor of three, now ranging from 61 to 121 GeV. The expansion of the  $m_{\ell\ell}$  window is done to increase the number of events in the control region, thus lowering the statistical uncertainty of the prediction<sup>1</sup>.

---

<sup>1</sup> Though this statistical uncertainty is no longer dominant for the analysis, the method was developed for a smaller dataset for which this expansion dramatically decreased the total uncertainty on the background prediction. [5] Because of previous excesses seen, the signal region was not reoptimized for the larger dataset used in this search,

This control region is expected to be about 95% pure in **FS** processes, with most of the remaining events coming from fake or non-prompt leptons. The **FS** portion is made up primarily of  $t\bar{t}$  ( $\sim 80\%$ ), with additional contributions from  $Wt$  ( $\sim 10\%$ ),  $WW$  ( $\sim 10\%$ ), and  $< 1\% Z \rightarrow \tau\tau$ .

After the number of data events are measured in CR-FS, correction factors are applied to account for trigger efficiencies, selection efficiencies, the  $m_{\ell\ell}$  expansion, and the purity of the control region. Combining these factors, the estimate for number of events in the  $ee$  and  $\mu\mu$  channels is as follows:

$$N_{ee}^{\text{est}} = \frac{1}{2} \cdot f_{\text{FS}} \cdot f_{Z\text{-mass}} \cdot \sum_{\ell=1}^{N_{e\mu}^{\text{data}}} k_e(p_T^\ell, \eta^\ell) \cdot \alpha(p_T^{\ell_1}, \eta^{\ell_1}), \quad (26)$$

$$N_{\mu\mu}^{\text{est}} = \frac{1}{2} \cdot f_{\text{FS}} \cdot f_{Z\text{-mass}} \cdot \sum_{\ell=1}^{N_{e\mu}^{\text{data}}} k_\mu(p_T^\ell, \eta^\ell) \cdot \alpha(p_T^{\ell_1}, \eta^{\ell_1}), \quad (27)$$

where  $N_{e\mu}^{\text{data}}$  is the number of data events observed in CR-FS,  $f_{\text{FS}}$  is the **FS** purity in CR-FS,  $f_{Z\text{-mass}}$  is the fraction of events in the widened  $m_{\ell\ell}$  range expected to be in the on-Z range (taken from  $t\bar{t}$  **MC**),  $k_e(p_T, \eta)$  and  $k_\mu(p_T, \eta)$  are relative selection efficiencies for electrons and muons, calculated in bins of  $p_T$  and  $\eta$  of the lepton to be replaced, and  $\alpha(p_T, \eta)$  accounts for the different trigger efficiencies for events in each channel, binned based on the kinematics of the leading lepton. These  $k$  and  $\alpha$  factors are calculated from data in an inclusive on-Z selection ( $81 < m_{\ell\ell}/\text{GeV} < 101$ ,  $\geq 2$  jets), according to:

$$k_e(p_T, \eta) = \sqrt{\frac{N_{ee}^{\text{meas}}}{N_{\mu\mu}^{\text{meas}}}} \quad (28)$$

$$k_\mu(p_T, \eta) = \sqrt{\frac{N_{\mu\mu}^{\text{meas}}}{N_{ee}^{\text{meas}}}} \quad (29)$$

$$\alpha(p_T, \eta) = \frac{\sqrt{\epsilon_{ee}^{\text{trig}}(p_T, \eta) \times \epsilon_{\mu\mu}^{\text{trig}}(p_T, \eta)}}{\epsilon_{e\mu}^{\text{trig}}(p_T, \eta)} \quad (30)$$

where  $\epsilon_{ee/\mu\mu}^{\text{trig}}$  is the trigger efficiency <sup>2</sup> and  $N_{ee/\mu\mu}^{\text{meas}}$  is the number of  $ee/\mu\mu$  events in the inclusive on-Z region described above. Here  $k_e(p_T, \eta)$

---

but in future iterations of this analysis, the signal region have tighter cuts, making this decreased statistical uncertainty significant once again.

<sup>2</sup> This efficiency is defined by taking all events in the inclusive on-Z selection mentioned above and determining the fraction that passes the relevant trigger requirement defined by [Table 6](#). Because the offline selection made on these events already has some trigger dependence, this calculation of efficiency could be slightly biased. This effect is considered in [Section 11.1.1](#), and the uncertainty applied to the estimate as a result is described.

Region	$ee$ prediction	$\mu\mu$ prediction	combined prediction
Prediction for $14.7 \text{ fb}^{-1}$ of 2015+2016 Data			
SRZ	$16.50 \pm 2.11$	$16.67 \pm 2.04$	$33.16 \pm 3.94$
VRS	$49.70 \pm 4.61$	$49.60 \pm 4.56$	$99.31 \pm 8.47$

Table 7: Yields in signal and validation regions for the flavor symmetric background. Errors include statistical uncertainty, uncertainty from MC closure, uncertainty from the  $k$  and  $\alpha$  factors, uncertainty due to deriving triggers efficiencies from a DAOD, and uncertainty on the MC shape used to correct for the  $m_{\ell\ell}$  expansion.

$= 1/k_{\mu}(p_T, \eta)$ , and this  $k$  factor is calculated separately for leading and sub-leading leptons, and the appropriate  $k$  value is selected based on the position of the lepton to be replaced.

Electron, muon, and trigger efficiencies are all quite close to one, and as a consequence, these correction factors are typically within 10% of unity, except in the region  $|\eta| < 0.1$  where, because of the lack of coverage of the muon spectrometer, they are up to 50% from unity.

The estimate is corrected for contamination of non-**FS** backgrounds in CR-FS. A scaling factor is determined by subtracting these backgrounds from the number of  $e\mu$  events measured in CR-FS, then determining the fraction of the original data events that this pure-**FS** number represents. The estimate for the other backgrounds is taken from **MC** for all processes except fakes, which are predicted from data using the matrix method described in [Section 10.3](#).

A prediction is made both for the signal region, SRZ, and the lower- $E_T^{\text{miss}}$  validation region, VRS. This process is performed separately for the two data taking periods, 2015 and 2016, because of the changing triggers and conditions. The results are then summed together, as shown in [Table 7](#). The uncertainties in this table are discussed in [Section 11.1.1](#).

### 10.1.2 Sideband Fit Method

As a crosscheck to the flavor symmetry method, a **MC**-based method is used. This method is called a “sideband fit,” and it begins with a **MC** estimate of the signal region across a  $m_{\ell\ell}$  range that includes all values above 40 GeV. This region, excluding the on-Z range that makes up the Signal Region (**SR**), is used as a control region, defined as CRT in [Table 4](#).

The total data yield is measured in CRT, and the **MC** is fit to match this yield with one normalization factor which scales the overall  $t\bar{t}$  background. As mentioned in the previous section,  $t\bar{t}$  is the dominant **FS** background, making up about 80% of the total events. All other

backgrounds contributing to this control region are constrained by their uncertainties, which are used as nuisance parameters in the fit. The normalization factor from this fit is then applied to the  $t\bar{t}$  MC yield in the SR, and combined with the MC predictions of the other FS processes in the SR to give a final estimate of this background. The results of the fit can be seen in Table 8.

The method is repeated in VRS to validate the method. The normalization factors, listed in Table 9, are significantly different for the two regions. This is expected because there is a known problem in which the  $t\bar{t}$  MC over-predicts the high- $E_T^{\text{miss}}$  tail. This effect can be seen in a data-MC comparison in Figure 38. This is likely due to a mismodeling of the top quark  $p_T$  distribution, which does not match the spectrum seen in data [15, 26]. However, this method corrects for this mismodeling by performing fits in regions very kinematically similar to the signal region.

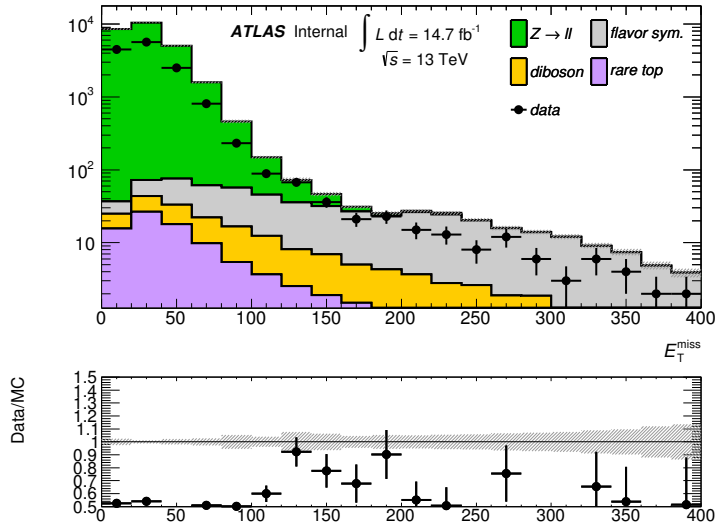


Figure 38: Comparison of data and MC in a selection like SRZ, without the  $E_T^{\text{miss}}$  cut.

This method is extremely effective as a crosscheck because it uses a completely independent dataset from the flavor symmetry method, and the two methods have very little overlap in dependence on MC. They produce consistent results in both SRZ and VRS, as shown in Table 10.

## 10.2 $Z/\gamma^* + \text{jets}$ BACKGROUND

The  $Z/\gamma^* + \text{jets}$  background is mainly produced by a process called Drell-Yan in which annihilating quark/anti-quark pairs produce a  $Z$  boson or a virtual photon. These bosons then decay to two leptons, which, in the case of the  $Z$  boson, naturally appear in the  $Z$ -mass window. The boson typically recoils off a hadronic system, which

channel	$ee/\mu\mu$ CRT	$ee/\mu\mu$ SRZ	$ee/\mu\mu$ SRZ	$ee/\mu\mu$ SRZ
Observed events	273	60	35	25
Fitted bkg events	$272.76 \pm 16.88$	$49.33 \pm 8.04$	$27.09 \pm 4.73$	$22.70 \pm 3.80$
Fitted flavour symmetry events	$236.96 \pm 21.66$	$28.96 \pm 7.47$	$16.41 \pm 4.33$	$12.55 \pm 3.29$
Fitted $WZ/ZZ$ events	$4.03 \pm 1.13$	$14.27 \pm 4.45$	$7.81 \pm 2.45$	$6.46 \pm 2.07$
Fitted SHERPA $Z/\gamma^*$ + jets events	$1.95 \pm 0.14$	$0.00 \pm 0.00$	$0.00 \pm 0.00$	$0.00 \pm 0.00$
Data-driven $Z/\gamma^*$ + jets ( $\gamma$ + jets) events	$0.00 \pm 0.00$	$3.10 \pm 2.25$	$1.02^{+1.25}_{-1.02}$	$2.08 \pm 1.38$
Fitted rare top events	$4.04 \pm 1.04$	$2.90 \pm 0.76$	$1.39 \pm 0.38$	$1.50 \pm 0.40$
Data-driven fake lepton events	$25.78 \pm 14.26$	$0.10^{+0.18}_{-0.10}$	$0.46 \pm 0.45$	$0.10 \pm 0.01$
MC exp. SM events	366.71	61.01	33.73	27.74
MC exp. flavour symmetry events	331.32	40.72	23.09	17.63
MC exp. $WZ/ZZ$ events	4.02	14.20	7.77	6.43
MC exp. SHERPA $Z/\gamma^*$ + jets events	1.94	0.00	0.00	0.00
Data-driven exp. $Z/\gamma^*$ + jets ( $\gamma$ + jets) events	0.00	3.10	1.02	2.08
MC exp. rare top events	4.04	2.89	1.39	1.50
Data-driven exp. fake lepton events	25.39	0.10	0.46	0.10

Table 8: Background fit results from the sideband fit method. The  $t\bar{t}$  MC's normalization is taken as a free parameter in the fit to data in CRT, then that normalization factor is applied in SRZ. The results are shown here both divided between the  $ee$  and  $\mu\mu$  channels and summed together. All other backgrounds are taken from MC in CRT, while in SRZ, the  $Z/\gamma^*$  + jets contribution is taken from the  $\gamma$  + jets method. The uncertainties quoted include both statistical and systematic components.

Fit region	$t\bar{t}$ normalization
CRT	$0.64 \pm 0.18$
VRT	$0.80 \pm 0.09$

Table 9: Summary of the  $t\bar{t}$  normalization factors calculated by the sideband fit to CRT and VRT for the 2015+2016 data.

Region	Flavour-symmetry	Sideband fit
SRZ	$33 \pm 4$	$29 \pm 7$
VR-S	$99 \pm 8$	$92 \pm 25$

Table 10: Comparison of [FS](#) background predictions from the nominal method, the flavor symmetry method, and the cross-check, the sideband fit method. Uncertainties include statistical and systematic uncertainties in both cases.

can produce the jet and  $H_T$  requirement required in SRZ. However, this process rarely produces real  $E_T^{\text{miss}}$  (though occasionally neutrinos do appear in its hadronic decays), so events often appear with high  $E_T^{\text{miss}}$  values due to extreme mismeasurement. Because SRZ cuts on the very high  $E_T^{\text{miss}}$  tails of a  $Z$  distribution, a small change in the assumptions about jet resolution or energy scale in [MC](#) can drastically change the prediction, and a low  $Z/\gamma^* + \text{jets}$  prediction can result in a signal-like peak appearing in the final result.

Because of this inaccuracy in the [MC](#) prediction in these high  $E_T^{\text{miss}}$  tails, a data-driven method is used to estimate this background. The method takes  $\gamma + \text{jets}$  events which, like the  $Z/\gamma^* + \text{jets}$  events, contain one boson recoiling against a hadronic system, and corrects for the kinematic differences between  $\gamma$  and  $Z$ s [4, 25]. These sample of photons used in taken from CR- $\gamma$ , which is similar to the SRZ selection without the  $E_T^{\text{miss}}$  requirement, but it vetoes leptons and requires at least one photon. Additionally, the  $\Delta\phi(\text{jet}_{12}, p_T^{\text{miss}})$  cut, which is designed to reduce the background from mismeasured jets, is removed for this region because of its unpredictability at very low values of  $E_T^{\text{miss}}$ , when the angle of the  $E_T^{\text{miss}}$  is much less meaningful.

The most significant experimental difference between  $Z$  and photon events is that  $Z$  bosons rapidly decay, in the case of this analysis, to two leptons, which can then be observed by the ATLAS detector. In contrast, the photon is stable, and can be directly detected by ATLAS. This means that the reconstructed  $Z$  boson and the directly observed photon have very different energy resolutions.

### 10.3 FAKES

The fakes background consists of processes that produce only one lepton, but whose events are otherwise kinematically similar to the [SR](#). These processes include semileptonic  $t\bar{t}$ ,  $W$ +jets processes, and single top. Though these processes typically only produce one lepton, they can be reconstructed with two leptons due to a hadron being misidentified as a lepton or from real non-prompt lepton resulting from photon conversions or  $b$ -hadron decays. As such, it includes both events that have been properly reconstructed and many that are included in the [SR](#) due to imperfect reconstruction. As with the  $Z/\gamma^* + \text{jets}$  background, it is very difficult to predict with [MC](#) because the flaws in reconstruction are typically less well described by the models used in [MC](#) production than the successes. Nonetheless, a rough estimate can be made of this background by using [MC](#), which indicates that the number of fake events in SRZ is consistent with zero.

Despite the small predicted contribution in the [SR](#), a data-driven method called the “matrix method” is employed to estimate these fake events [12]. This method is also used to estimate the fakes contribution to other control and validation regions where their effect is often more significant.

In the matrix method, the quality requirements for signal leptons are loosened to give a selection of baseline leptons (see [Table 2](#) and [Table 3](#)), which consist of a higher fraction of fake leptons. In each CR, VR, or SR, the remaining kinematic selections are made on the baseline leptons, and the number of leptons in that region which pass the signal lepton requirements ( $N_{\text{pass}}$ ) and the number which fail ( $N_{\text{fail}}$ ) are measured. For a 1-lepton selection, these quantities can be used to predict the number of fake events that pass the selection according to:

$$N_{\text{pass}}^{\text{fake}} = \frac{N_{\text{fail}} - (1/\epsilon^{\text{real}} - 1) \times N_{\text{pass}}}{1/\epsilon^{\text{fake}} - 1/\epsilon^{\text{real}}}. \quad (31)$$

The efficiencies  $\epsilon^{\text{real}}$  and  $\epsilon^{\text{fake}}$  give the relative identification efficiency from baseline to signal for genuine, prompt leptons and fake and non-prompt leptons, respectively. For a 2-lepton selection, the principle is the same, but the equation is more complicated, and it requires four-by-four matrix to account for possible combinations of real and fake leptons.

To calculate  $\epsilon^{\text{real}}$ , the tag-and-probe method is performed a selection of  $Z \rightarrow \ell\ell$  data events, CR-real, described in [Table 11](#). In this method, one “tag” lepton passing a signal selection is required, as is another “probe” lepton passing a baseline requirement. Distributions of  $m_{\ell\ell}$  for tag + passing probe and tag + failing probe are then fit, and

the efficiency is computed using the ratio acquired from the fit. A comparison of data and MC in CR-real can be seen in Figure 39.

Fakes regions	$E_T^{\text{miss}}$ [GeV]	$H_T$ [GeV]	$n_{\text{jets}}$	$m_{\ell\ell}$ [GeV]	SF/DF	OS/SS	$n_{\ell}$
CR-real	–	$> 200$	$\geq 2$	<b>81–101</b>	$2\ell$ SF	OS	2
CR-fake	$< 125$	–	–	$> 12$	$2\ell$ SF/DF	SS	$\geq 2$

Table 11: Control regions used to measure efficiencies of real and fake leptons. The flavour combination of the dilepton pair is denoted as either “SF” for same-flavour or “DF” for different flavour. The charge combination of the leading lepton pairs are given as “SS” for same-sign or “OS” for opposite-sign.

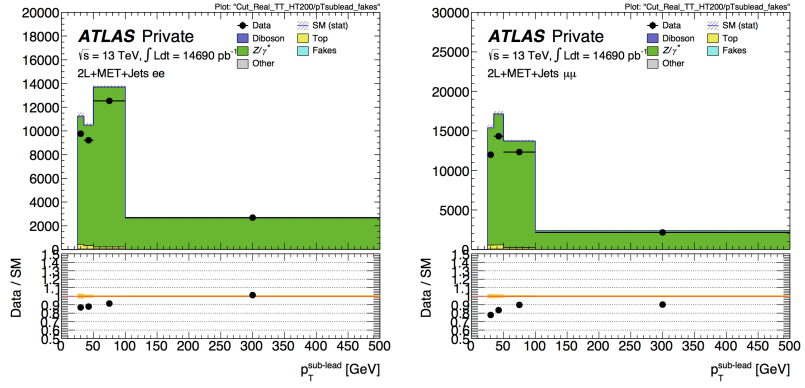


Figure 39: Sub-leading lepton  $p_T$  for  $ee$  (left) and  $\mu\mu$  (right) events in the tight-tight region used to measure the real-lepton efficiency for 2016.

The fake efficiency,  $\epsilon^{fake}$ , is determined using the tag-and-probe method in CR-fake, also described in Table 11. This region is different from all other regions considered in this analysis because it requires same-sign leptons. Very few processes genuinely produce two same-sign leptons, so this region is enhanced in fake leptons. An upper limit on  $E_T^{\text{miss}}$  is placed on CR-fake to limit the possible contamination from BSM processes. According to MC, real, prompt leptons make up about 7% (11%) of the baseline electron (muon) sample and about 10% (61%) of the signal electron (muon) sample. These backgrounds are subtracted from the CR-fake yields when calculating the efficiencies. Figure 40 shows a comparison of data and MC in this region.

This method is validated in a fakes-rich validation region with a same-sign lepton requirement,  $E_T^{\text{miss}} \geq 50\text{GeV}$ ,  $\geq 2$  jets, and a veto on  $m_{\ell\ell}$  on the Z-mass peak for same flavor channels. The results of this validation can be seen in Figure 41. With the systematic uncertainties

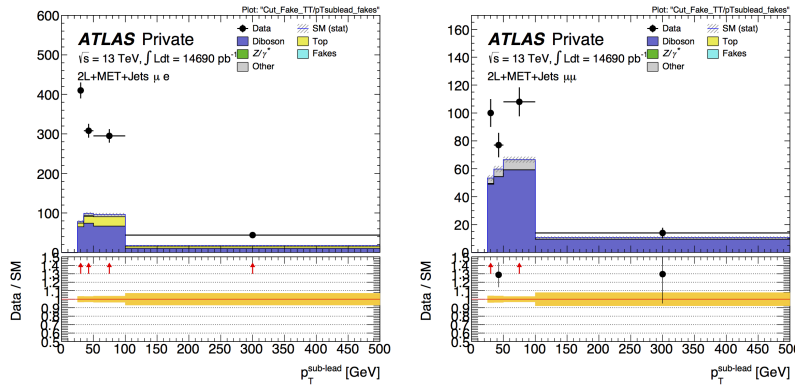


Figure 40: Sub-leading lepton  $p_T$  for  $\mu e$  (left) and  $\mu\mu$  (right) events in the tight-tight region used to measure the fake-lepton efficiency for 2016.

included, the prediction agrees well with the data across a wide range of  $m_{\ell\ell}$  values.

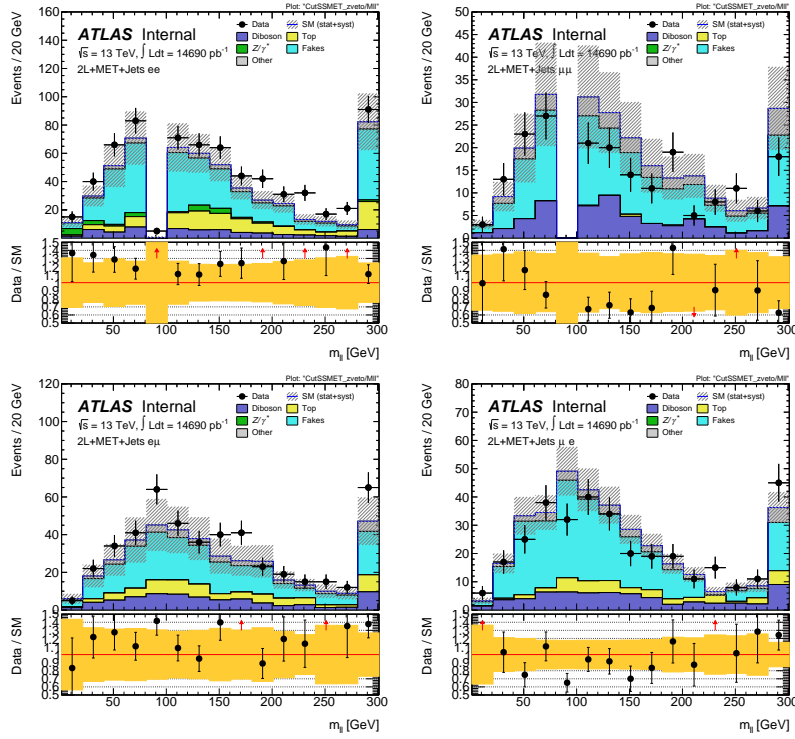


Figure 41: Same sign validation regions in the  $ee$  (top left),  $\mu\mu$  (top right),  $e\mu$  (bottom left) and  $\mu e$  (bottom right) channels combining 2015+2016 data. Uncertainty bands include both statistical and systematic uncertainties.

#### 10.4 DIBOSON AND RARE TOP PROCESSES

The remaining backgrounds are diboson processes (excluding WW, which is included in the [FS](#) background) and rare top processes. Dibosons events make up about 30% of the events in SRZ, while rare top process contributions are much smaller. Both are taken directly from [MC](#), with validation regions to confirm the accuracy of the prediction. These regions are [Table 4](#), and target different parts of these backgrounds. VR-ZZ is a four-lepton selection designed to select a very pure sample of ZZ events. VR-WZ requires three leptons and specific cuts on  $m_T$ , the transverse mass, and  $E_T^{\text{miss}}$  in order to select mostly  $WZ \rightarrow llvv$  events. VR-3L is similar to VR-S, but loosens the  $H_T$  and  $E_T^{\text{miss}}$  cuts and requires at least three leptons. This region is designed to target any  $\geq 3$ -lepton process in a region as kinematically close to SRZ as possible while still maintaining enough events to validate. The makeups of these multilepton validation regions, as well as VRS, are shown in [Table 12](#).

	VR-S	VR-WZ	VR-ZZ	VR-3L
Observed events	236	698	132	32
Total expected background	$224 \pm 41$	$613 \pm 66$	$139 \pm 25$	$35 \pm 10$
Flavour-symmetric	$99 \pm 8$	-	-	-
WZ/ZZ events	$27 \pm 13$	$573 \pm 66$	$139 \pm 25$	$25 \pm 10$
Rare top events	$11 \pm 3$	$14 \pm 3$	$0.44 \pm 0.11$	$9.1 \pm 2.3$
$Z/\gamma^* + \text{jets}$ events	$84 \pm 37$	-	-	-
Fake lepton events	$4 \pm 4$	$26 \pm 6$	-	$0.6 \pm 0.3$

Table 12: Yields in validation regions. In VRS, data-driven background estimates are used for  $Z/\gamma^* + \text{jets}$ , fakes, and [FS](#) processes. All other backgrounds are taken from [MC](#), including all backgrounds in the multi-lepton [VRS](#). Uncertainties include statistical and systematic components.

To confirm that the kinematics are well modeled in the diboson validation regions, distributions of boson mass and  $p_T$  are shown in [MC](#) and data. [Figure 42](#) shows these distributions for VR-WZ, and [Figure 43](#) shows these distributions for VR-ZZ.

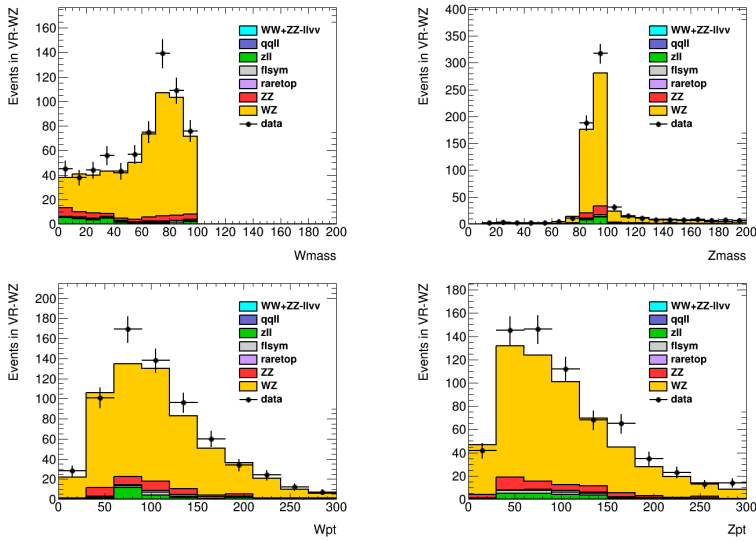


Figure 42: Distributions in VR-WZ. On the top row, reconstructed transverse mass of the  $W$  (left) and mass of the  $Z$  (right). On the bottom row,  $p_T$  of the  $W$  (left) and  $Z$  (right).

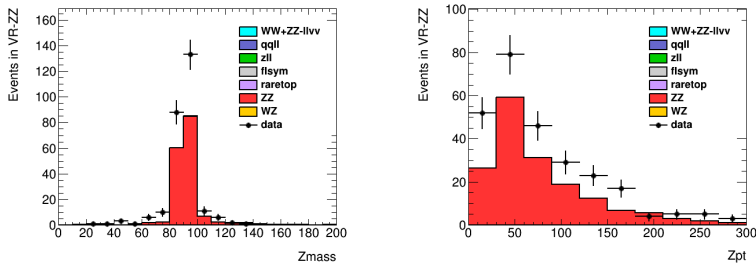


Figure 43: Distributions in VR-ZZ. On the left, mass of the  $Z$  bosons in the event, and on the right,  $p_T$  of the  $Z$  bosons.



## SYSTEMATIC UNCERTAINTIES

---

### 11.1 UNCERTAINTIES ON DATA-DRIVEN BACKGROUNDS

#### 11.1.1 *Uncertainties on the Flavor Symmetry Method*

The flavor symmetry method is a data driven method that makes its primarily on based events populating an **SR**-like Control Region (**CR**) in the different-flavor channel. The statistical uncertainty on these events makes up the dominant uncertainty on the method. To reduce this uncertainty, the  $m_{\ell\ell}$  range on the **CR** is expanded, tripling the number of events in CR-FS. Though this reduces the statistical uncertainty significantly, it is still significantly higher than any of the other systematic uncertainties on this method, as seen in [Table 13](#). Also included in the statistical uncertainty column is the uncertainty on the number of non-**FS** events in CR-FS, which is used to scale the prediction to remove any contamination in the **CR**.

Reg.	Ch.	Pred.	Uncertainties					
			stat. clos.	MC and $\alpha$	k usage	dAOD shape	$m_{\ell\ell}$	total
SRZ	$ee$	16.50	1.82	0.88	0.53	0.12	0.22	2.11
	$\mu\mu$	16.67	1.83	0.79	0.33	0.11	0.23	2.04
	$ee+\mu\mu$	33.16	3.66	1.07	0.86	0.23	0.45	3.94
VRS	$ee$	49.70	3.21	2.34	2.20	0.34	0.75	4.61
	$\mu\mu$	49.60	3.14	2.88	1.40	0.31	0.75	4.56
	$ee+\mu\mu$	99.31	6.34	4.00	3.60	0.65	1.49	8.47

[Table 13](#): Uncertainties in the on-Z signal and validation regions. Nominal predictions are given with statistical uncertainty (including uncertainty from subtracted backgrounds), MC Closure uncertainty, uncertainty on the prediction from varying k and  $\alpha$  by their statistical uncertainties, comparing the efficiencies from AODs to that of DAOs, and on the  $m_{\ell\ell}$ widening, which includes MC statistics and a data/MC comparison in a loosened region.

The next largest contribution to the uncertainty comes from **MC** closure tests, which are used to determine how effective the method is in its prediction. If, for example, using weights derived from an inclusive selection at high  $E_T^{\text{miss}}$  lead to a bias, the closure test would indicate that and an appropriate uncertainty could be placed on the

estimate based on the difference between the MC and the prediction. In this test, the entire FS procedure is performed on  $t\bar{t}$  MC, including a recalculation of weighting factors  $\alpha$  and  $k$ . The prediction from  $e\mu$  events in MC is compared to the MC  $ee$  and  $\mu\mu$  events, as seen in Figure 44. The difference between the two predictions is then summed in quadrature with the statistical uncertainty on each prediction to give the total closure uncertainty seen in Table 13. In these closure tests, all predictions agree within the statistical uncertainty, so the bulk of the resulting error is due to MC statistics.

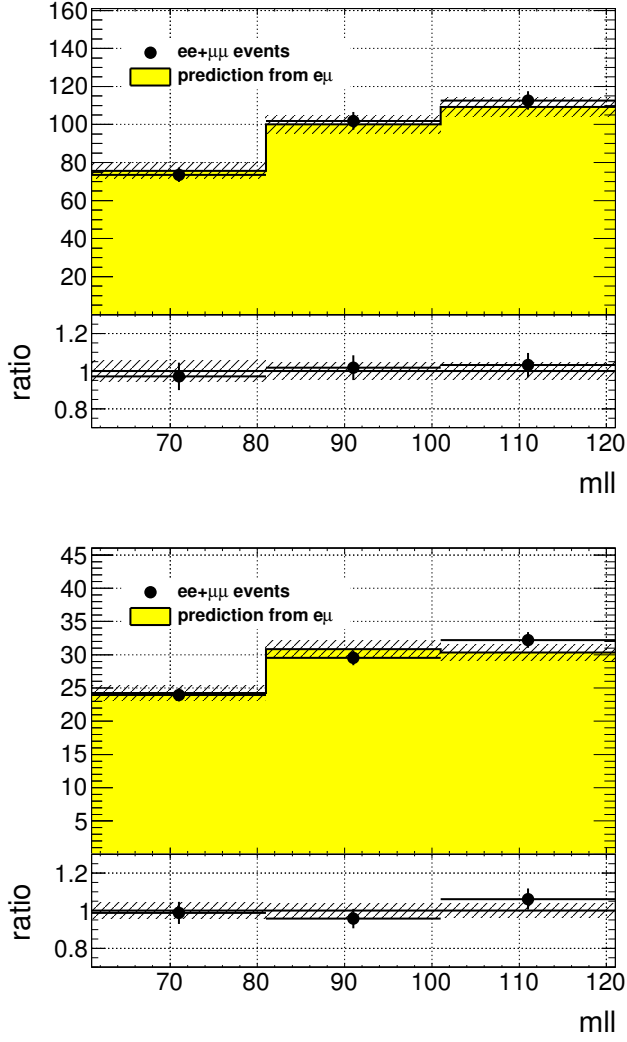


Figure 44: MC closure plots of VRS (top) and SRZ (bottom). The number of events from MC (black points) is compared to the number of events predicted from the flavor symmetry method (yellow histogram). The comparison is performed before the expanded  $m_{\ell\ell}$  window is used to predict the on-Z bin.

A small uncertainty is added based on the statistical uncertainty on the  $k$  and  $\alpha$  factors derived from data. These factors are measured

in many different bins (see, for example, the different measurements of  $k$  in Figure 45), and as a consequence, some bins can have very large statistical uncertainties. To assess the uncertainty on the total estimate, each measurement of these factors is varied by its uncertainty in order to produce the maximum and minimum possible prediction. This error is symmetrized, and the resulting change in the prediction is included in Table 13.

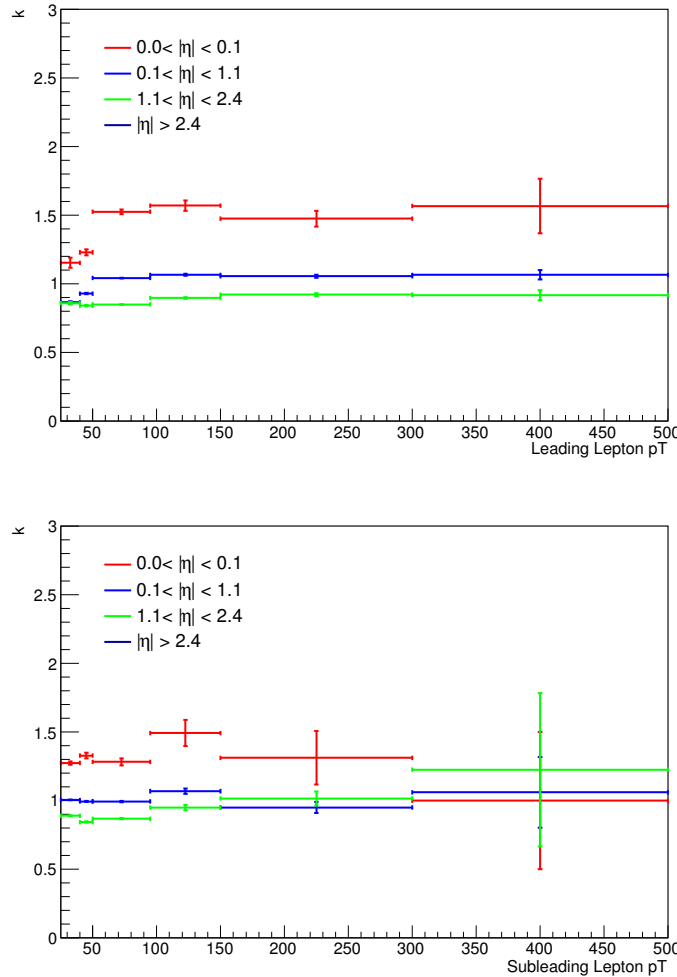
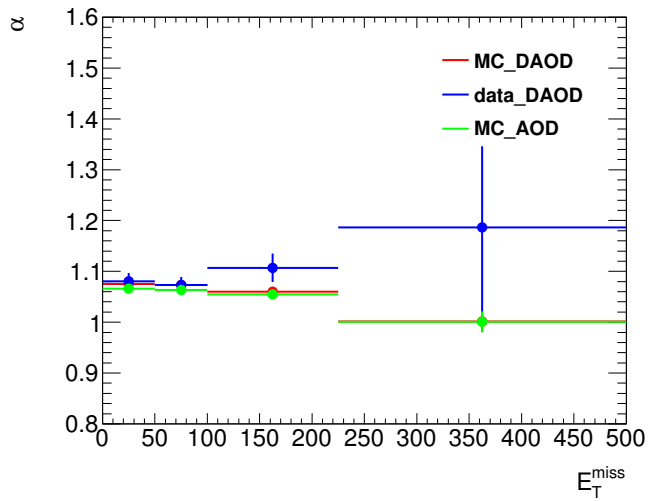


Figure 45: Measurements of  $k$ , the ratio of electron to muon events, in bins of  $p_T$  and  $\eta$ . On the top is the measurements indexed by the leading lepton, while the measurements indexed by the subleading lepton are on the bottom. These efficiencies are for the 2016 dataset.

The next uncertainty considers a potential bias in the way the  $\alpha$  factors are calculated. Because they are derived from data, there is already trigger dependence in data collection (only events passing a trigger are stored) and further dependences are introduced by the use of the “dAOD” data format. This is short for derived Analysis Object Data ([AOD](#)), and they provide smaller, more efficient versions of the complete ATLAS datasets. These dAODs are designed with spe-

cific analyses in mind, filtering on the triggers and objects required by the analyses. As a consequence, there are explicit requirements that lepton or  $E_T^{\text{miss}}$  triggers are passed before events are included in the dAODs used by this analysis. These requirements mean that the trigger efficiencies calculated from these samples do not include all possible events, and will have artificially high values. However, because the ratio of trigger efficiencies is the quantity needed for this analysis (see [Equation 30](#)), this will only bias the prediction if the different channels are differently impacted by the trigger preselection.

Calculating the **FS** prediction's dependence on these biases requires the use of **MC**. With a generated **MC** sample, there is no trigger dependence, so an unskimmed sample can be compared to a typical **MC** dAOD to identify the effect of the skimming. [Figure 46](#) shows a comparison of the  $\alpha$  factors calculated for different bins in  $E_T^{\text{miss}}$  from the nominal source, data, as well as these two **MC** sources. A  $E_T^{\text{miss}}$  dependence would be the most likely bias between the two **MC**-derived  $\alpha$  factors because  $E_T^{\text{miss}}$  triggers are the only triggers besides lepton triggers that will allow an event to be accepted into the dAOD used by this analysis. Though there is some difference between the data-derived  $\alpha$  and those taken from **MC**, it is clear from this plot that there is very little dependence on the choice of an unskimmed or skimmed sample. The actual calculation of the uncertainty is performed by repeating the flavor symmetric method in **MC** with each of the two  $\alpha$  factors and observing the difference between the estimates.



[Figure 46](#):  $\alpha$ , the trigger efficiency ratio, calculated as a function of  $E_T^{\text{miss}}$  from three different sources: data, the usual skimmed  $t\bar{t}$  **MC**, and an unskimmed  $t\bar{t}$  **MC**.

The last uncertainty relates to the main **MC** dependence of the method - the  $m_{\ell\ell}$  shape of the **FS** background. A correction factor is taken from **MC** in order to account for the  $m_{\ell\ell}$  widening, and the accuracy of that factor must be checked. Its shape is compared to that

of data in region similar to VR-FS, but with an  $H_T$  cut lowered to 300 GeV to increase statistics. The difference between the fraction of events on the Z mass peak in data and MC in this region is taken as a systematic uncertainty. To confirm that using this lowered  $H_T$  cut still gives a valid answer, the fractions are compared as a function of  $H_T$  in Figure 47. In these plots, especially in the higher-statistics 2016 plot, it is clear both that the data and MC agree very well and that there is no strong  $H_T$  dependence.

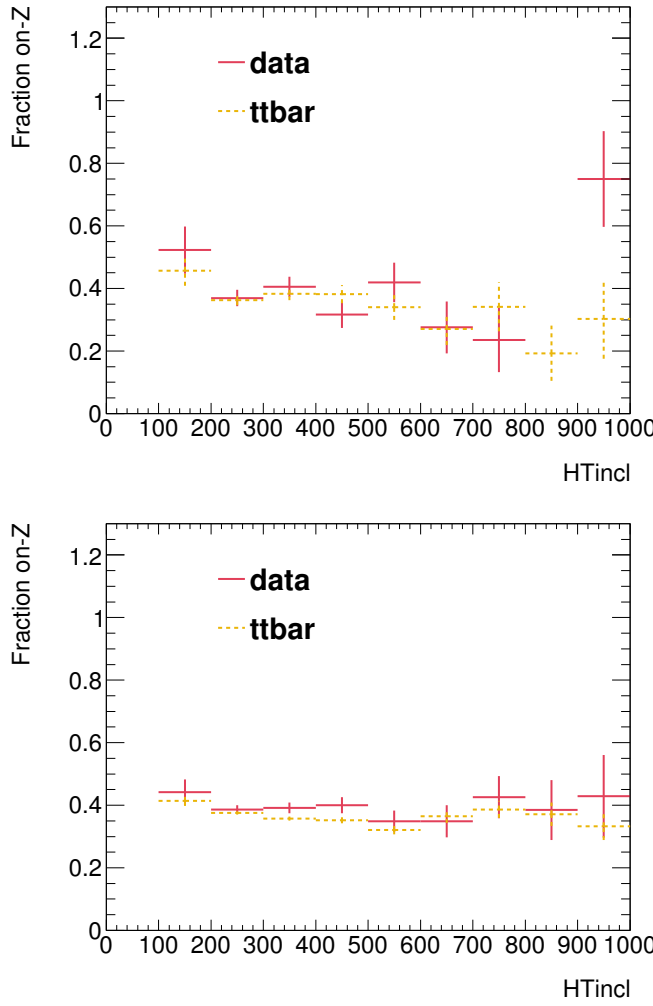


Figure 47: Plots of the fraction of on-Z events with a VR-FS-like selection as a function of  $H_T$ . The top figure shows 2015 data and MC while the bottom figure shows the same for 2016.

These uncertainties are each calculated independently for the two datasets then added. Statistical uncertainties, including the MC closure statistical uncertainties and the  $k$  and  $\alpha$  uncertainties, are added in quadrature between the two years. Uncertainties that are more likely to be correlated, such as the difference between the two estimates in MC closure and the dependence on using a dAOD to cal-

culate trigger efficiencies, are added linearly. The total uncertainty is about 12% of the nominal prediction in the signal region and about 9% in the validation region.

### 11.1.2 Uncertainties on the $\gamma+jets$ Method

### 11.1.3 Uncertainties on the Fakes Background

Systematic uncertainties on the fakes background are derived from a series of variations on the nominal method. Variations include scaling the real and fake efficiencies up and down by their statistical uncertainties, scaling the prompt lepton contamination in CR-fake up and down by 20%, and by requiring and vetoing  $b$ -tagged jets in CR-fake to determine the dependence on heavy flavor. Statistical uncertainties can also be large in regions with small numbers of events in the baseline selection, such as SRZ. In other regions, the  $b$ -tagging dependence provides the largest uncertainty. The full breakdown of uncertainties for the most important regions are listed in [Table 14](#).

Variation	SRZ	CRT	CRFS	VRFS	VRS	VRT
Nominal	$0.10 \pm 1.61$	$25.39 \pm 5.35$	$3.73 \pm 2.19$	$10.53 \pm 3.56$	$3.64 \pm 3.20$	$80.06 \pm 9.80$
EL F Up	0.15	30.23	3.96	10.93	3.56	92.46
EL F Down	0.06	21.80	3.52	10.18	3.54	70.07
EL R Up	0.25	26.17	3.92	11.10	4.13	82.57
EL R Down	-0.07	24.51	3.52	9.92	3.10	77.24
MU F Up	-0.20	32.48	4.77	16.41	5.25	86.48
MU F Down	0.29	20.17	2.91	7.04	2.87	70.12
MU R Up	0.13	25.67	3.78	10.66	3.81	81.18
MU R Down	0.05	25.04	3.67	10.38	3.44	78.72
Total Sys	+0.26 -0.35	+8.64 -6.39	+1.08 -0.87	+5.92 -3.56	+1.70 -0.97	+14.24 -14.42
Total Sys (%)	+261.05 -354.72	+34.01 -25.19	+29.05 -23.23	+56.22 -33.85	+46.57 -26.60	+17.78 -18.02
Real Cont. Up	0.23	20.97	3.06	8.08	3.15	68.79
Real Cont. Down	-0.01	29.67	4.38	12.95	4.16	90.23
$b$ -jet	0.31	40.44	5.28	8.98	5.63	120.50
no $b$ -jet	0.16	23.44	3.08	11.38	3.97	70.55
Total Sys	+0.25 -0.11	+15.65 -4.83	+1.69 -0.93	+2.56 -2.90	+2.09 -0.49	+41.71 -14.74
Total Sys (%)	+260.46 -109.06	+61.66 -19.02	+45.30 -24.85	+24.32 -27.58	+57.31 -13.35	+52.10 -18.42

**Table 14:** Systematic uncertainties on the fake-lepton background for on-Z regions for 2015+2016 yields. The nominal yield includes statistical uncertainty from the baseline selection in a given region. The following rows indicate the results of varying the real and fake lepton efficiencies up and down by their statistical uncertainty. Real cont. gives an uncertainty on the contamination of real leptons in the fake lepton efficiency.  $b$ -jet and no  $b$ -jet indicate the impact of requiring or vetoing  $b$ -tagged jets in the regions used to measure the fake efficiency.

## 11.2 THEORETICAL AND EXPERIMENTAL UNCERTAINTIES

Experimental uncertainties cover any detector effect or LHC condition that may not be modeled precisely correctly in MC. For each

uncertainty, a standard prescription from the ATLAS experiment is followed. Uncertainties are included on the following parameters:

- Luminosity (2.9%) [2, 6]
- Jet energy scale [9]
- Jet energy resolution [9]
- Jet vertex tagging
- Heavy flavor tagging
- $E_T^{\text{miss}}$  soft term [8]
- $e/\mu$  momentum scale
- $e/\mu$  trigger, reconstruction, and identification efficiencies
- Pileup

These uncertainties are applied to all [MC](#) samples used in the analysis. This includes signal models, diboson and rare top samples for the nominal estimate, and all backgrounds taken from [MC](#) in the sideband fit.

Theoretical uncertainties include cross-section uncertainties, scale uncertainties, and [PDF](#) uncertainties. For the diboson samples, the scale uncertainties, given in [Table 15](#) and calculated by varying each scale up and down by a factor of two, are combined with a 6% cross-section uncertainty and a generator uncertainty obtained by comparing PowHEG and SHERPA [MC](#) yields. The generator uncertainty, shown in [Table 16](#), is dominant in most regions. Rare top processes are given a 13% PDF and scale variation uncertainty [20] and a 22% cross section uncertainty [28, 39, 47].

Signal models have both the central value and uncertainty on cross-sections taken from an envelope of predictions using different scales and [PDF](#) sets [43]. The signal processes are calculated at Next-to-Leading-Logarithmic Accuracy ([NLO+NLL](#)), meaning they are calculated at next-to-leading order in the strong coupling constant, with additional terms from next-to-leading-logarithmic resummation of soft gluon emission [21–23, 44, 45].

### 11.3 IMPACT OF UNCERTAINTIES ON THE SIGNAL REGION

The breakdown of each major uncertainty’s contribution to the total uncertainty in SRZ is shown in [Table 17](#). The dominant uncertainty is the diboson generator uncertainty, followed by the statistical uncertainty from the [FS](#) background. Uncertainties smaller than 1% are not shown in the table.

$VV \rightarrow llvv$ Samples							
	SRZ	VRS	CRT	VRT	VRWZ	VRZZ	VR <sub>3L</sub>
resummation	0.07	0.03	0.01	0.02	0.00	0.00	0.00
renormalization	0.13	0.17	0.16	0.22	0.00	0.00	0.00
factorization	0.01	0.01	0.01	0.03	0.00	0.00	0.00
total	0.15	0.17	0.16	0.22	0.00	0.00	0.00
$WZ \rightarrow llvv$ Samples							
	SRZ	VRS	CRT	VRT	VRWZ	VRZZ	VR <sub>3L</sub>
resummation	0.07	0.05	0.13	0.08	0.02	0.00	0.01
renormalization	0.26	0.20	0.28	0.21	0.07	0.00	0.18
factorization	0.04	0.04	0.02	0.06	0.01	0.00	0.02
total	0.28	0.21	0.31	0.23	0.07	0.00	0.18
$ZZ \rightarrow llll$ Samples							
	SRZ	VRS	CRT	VRT	VRWZ	VRZZ	VR <sub>3L</sub>
resummation	0.27	1.07	0.01	0.01	0.06	0.01	0.53
renormalization	0.28	0.26	0.30	0.60	0.07	0.04	0.14
factorization	0.27	0.25	0.30	0.58	0.13	0.02	0.16
total	0.48	1.13	0.43	0.84	0.16	0.05	0.57

Table 15: Fractional uncertainties of dibosons in signal and validation regions from Sherpa scale variations.

Region	Sherpa Events/fb <sup>-1</sup>	Sherpa Events	Powheg Events/fb <sup>-1</sup>	Powheg Events	% Difference
WZ Samples					
SRZ+VRZ	5.219	76.722	3.286	48.300	37.046
CRT+VRT	1.060	15.583	0.742	10.913	29.970
WW/ZZ Samples					
SRZ+VRZ	1.921	28.244	0.685	10.070	71.424
CRT+VRT	6.281	92.332	3.142	46.188	55.474

Table 16: Comparison of yields in on-Z and off-Z regions in Sherpa and Powheg diboson MC at 14.7 fb<sup>-1</sup>.

Source	Relative systematic uncertainty [%]
	SRZ
Total systematic uncertainty	17
WZ/ZZ generator uncertainty	13
Flavour symmetry (statistical)	7
WZ/ZZ scale uncertainty	6
$Z/\gamma^* + \text{jets}$ (systematic)	4
Flavour symmetry (systematic)	3
$Z/\gamma^* + \text{jets}$ (statistical)	2
Fake-leptons	1

Table 17: Overview of the dominant sources of systematic uncertainty on the total background estimate in the signal regions. The values shown are relative to the total background estimate, shown in %.



# 12

## RESULTS

---



# 13

## INTERPRETATIONS

---



## Part V

### CONCLUSIONS

This section presents conclusions and an outlook for future work.



CONCLUSIONS

---



# 15

## OUTLOOK

---



## BIBLIOGRAPHY

---

- [1] .
- [2] ATLAS Collaboration. “Luminosity determination in pp collisions at  $\sqrt{s} = 8$  TeV using the ATLAS detector at the LHC.” In: *to be submitted to Eur. Phys. J. C* ().
- [3] ATLAS Collaboration. “The ATLAS Experiment at the CERN Large Hadron Collider.” In: *JINST* 3 (2008), S08003. doi: [10.1088/1748-0221/3/08/S08003](https://doi.org/10.1088/1748-0221/3/08/S08003).
- [4] ATLAS Collaboration. *Search for physics beyond the Standard Model in events with a Z boson and large missing transverse momentum using  $\sqrt{s} = 7$  TeV pp collisions from the LHC with the ATLAS detector.* ATLAS-CONF-2012-046. 2012. URL: <http://cdsweb.cern.ch/record/1448222>.
- [5] ATLAS Collaboration. *Search for supersymmetry in final states with jets, missing transverse momentum and a Z boson at  $\sqrt{s} = 8$  TeV with the ATLAS detector.* ATLAS-CONF-2012-152. 2012. URL: <http://cds.cern.ch/record/1493491>.
- [6] ATLAS Collaboration. “Improved luminosity determination in pp collisions at  $\sqrt{s} = 7$  TeV using the ATLAS detector at the LHC.” In: *Eur. Phys. J. C* 73 (2013), p. 2518. doi: [10.1140/epjc/s10052-013-2518-3](https://doi.org/10.1140/epjc/s10052-013-2518-3). arXiv: [1302.4393 \[hep-ex\]](https://arxiv.org/abs/1302.4393).
- [7] ATLAS Collaboration. “A neural network clustering algorithm for the ATLAS silicon pixel detector.” In: *JINST* 9 (2014), P09009. doi: [10.1088/1748-0221/9/09/P09009](https://doi.org/10.1088/1748-0221/9/09/P09009). arXiv: [1406.7690 \[hep-ex\]](https://arxiv.org/abs/1406.7690).
- [8] ATLAS Collaboration. *Expected performance of missing transverse momentum reconstruction for the ATLAS detector at  $\sqrt{s} = 13$  TeV.* ATL-PHYS-PUB-2015-023. 2015. URL: <http://cds.cern.ch/record/2037700>.
- [9] ATLAS Collaboration. *Jet Calibration and Systematic Uncertainties for Jets Reconstructed in the ATLAS Detector at  $\sqrt{s} = 13$  TeV.* ATL-PHYS-PUB-2015-015. 2015. URL: <http://cds.cern.ch/record/2037613>.
- [10] ATLAS Collaboration. *Measurement of performance of the pixel neural network clustering algorithm of the ATLAS experiment at  $\sqrt{s} = 13$  TeV.* ATL-PHYS-PUB-2015-044. 2015. URL: <http://cdsweb.cern.ch/record/2054921>.
- [11] ATLAS Collaboration. *Robustness of the Artificial Neural Network Clustering Algorithm of the ATLAS experiment.* ATL-PHYS-PUB-2015-052. 2015. URL: <http://cdsweb.cern.ch/record/2116350>.

- [12] ATLAS Collaboration. “Search for squarks and gluinos in events with isolated leptons, jets and missing transverse momentum at  $\sqrt{s} = 8$  TeV with the ATLAS detector.” In: *JHEP* 1504 (2015), p. 116. doi: [10.1007/JHEP04\(2015\)116](https://doi.org/10.1007/JHEP04(2015)116). arXiv: [1501.03555 \[hep-ex\]](https://arxiv.org/abs/1501.03555).
- [13] ATLAS Collaboration. “Search for supersymmetry in events containing a same-flavour opposite-sign dilepton pair, jets, and large missing transverse momentum in  $\sqrt{s} = 8$  TeV  $pp$  collisions with the ATLAS detector.” In: *Eur. Phys. J. C* 75 (2015), p. 318. doi: [10.1140/epjc/s10052-015-3518-2](https://doi.org/10.1140/epjc/s10052-015-3518-2). arXiv: [1503.03290 \[hep-ex\]](https://arxiv.org/abs/1503.03290).
- [14] ATLAS Collaboration. *2015 start-up trigger menu and initial performance assessment of the ATLAS trigger using Run-2 data*. ATL-DAQ-PUB-2016-001. 2016. URL: <http://cds.cern.ch/record/2136007>.
- [15] ATLAS Collaboration. “Measurement of the differential cross-section of highly boosted top quarks as a function of their transverse momentum in  $\sqrt{s} = 8$  TeV proton-proton collisions using the ATLAS detector.” In: *Phys. Rev. D* 93.3 (2016), p. 032009. doi: [10.1103/PhysRevD.93.032009](https://doi.org/10.1103/PhysRevD.93.032009). arXiv: [1510.03818 \[hep-ex\]](https://arxiv.org/abs/1510.03818).
- [16] ATLAS Collaboration. *Modelling of the  $t\bar{t}H$  and  $t\bar{t}V$  ( $V = W, Z$ ) processes for  $\sqrt{s} = 13$  TeV ATLAS analyses*. ATL-PHYS-PUB-2016-005. 2016. URL: <http://cds.cern.ch/record/2120826>.
- [17] ATLAS Collaboration. *Monte Carlo Generators for the Production of a  $W$  or  $Z/\gamma^*$  Boson in Association with Jets at ATLAS in Run 2*. ATL-PHYS-PUB-2016-003. 2016. URL: <http://cds.cern.ch/record/2120133>.
- [18] ATLAS Collaboration. *Multi-Boson Simulation for 13 TeV ATLAS Analyses*. ATL-PHYS-PUB-2016-002. 2016. URL: <http://cds.cern.ch/record/2119986>.
- [19] ATLAS Collaboration. *Simulation of top quark production for the ATLAS experiment at  $\sqrt{s} = 13$  TeV*. ATL-PHYS-PUB-2016-004. 2016. URL: <http://cds.cern.ch/record/2120417>.
- [20] J. Alwall, R. Frederix, S. Frixione, V. Hirschi, F. Maltoni, O. Matelaer, H. S. Shao, T. Stelzer, P. Torrielli, and M. Zaro. “The automated computation of tree-level and next-to-leading order differential cross sections, and their matching to parton shower simulations.” In: *JHEP* 07 (2014), p. 079. doi: [10.1007/JHEP07\(2014\)079](https://doi.org/10.1007/JHEP07(2014)079). arXiv: [1405.0301 \[hep-ph\]](https://arxiv.org/abs/1405.0301).
- [21] W. Beenakker, R. Höpker, M. Spira, and P.M. Zerwas. “Squark and gluino production at hadron colliders.” In: *Nucl. Phys. B* 492 (1997), pp. 51–103. doi: [10.1016/S0550-3213\(97\)00084-9](https://doi.org/10.1016/S0550-3213(97)00084-9). arXiv: [hep-ph/9610490 \[hep-ph\]](https://arxiv.org/abs/hep-ph/9610490).

- [22] W. Beenakker et al. "Soft-gluon resummation for squark and gluino hadroproduction." In: *JHEP* 0912 (2009), p. 041. doi: [10.1088/1126-6708/2009/12/041](https://doi.org/10.1088/1126-6708/2009/12/041). arXiv: [0909.4418 \[hep-ph\]](https://arxiv.org/abs/0909.4418).
- [23] W. Beenakker et al. "Squark and gluino hadroproduction." In: *Int. J. Mod. Phys. A* 26 (2011), pp. 2637–2664. doi: [10.1142/S0217751X11053560](https://doi.org/10.1142/S0217751X11053560). arXiv: [1105.1110 \[hep-ph\]](https://arxiv.org/abs/1105.1110).
- [24] C. P. Burgess and G. D. Moore. *The standard model: A primer*. Cambridge University Press, 2006. ISBN: 9780511254857, 9781107404267, 9780521860369.
- [25] CMS Collaboration. "Search for physics beyond the standard model in events with a  $Z$  boson, jets, and missing transverse energy in  $pp$  collisions at  $\sqrt{s} = 7$  TeV." In: *Phys. Lett. B* 716 (2012), pp. 260–284. doi: [10.1016/j.physletb.2012.08.026](https://doi.org/10.1016/j.physletb.2012.08.026). arXiv: [1204.3774 \[hep-ex\]](https://arxiv.org/abs/1204.3774).
- [26] CMS Collaboration. "Measurement of the integrated and differential  $t\bar{t}$  production cross sections for high-pt top quarks in  $pp$  collisions at  $\sqrt{s} = 8$  TeV." In: *Phys. Rev. D* (2016). Submitted. arXiv: [1605.00116 \[hep-ex\]](https://arxiv.org/abs/1605.00116).
- [27] J. M. Campbell and R. K. Ellis. "An update on vector boson pair production at hadron colliders." In: *Phys. Rev. D* 60 (1999), p. 113006. arXiv: [hep-ph/9905386 \[hep-ph\]](https://arxiv.org/abs/hep-ph/9905386).
- [28] J. M. Campbell and R. K. Ellis. " $t\bar{t}$  W production and decay at NLO." In: *JHEP* 1207 (2012), p. 052. arXiv: [1204.5678 \[hep-ph\]](https://arxiv.org/abs/1204.5678).
- [29] J. M. Campbell, R. K. Ellis, and C. Williams. "Vector boson pair production at the LHC." In: *JHEP* 1107 (2011), p. 018. arXiv: [1105.0020 \[hep-ph\]](https://arxiv.org/abs/1105.0020).
- [30] S. Catani and M. Grazzini. "An NNLO subtraction formalism in hadron collisions and its application to Higgs boson production at the LHC." In: *Phys. Rev. Lett.* 98 (2007), p. 222002. arXiv: [hep-ph/0703012 \[hep-ph\]](https://arxiv.org/abs/hep-ph/0703012).
- [31] S. Catani, L. Cieri, G. Ferrera, D. de Florian, and M. Grazzini. "Vector boson production at hadron colliders: a fully exclusive QCD calculation at NNLO." In: *Phys. Rev. Lett.* 103 (2009), p. 082001. arXiv: [0903.2120 \[hep-ph\]](https://arxiv.org/abs/0903.2120).
- [32] The ALICE Collaboration. "The ALICE experiment at the CERN LHC." In: *Journal of Instrumentation* 3.08 (2008), So8002. url: <http://stacks.iop.org/1748-0221/3/i=08/a=S08002>.
- [33] The CMS Collaboration. "The CMS experiment at the CERN LHC." In: *Journal of Instrumentation* 3.08 (2008), So8004. url: <http://stacks.iop.org/1748-0221/3/i=08/a=S08004>.
- [34] The LHCb Collaboration. "The LHCb Detector at the LHC." In: *Journal of Instrumentation* 3.08 (2008), So8005. url: <http://stacks.iop.org/1748-0221/3/i=08/a=S08005>.

- [35] M. Czakon, P. Fiedler, and A. Mitov. “Total Top-Quark Pair-Production Cross Section at Hadron Colliders Through  $O(\alpha_s^4)$ .” In: *Phys. Rev. Lett.* 110 (2013), p. 252004. arXiv: [1303.6254 \[hep-ph\]](https://arxiv.org/abs/1303.6254).
- [36] M. Czakon and A. Mitov. “Top++: A Program for the Calculation of the Top-Pair Cross-Section at Hadron Colliders.” In: *Comput. Phys. Commun.* 185 (2014), p. 2930. DOI: [10.1016/j.cpc.2014.06.021](https://doi.org/10.1016/j.cpc.2014.06.021). arXiv: [1112.5675 \[hep-ph\]](https://arxiv.org/abs/1112.5675).
- [37] Lyndon Evans and Philip Bryant. “LHC Machine.” In: *Journal of Instrumentation* 3.08 (2008), S08001. URL: <http://stacks.iop.org/1748-0221/3/i=08/a=S08001>.
- [38] D. Galbraith.
- [39] M. V. Garzelli, A. Kardos, C. G. Papadopoulos, and Z. Trocsanyi. “ $t\bar{t}W^{+-}$  and  $t\bar{t}Z$  Hadroproduction at NLO accuracy in QCD with Parton Shower and Hadronization effects.” In: *JHEP* 11 (2012), p. 056. DOI: [10.1007/JHEP11\(2012\)056](https://doi.org/10.1007/JHEP11(2012)056). arXiv: [1208.2665 \[hep-ph\]](https://arxiv.org/abs/1208.2665).
- [40] David J Griffiths. *Introduction to elementary particles; 2nd rev. version*. Physics textbook. New York, NY: Wiley, 2008. URL: <https://cds.cern.ch/record/111880>.
- [41] Huang, Qing-Guo, Wang, Ke, and Wang, Sai. “Constraints on the neutrino mass and mass hierarchy from cosmological observations.” In: *Eur. Phys. J. C* 76.9 (2016), p. 489. DOI: [10.1140/epjc/s10052-016-4334-z](https://doi.org/10.1140/epjc/s10052-016-4334-z). URL: <http://dx.doi.org/10.1140/epjc/s10052-016-4334-z>.
- [42] N. Kidonakis. “Two-loop soft anomalous dimensions for single top quark associated production with a  $W^-$  or  $H^-$ .” In: *Phys. Rev. D* 82 (2010), p. 054018. DOI: [10.1103/PhysRevD.82.054018](https://doi.org/10.1103/PhysRevD.82.054018). arXiv: [1005.4451 \[hep-ph\]](https://arxiv.org/abs/1005.4451).
- [43] Michael Kramer et al. *Supersymmetry production cross sections in pp collisions at  $\sqrt{s} = 7$  TeV*. 2012. arXiv: [1206.2892 \[hep-ph\]](https://arxiv.org/abs/1206.2892).
- [44] A. Kulesza and L. Motyka. “Soft gluon resummation for the production of gluino-gluino and squark-antisquark pairs at the LHC.” In: *Phys. Rev. D* 80 (2009), p. 095004. DOI: [10.1103/PhysRevD.80.095004](https://doi.org/10.1103/PhysRevD.80.095004). arXiv: [0905.4749 \[hep-ph\]](https://arxiv.org/abs/0905.4749).
- [45] A. Kulesza and L. Motyka. “Threshold resummation for squark-antisquark and gluino-pair production at the LHC.” In: *Phys. Rev. Lett.* 102 (2009), p. 111802. DOI: [10.1103/PhysRevLett.102.111802](https://doi.org/10.1103/PhysRevLett.102.111802). arXiv: [0807.2405 \[hep-ph\]](https://arxiv.org/abs/0807.2405).
- [46] *LEP design report*. Copies shelved as reports in LEP, PS and SPS libraries. Geneva: CERN, 1984. URL: <https://cds.cern.ch/record/102083>.

- [47] A. Lazopoulos, T. McElmurry, K. Melnikov, and F. Petriello. “Next-to-leading order QCD corrections to  $t\bar{t}Z$  production at the LHC.” In: *Phys. Lett. B* 666 (2008), p. 62. arXiv: [0804.2220 \[hep-ph\]](#).
- [48] A. D. Martin, W. J. Stirling, R. S. Thorne, and G. Watt. “Parton distributions for the LHC.” In: (2009). doi: [10.1140/epjc/s10052-009-1072-5](#). eprint: [arXiv:0901.0002](#).
- [49] Stephen P. Martin. “A Supersymmetry primer.” In: (1997). [Adv. Ser. Direct. High Energy Phys.18,1(1998)]. doi: [10.1142/9789812839657\\_0001](#), [10.1142/9789814307505\\_0001](#). arXiv: [hep-ph/9709356 \[hep-ph\]](#).
- [50] Johan Messchendorp. “Physics with Charmonium – A few recent highlights of BESIII.” In: *PoS Bormio2013* (2013), p. 043. arXiv: [1306.6611 \[hep-ex\]](#).
- [51] F. Zwicky. “Die Rotverschiebung von extragalaktischen Nebeln.” In: *Helvetica Physica Acta* 6 (1933), 110–127.
- [52] LHCb collaboration. “Observation of  $J/\Psi p$  resonances consistent with pentaquark states in  $\Lambda_b^0 \rightarrow J/\Psi K^- p$  decays.” In: (2015). doi: [10.1103/PhysRevLett.115.072001](#). eprint: [arXiv:1507.03414](#).
- [53] T. S. van Albada, J. N. Bahcall, K. Begeman, and R. Sancisi. “Distribution of dark matter in the spiral galaxy NGC 3198.” In: *The Astrophysical Journal* 295 (Aug. 1985), pp. 305–313. doi: [10.1086/163375](#).